Excitation and Excitability of Unipolar Brush Cells

The work described in this thesis was carried out at the Netherlands Institute for Neuroscience in Amsterdam, an institute of the Royal Netherlands Academy of Arts and Sciences, under the supervision of prof.dr. C.I. de Zeeuw.

Typeset by LaTeX. Printed by Ridderprint.

Excitation and Excitability of Unipolar Brush Cells

Prikkeling en prikkelbaarheid van *unipolar brush* cellen

PROEFSCHRIFT

ter verkrijging van de graad van doctor aan de
Erasmus Universiteit Rotterdam
op gezag van de
rector magnificus

Prof.dr. H.A.P. POLS

en volgens besluit van het College voor Promoties.
De openbare verdediging zal plaatsvinden op
dinsdag 21 januari 2014 om 13:30 uur
door

Stijn van DORP
geboren te Oosterhout

ERASMUS UNIVERSITEIT ROTTERDAM

Promotiecommissie

Promotor:	Prof.dr. C.I. de Zeeuw
Overige leden:	Prof.dr. J.G.G. Borst
	Dr. T.J.H. Ruigrok
	Prof.dr. J. van der Steen

Mother Nature's quite a lady...

Contents

Chapter 1

Introduction

THE cerebellum is a distinct brain structure that ensures the spatial accuracy and temporal coordination of movements. It is located superimposed on the brainstem and has an appearance and organization unlike that of the cerebral cortex: its surface has a highly regular foliation pattern, and its neural circuitry is organized in repeated structured modules. Neural activity enters the cerebellum via two excitatory pathways, the mossy fiber system and the climbing fiber system. Climbing fibers originate from the inferior olivary nucleus in the brainstem, and assert a powerful influence on cerebellar output and long-term adaptation processes. Mossy fibers originate from a large number of sources, and carry contextual information on sensory inputs, aspects of motor planning and commands, and proprioceptive feedback. In the cerebellum this information is evaluated and integrated, to produce neural output that influences ongoing movement directly. Mossy fiber signals are processed in the cerebellum in three stages. In the granular layer, the input stage of the cerebellum, mossy fiber signals undergo a recoding step where they are combined and expanded by granule cells. Next, in the molecular layer, granule cell signals are integrated with climbing fiber signals in Purkinje cells. Together, the granular layer and molecular layer make up the cerebellar cortex. Finally, Purkinje cell activity is integrated in the cerebellar nuclei, which form the output stage, and project to various motor and pre-motor systems in the cerebral cortex and brainstem. The cerebellar cortex acts to modulate ongoing movement commands in order to make movements more accurate. Damage to the cerebellum can cause impairments in the control of movements, and bodily balance and posture.

1.1 The vestibulo-cerebellum

The experiments presented in this thesis were performed in the vestibulo-cerebellum, which is involved in the control of bodily balance and eye movements [1]. It is the most primitive part of the cerebellum, already present in fish, and (among other tasks) optimizes the vestibulo-ocular reflex (VOR), a particularly well-studied reflex movement [2–4]. The VOR aids to stabilize images on the retina by countermoving the eyes in response to head movement. It is initiated by activation of the vestibular organs [5], which signal information about angular and linear velocity of the head, as well as static tilt of the head relative to gravity [6]. The VOR is complemented by opto-kinetic reflexes (OKR), which move the eyes in response to motion of the visual field on the retina. Signals from vestibular, retinal and other sources are integrated in the vestibular nuclei in the brainstem, which produce the oculo-motor commands that instigate eye movement.

The area of the cerebellum involved in the VOR is called the flocculo-nodular lobe, consisting of the lateral (para-) flocculi and medial nodulus and uvula/lingula [1]. It ensures accuracy of reflexive eye movements, by modulating amplitude and timing of VOR and OKR [2]. The flocculo-nodular lobe can be further divided into functional zones [7], that each control a component of the eye movement related to a specific head rotation or translation direction [8, 9]. Mossy fiber inputs to the flocculo-nodular lobe arise from the vestibular nuclei and related nuclei in the brainstem, and in some areas directly from the vestibular ganglia [10]. They encode a mixture of head and eye movement kinematics. Climbing fiber inputs originate from a region of the inferior olivary nucleus called the dorsal cap of Kooy [11]. They are believed to signal a measure of the performance of the oculo-motor system, based on evaluation of discrepancies between neural oculo-motor commands and feedback on the accuracy of the actual eye movement. This information is used by the cerebellum to refine its output in order to optimize performance. Although output from the cerebellar cortex is typically mediated by the cerebellar nuclei, areas of the vestibulo-cerebellar cortex interfere directly with activity in the vestibular nuclei.

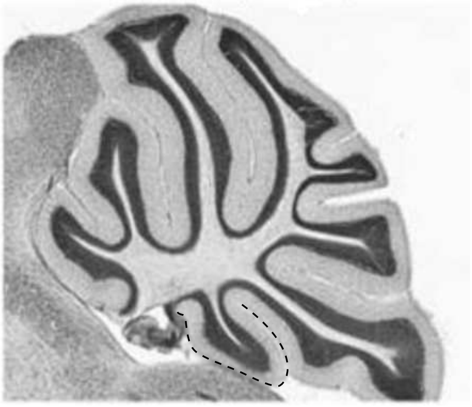

Figure 1.1: Sagittal slice of mouse cerebellar vermis. The granular layer is stained dark, the outer light grey layer is the molecular layer. Inner white matter consists of mossy fibers, climbing fibers and Purkinje cell axons. The cerebellar nuclei are in the center. The dashed contour marks the nodulus.

1.2 The cerebellar granular layer

Although the human cerebellum occupies only 10-15 % of the total volume of the brain, it contains over half of all its neurons. Most of these neurons are granule cells, which constitute the main elements of the input stage of the cerebellar cortex, the granular layer. Granule cells are small excitatory neurons (typical soma diameter ∼5 µm), with on average four arm-like dendrites, and an axon that protrudes into the molecular layer. Mossy fibers entering the granular layer split into multiple branches, which terminate as rosettes that form the pre-synaptic elements of granule cells. Each rosette is at the center of a glomerular structure enwrapped by glial processes, in which it contacts dendrites from tens of granule cells. Granule cells thus recode information by combining mossy fiber inputs, resulting in a huge expansion as each mossy fiber can contact hundreds of granule cells [12]. Mossy fiber-granule cell transmission is modulated by inhibition from Golgi cells, a local granular layer interneuron [13]. Golgi cells are large (typical soma diameter ∼ 20 µm), relatively sparsely distributed neurons that are thought to multiplex several tasks, from setting granule cell excitability through slow tonic inhibition, to fine-tuning granule cell activation windows on the millisecond time scale [14]. Early influential theoretical studies have suggested that the granular layer forms non-linear combinations of mossy fiber signals from distinctly different sensory modalities, to facilitate the associative capabilities of the cerebellar cortex [15, 16]. Such multimodal input to granule cells has indeed been shown experimentally [17], but local differences in the principles of granule cell recoding might still exist across the cerebellum [18].

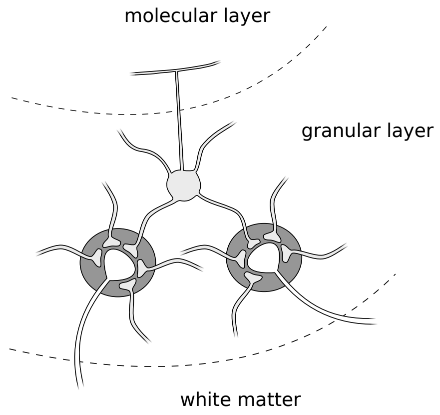

Figure 1.2: Schematic drawing of mossy fiber-granule cell connections. Granule cells (light grey) typically have four dendrites, which form synapses with mossy fibers (white) in glomerular structures (dark grey). Granule cells combine and expand mossy fiber signals, and their axons project into the molecular layer where they give rise to the parallel fibers that synapse onto Purkinje cells and local interneurons.

In the vestibulo-cerebellum, mossy fibers display relatively high background firing rates *in vivo* (∼10 Hz in mice, ∼80 Hz in primates), and encode aspects of the kinematics of eye and head movements [6, 19, 20]. In contrast, granule cells appear mostly inactive at rest, but can generate action potentials at high instantaneous frequencies (several hundred Hz) in response to synaptic input [21]. The vestibulo-cerebellum is further characterized by the abundance of a relatively unexplored class of excitatory granule cell layer interneurons, called unipolar brush cells (UBCs) [22]. UBCs are interposed between mossy fibers and granule cells, and have a characteristic morphology consisting of an intermediate sized soma ($\sim$ 10 μm diameter) and a single, short bushy dendrite [23]. The few available reports of their activity *in vivo* reveal a very regular background activity and modulation by vestibular stimuli, but their functions are not well understood [21]. UBCs are the main topic of this thesis.

1.3 Experimental techniques

Neuronal signaling occurs through perturbations in the electrical potential that is maintained across the outer membrane of cells. The experiments presented in this thesis were performed using the whole-cell patch-clamp technique, which allows for manipulating the membrane potential of cells, and measuring directly the flow of ionic current [24]. To this end, the tip of a small glass pipette filled with electrolyte is sealed to the outer membrane of a cell, and a small hole is created in the membrane through a brief suction pulse. An electrode placed inside the pipette then allows for determining the potential inside the cell, with respect to a reference electrode outside the cell. Two modes of electrical measurement are typically used, termed 'voltage-clamp mode' and 'current-clamp mode'. In voltage-clamp mode, the electronic amplifier circuitry is set to maintain a constant value of the membrane potential, through a feedback mechanism that rapidly adjusts the current flow through the pipette. This allows for isolated measurement of current flows, such as for example the currents generated by chemical receptor ion channels in the postsynaptic membrane. In current-clamp mode, the membrane potential is allowed to develop freely, and the amplifier is set to use a voltage-follower circuitry performing a minimal-interference measurement of the potential. Current can be injected through the pipette directly into the cell, and neuronal signalling events such as action potentials can be observed.

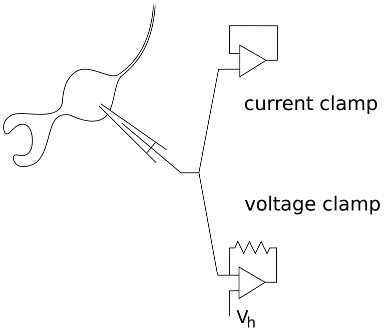

Figure 1.3: Whole-cell recording. Current-clamp mode is used to measure the development of the membrane potential, and directly inject current into the cell. Voltage-clamp mode is used to maintain a fixed membrane potential (V_h) and measure current flow across the membrane.

The electrical interface of a pipette with a neuron introduces unwanted signal filtering, which can be largely compensated for online. Standard methods were used for online compensation of pipette capacitance and access resistance artifacts

[25], as well as for determination of passive electrical properties such as access resistance, whole-cell membrane resistance and whole-cell membrane capacitance [26]. In line with standard conventions, the resting membrane potential of a neuron is reported here as a negative potential, and inward (depolarizing) currents are reported as negative currents.

Experiments were performed in thin (250 μm) sagittal slices of the cerebellum of 4-7 weeks old mice. Neurons were visualized using infrared differential interference contrast (IR-DIC) microscopy, which allows visualization of transparent objects, and works particularly well for biological samples. In DIC microscopy, two parallel images of an object are created with a slight spatial offset, which induces differences in phase shifts of incident light at object edges. Recombining the two phase-shifted images creates an interference pattern that is the DIC image. Furthermore, by loading the patch pipette with a fluorescent dye, neurons could be visualized using reflected fluorescent microscopy coupled into the same light path, see Figure 1.4A for examples. Experimental procedures are covered in more detail in the relevant chapters.

1.4 Unipolar brush cells

UBCs were identified as a distinct cell class by Mugnaini and colleagues in the 1990s. They are present in the cerebellum of all mammals studied, as well as in cerebellum-like structures such as dorsal cochlear nucleus. Some birds like chicken and pigeon also have high densities of cerebellar UBCs in several lobules not related to the vestibulo-cerebellum. Their morphologically and functionally most distinctive feature is the single dendrite, which has a paint brush-like tuft with many small protrusions termed dendrioles at the tip (hence the adjective 'unipolar brush'), and forms a single large synaptic contact with a mossy fiber rosette. This section provides a brief overview of the characteristics of cerebellar UBCs, based in part on a recent review by Mugnaini and colleagues [23]. Data and images presented for illustration are original.

1.4.1 Neurogenesis and lobular distribution

The distribution of UBCs across the cerebellum is species-specific, but they are generally present in the oculo-motor vermis and are clearly most abundant in the flocculo-nodular lobes. Although they are vastly outnumbered by granule cells, their presence is significant especially in the nodulus, which contains on average ∼7 UBCs for each Golgi cell and ∼2 for each Purkinje cell in rats [27]. Like granule cells and cerebellar nuclei neurons, UBCs originate from precursors situated in the rhombic lip. UBCs are produced in the rhombic lip during the late embryonic period, and stay there for one or more days before migrating through the developing white matter into the internal granular layer of the cortical lobules. UBCs and granule cells have distinct lineages, and migrating UBCs never reach the external granular layer [28]. Mature UBC features are not developed until the entire external granular layer has reached the internal granular layer.

During migration UBCs acquire two main phenotypes, characterized by the expression of either metabotropic glutamate receptor 1a (mGluR1a) or calretinin (CR). This division is corroborated by differential distribution of several other genetic markers [29]. Immunostaining studies have shown that UBC subclasses display partly overlapping, but distinctly different lobular distributions. mGluR1a$^+$ UBCs represent approximately 70% of all UBCs and are present in all lobules, although their density is highest in the ventral nodulus (lob X). CR$^+$ UBCs are largely restricted to nodulus and uvula (lob IX), and are particularly abundant in the transition zone between these lobules. In general, the highest UBC densities are found in the vermis, with a marked decrease in density in lateral directions. Both types of UBCs are present in high density in the flocculus and paraflocculus.

The lobular distributions of UBCs appear correlated with the distribution of origins of afferent mossy fibers, although this is a largely unexplored topic. In the uvula and nodulus, CR$^+$ UBCs are targeted by primary vestibular mossy fibers from vestibular end organs. Also, choline acetyl transferase (ChAT)-immunoreactive mossy fibers originating from the vestibular nuclei were shown to innervate UBCs in these areas in rats, but their phenotypes were not identified [30]. Corticotropin releasing factor (CRF)-positive mossy fiber terminals were found in close apposition to CR$^+$ UBCs in the nodulus and flocculus, but the source of these fibers was not determined.

1.4.2 Synaptic transmission

The UBC dendritic brush is an extensive, irregular structure with many small protruding filaments (dendrioles), which enwraps a major portion of a presynaptic mossy fiber terminal. Total synaptic junctional area may be in the order of 20-40 μm^2 in rats [31]. Like mossy fiber-granule cell synapses, mossy fiber-UBC synapses are located in a glomerular structure with Golgi cell dendritic terminals and glial processes, and usually also granule cell dendritic terminals.

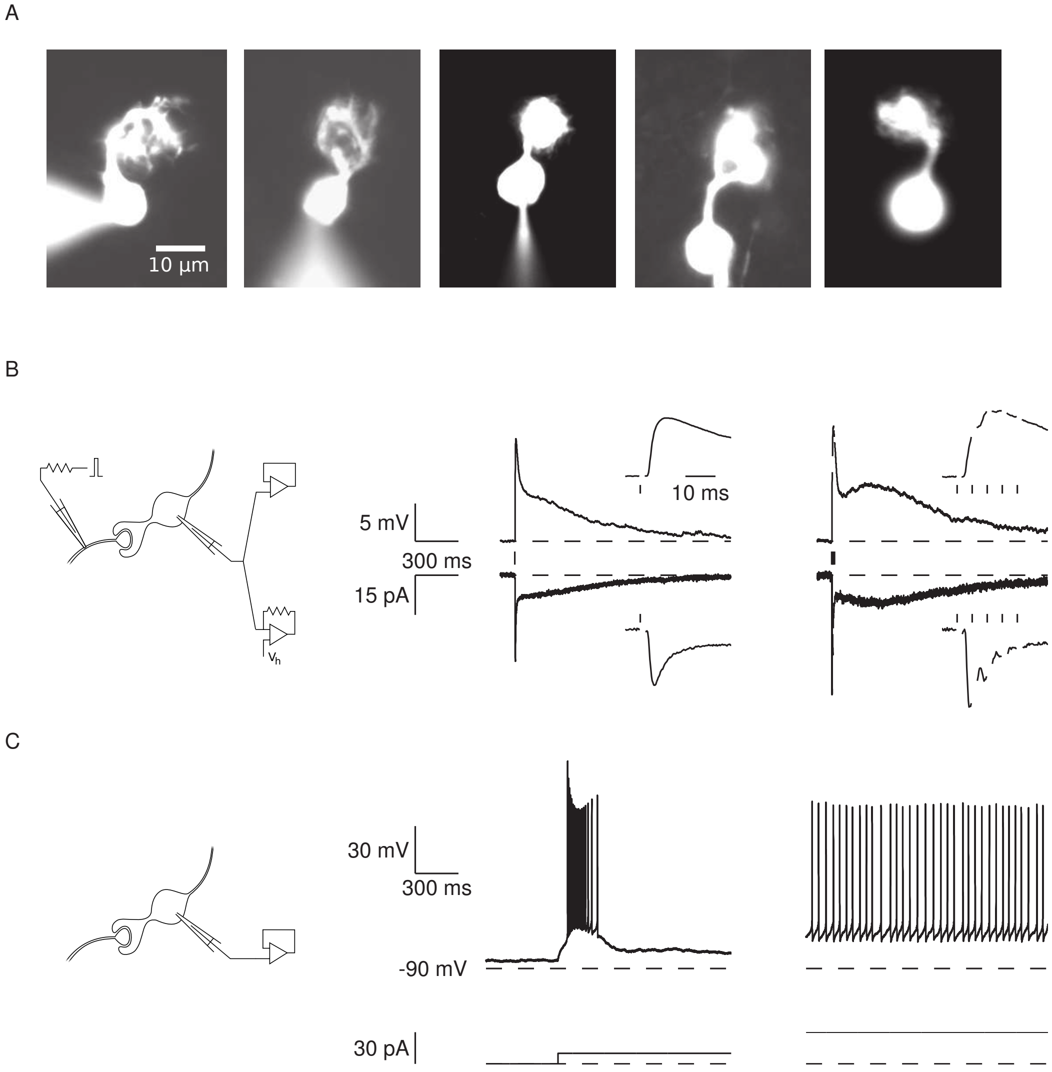

Figure 1.4: Characteristic UBC features. (A) Fluorescence images of five different mouse UBCs filled with dye through a pipette on the soma. There was considerable variation between UBCs with respect to the length of the dendritic shaft and the size of the brush. (B) Typical UBC responses to presynaptic stimulation. Top traces were obtained in current-clamp configuration, bottom traces in voltage-clamp with the same cell. Traces are averages of at least five trials. Times of stimulation are indicated by vertical black bars. (C) Bimodal UBC responses to direct somatic current injection through the pipette. A step-wise current increase from a hyperpolarized state elicited a strong burst of action potentials. Sustained current injection from a more depolarized state resulted in regular generation of action potentials.

1.4.2.1 Excitatory input

The brush is characterized by multiple asymmetric synaptic junctions with prominent postsynaptic densities (PSDs). AMPA receptors (AMPARs) in the brush contain GluR2 and most likely GluR6 subunits, and NMDA receptors (NMDARs) likely contain, apart from NR1, the NR2A and NR2B subunits. G-protein-coupled mGluRs are present at the perisynaptic membrane surrounding the PSD and extrasynaptically at filopodia [32]. UBCs differentially express mGluR2 although not restricted to one of the two above-mentioned UBC subtypes. mGluR1a is restricted to the CR^- subset of UBCs (see 1.4.1), while mGluR1b and 1c are not expressed in UBCs. mGluR2 activation hyperpolarizes UBCs through activation of a background potassium current [33], while mGluR1a activation depolarizes UBCs [34]. It is not clear to which extent synaptically released glutamate has the ability to activate mGluRs in UBCs.

The glomerular structure and extensive synaptic apposition of UBC synapses have some unusual consequences for synaptic transmission. At most central synapses, the lifetime of neurotransmitter in the cleft is short, limited by rapid diffusional escape to the surrounding medium [35]. In contrast, the UBC synapse has been hypothesized to promote prolonged entrapment of glutamate in the synaptic cleft [36, 37]. Excitatory postsynaptic currents (EPSCs) recorded from rat UBCs have a 'classical' fast component, mediated by AMPARs, followed by a protracted tail of persistent inward current that can last up to seconds. The slow tail is believed to be due to the prolonged presence of glutamate in the cleft, and is mediated by NMDARs or AMPARs, or a combination of both [36]. In many UBCs, the biphasic appearance of EPSCs is particularly striking as the slow current first rises to peak in several hundreds of milliseconds, before decaying to baseline in seconds. Such slow resurgent EPSCs are mediated by AMPARs, and are believed to arise from interplay between receptor desensitization and dose-response properties, due to long-lasting activation by ambient glutamate [37].

Figure 1.4B shows examples of UBC responses to electrical stimulation of the presynaptic mossy fiber in a mouse cerebellar slice. To date, reports in the literature on UBC synaptic responses have been limited to rats, but it is clear from the figure that the most salient features of the response are also present in mice. A single presynaptic stimulus resulted in a fast initial peak response, followed by a slow tail that decayed to baseline with a time constant of ~ 450 ms. High-frequency burst stimulation triggered the development of a 'bump' in the slow tail, which rose to peak in ~ 200 ms. In general, the slow bump was of lower amplitude and had rise and decay times that were approximately a factor 1.5 faster as compared to rats. A detailed account of UBC EPSC parameters is provided in Chapter 2.

1.4.2.2 Inhibitory input

Axons from Golgi cells make synaptic contacts with UBC brush dendrioles in the periphery of glomeruli and on the dendritic shaft. Whereas glycinergic receptors

(GlyRs) are present in all UBCs at these sites in rats (17-21 days), expression of GABA-ergic receptors (GABARs) is strictly anti-correlated with postsynaptic mGluR2 (but not mGluR1a) expression [38]. Individual Golgi cells contact both granule cells and UBCs, and have been shown to co-release GABA and glycine. Due to the differential expression of postsynaptic inhibitory receptors, Golgi cell activity thus has a target-dependent effect on UBCs [39]. Glycinergic IPSCs in UBCs are slower and of lower amplitude than GABA-ergic IPSCs, and might serve to set an inhibitory tone on mossy fiber-UBC synaptic transmission. The larger and faster GABA-ergic IPSCs might in turn play a direct part in spike timing of mGluR2$^-$ UBCs.

1.4.2.3 Input forwarded by presynaptic UBCs

The potential impact of UBCs on cortical neural activity can be especially appreciated from their axonal projections. Axons from UBCs project within the granule cell layer, where they branch extensively and form multiple rosette-like terminals. UBC axons are often referred to as granular layer 'internal' mossy fibers, as their rosettes strongly resemble extra-cerebellar ('external') mossy fiber rosettes. As is the case with external mossy fibers, the rosettes of UBC axons form the cores of glomeruli where they contact tens of granule cells, and also sometimes other UBCs. UBCs thus form an intricate network of excitatory feedforward projections within the granular layer, and it has been estimated that in the nodulus at least 50% of mossy fiber rosettes arise from UBCs [40].

Figure 1.5A shows a fluorescence image of a UBC in the sagittal plane, including part of its axonal outgrowth. The axon formed at least four rosettes, two of which are visible in the image (the others were in different focal planes). This single UBC would thus have been able to forward signals to many granule cells and/or several other UBCs. Some experimental evidence exists for electrophysiological functionality of the UBC-granule cell synapse. In a recent study, UBCs were stimulated using local drug application to activate mGluR1s, while EPSCs were recorded from a postsynaptic granule cell [34]. The authors used this tool to study properties of NMDA receptors at the UBC-granule cell synapse. Stimulation of mossy fibers in the nodulus can evoke delayed trains of EPSCs in granule cells, that are not observed in other lobules [41]. An example of such an experiment is shown in Figure 1.5B, with a cartoon of the putative connectivity. EPSCs were consistently observed with a delay of > 10 ms, indicating at least a disynaptic connection. Presumably, the stimulus elicited a burst response in a presynaptic UBC, which subsequently triggered EPSCs in the postsynaptic granule cell. A similar

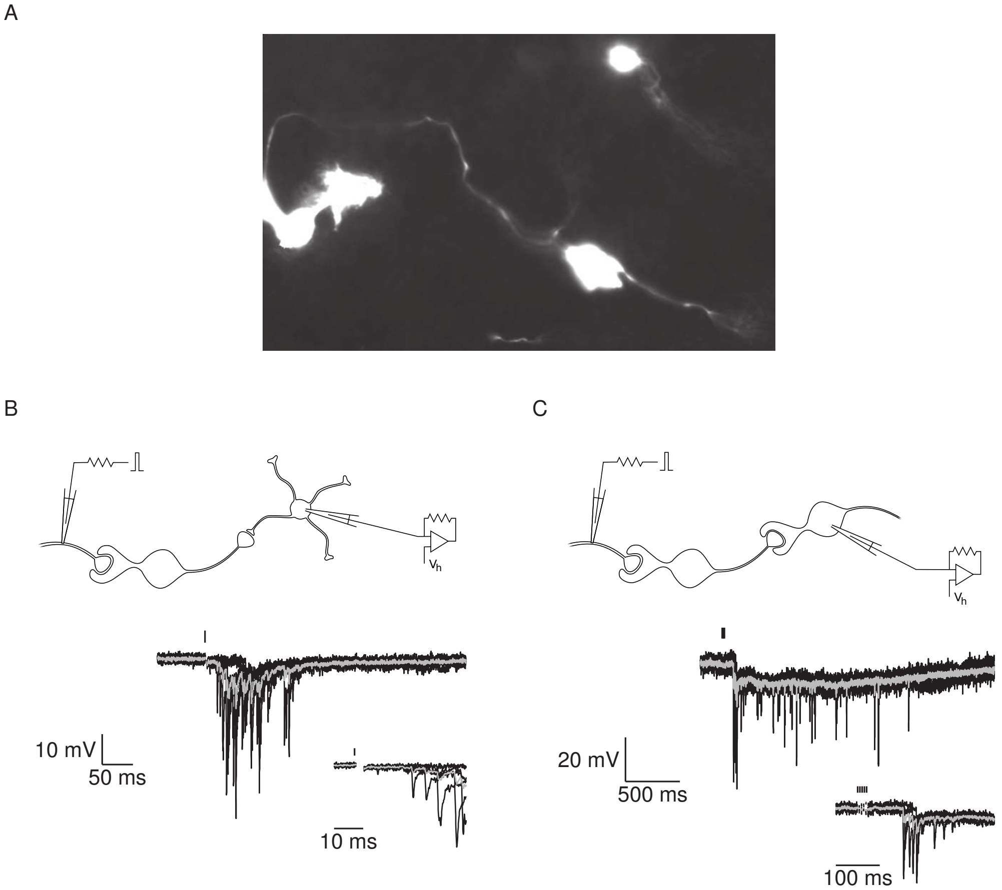

Figure 1.5: Disynaptic stimulus responses in the nodulus. (A) Fluorescence image of a UBC filled with dye through the pipette. The axon of this UBC could be traced through a large portion of the lobule, branching several times and sprouting at least four rosettes, two of which are visible here. (B) Delayed EPSCs in a granule cell in response to mossy fiber stimulation, due to a putative UBC-granule cell connection. Five traces, average in grey. (C) Delayed EPSCs in a UBC, due to a putative UBC-UBC connection.

scenario is depicted in Figure 1.5C for a recording from a UBC. This response was distinctly different as compared to the granule cell response (note the different time scales), and presumably resulted from delayed burst generation followed by a prolonged train of action potentials in the presynaptic UBC. The resulting EPSCs were then integrated in the postsynaptic UBC, resulting in an inward current plateau that lasted seconds. Such prolonged activations, in combination with the strategic position in the granular layer network, are likely to allow UBCs to significantly influence cortical information processing [23, 42].

1.4.3 Intrinsic excitability

1.4.3.1 Activity of UBCs *in vivo*

Only few accounts exist of the properties of UBC activity *in vivo*. In anesthetized rats, most UBCs were found to fire spontaneous regular action potentials at 7-47 Hz in the uvula-nodulus, although some UBCs were also found that fired more irregularly at lower rates of 1-6 Hz [21, 43]. Similar activity patterns were found in the flocculus of the anesthetized rabbit, and in the awake rabbit putative UBCs were found with regular activity that was modulated by head movements. Interestingly, the authors of this study noted that UBCs responded to movement of the head (and eyes) with a considerable delay of ∼200 ms [43]. In the uvula-nodulus of anesthetized mice UBCs were spontaneously active at ∼10 Hz and were modulated by vestibular stimulation (roll tilt) [44]. Regular spontaneous background activity thus appears a general feature of UBCs *in vivo* across species. However, it should be noted that the mentioned studies used extracellular recording techniques, which are inherently biased in favor of spontaneously active neurons.

1.4.3.2 Activity of UBCs in slices

A characteristic feature of UBCs is the ability to trigger a burst of action potentials from a hyperpolarized state ($\lesssim -90$ mV), in response to depolarizing current steps [45]. Such all-or-none events are mediated by low-threshold T-type calcium channels preferentially located in the dendritic brush, and transiently depolarize UBCs to a level above the threshold for action potential generation (suprathreshold). UBCs also typically display strong H-currents [46], which are slowly-inactivating currents that are activated by hyperpolarization, and are known the promote burst firing [47]. It has been reported that H-currents are expressed to a lesser extent in mGluR1a$^+$ UBCs [48]. From a more depolarized state, UBCs in slices generate action potentials at a regular pace [45, 46]. Examples of these two modes of UBC activation are shown in Figure 1.4C. UBC excitability will be discussed further in Chapter 4.

The literature provides mixed reports on the spontaneous activity of UBCs in slices. UBCs were reported to be mostly silent in 17-21 days old rats at 33-36 °C [45] and in 17-33 old rats at room temperature [47], while they were found to be intrinsically active with very regular firing at ∼20 Hz in 26-38 days old mice at 22-24 °C [46]. In mice, the propensity for spontaneous activity was shown to be mostly present in mGluR1a^{-} UBCs [48], and modulated by type 2 metabotropic glutamate receptors [33]. As the two main UBC subtypes are differentially distributed within the uvula/nodulus, and also display some slight morphological differences, the apparent discrepancies in the various reports might be due to a selection bias. In the experiments performed for this thesis, UBCs were found that were silent, bursty or regularly firing in extracellular recordings in the uvula/nodulus of 4-7 weeks old mice. Examples of extracellular recordings from a bursty and a regularly firing UBC are shown in Figure 1.6A. Chemical blockers for excitatory synaptic transmission were not present in these cases, so the bursts might also have been caused by synaptic inputs.

As external mossy fibers are not spontaneously active in slices, any spontaneous EPSCs observed in granule cells or UBCs are likely due to spontaneous activity in presynaptic UBCs. Spontaneous EPSCs/EPSPs were encountered occasionally during experiments for this thesis. Two examples are shown in Figures 1.6B and 1.6C, for recordings from a granule cell and a UBC respectively. In these examples, EPSCs were triggered by occasional short presynaptic bursts, resulting in typical EPSC waveforms in granule cells and UBCs.

1.5 Scope of this thesis

UBCs are a relatively newly defined cell class in the cerebellar cortex, and many of their properties are largely unexplored. Nonetheless, details of their specific and restrictive distribution are increasingly becoming clear, and the most salient characteristics of their physiology have been elucidated and confirmed by several groups. Their physiological functions however remain elusive. In order to understand how UBCs contribute to cerebellar function it is crucial to understand the neural signal transformations that they perform, defined by the properties of synaptic transmission, intrinsic excitability and neurotransmitter release. This thesis contributes towards this goal by describing new insights into the process of temporal integration in UBC synaptic transmission, as well as the input-output transformations in UBC action potential generation. It provides the first experiments on synaptic transmission of UBCs in mice, which has thus far only been described in rats.

In Chapter 2 an analysis is presented of basic properties of UBC EPSCs in mice. The slow tail of UBC EPSCs determines temporal integration already at low stimulation frequencies, and this issue was investigated in this chapter using various long-lasting stimulation protocols. In particular, the question was addressed to

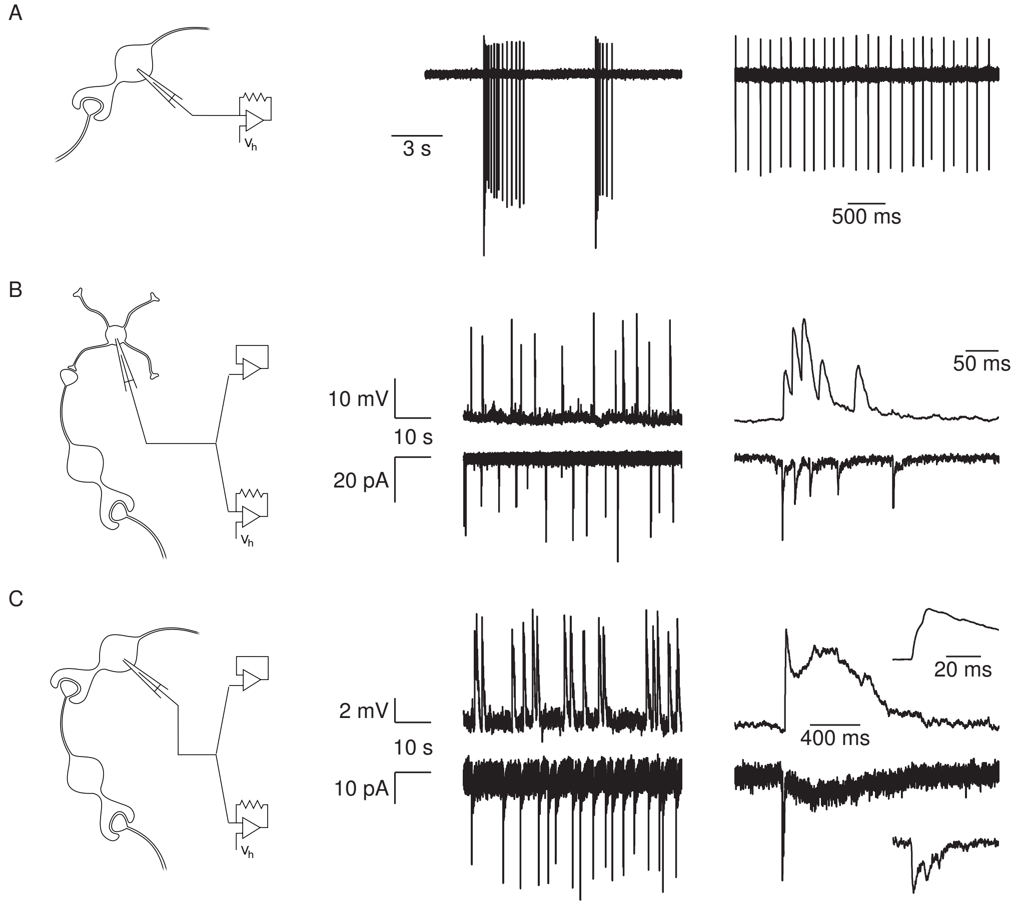

Figure 1.6: Spontaneous UBC activity. (A) Extracellular recordings from the soma of two different UBCs. Different types of spontaneous activities were observed in UBCs, some were fully silent while others displayed very regular firing patterns. Bursty firing patterns were also occasionally observed, although those could well have been due to synaptic inputs under the used conditions. (B) Spontaneous EPSCs recorded in a granule cell. These EPSC bursts putatively arose from a spontaneously bursting presynaptic UBC. Examples are shown in current-clamp (top) and voltage-clamp (bottom) configurations. (C) Spontaneous EPSCs recorded from a UBC, putatively due to a presynaptic UBC. The EPSCs had the characteristic slow 'bump' following a burst of fast EPSCs. Fast EPSCs/EPSPs are shown enlarged in the insets.

which extent the timing of the slow resurgent EPSC peak depends on the frequency of presynaptic stimulation.

In Chapter 3, a more detailed analysis of the mechanism underlying the slow UBC EPSC is presented, on the basis of a numerical model of synaptic transmission. The slow EPSC is believed to be caused by slow diffusion of glutamate in the synaptic cleft, but it is at present unclear whether this is a viable hypothesis considering the properties of diffusion and the kinetics of receptor activation. A computational model was therefore used to investigate the biophysical basis of UBC EPSCs.

Finally, in Chapter 4, properties of UBC subthreshold and suprathreshold excitability are explored. UBCs display bimodal activity patterns *in vitro*, switching between bursting and sustained regular action potential firing. The properties of transmission of time-varying input signals in UBCs are however largely unknown. Therefore the question was addressed whether suprathreshold signal transmission in UBCs is linear, by using various patterns of direct somatic current injection.

Chapter 2

Timing of synaptic transmission in unipolar brush cells

The cerebellum ensures the smooth execution of movements, a task that requires accurate neural signaling on multiple time scales. Computational models of cerebellar timing mechanisms have suggested that temporal information in cerebellum-dependent behavioral tasks is in part computed locally in the cerebellar cortex. These models rely on the local generation of delayed signals spanning hundreds of milliseconds, yet the underlying neural mechanism remains elusive. In this chapter it is shown that UBCs are well-suited to represent time intervals in a robust way in the cerebellar cortex. UBCs exhibited delayed increases in excitatory synaptic input in response to presynaptic stimulation in mouse cerebellar slices. Depending on the stimulation frequency, delays extended from zero up to hundreds of milliseconds. Such controllable protraction of delayed currents was the result of the unusual mode of synaptic integration in UBCs, which was well described by a model of steady-state AMPA-receptor activation. This functionality extends the capabilities of the cerebellum for adaptive control of behavior, by facilitating appropriate output in a broad temporal window.

2.1 Introduction

In the cerebellar granular layer, mossy fiber-granule cell synapses are characterized by precise, reliable, high-bandwidth transmission, with significant short-term depression only at high frequencies ($\sim$100 Hz) [20, 49–52]. Some of the structural elements supporting these functionalities are a large and rapidly replenishable pool of releasable vesicles, fast vesicle release, and a small PSD surface area of < 1 μm^2 [49, 50]. In recent years it has become clear that the glomerular structure of the mossy fiber-granule cell synapse promotes cross-talk between individual mossy fiber release sites, by activating neighbouring granule cell synapses through glutamate spillover [49, 53, 54]. Apart from direct activation, glutamate spillover can significantly influence fast synaptic transmission through AMPAR desensitization [55–57]. AMPARs have an affinity to desensitize to concentrations of glutamate in the micromolar range, and desensitization can become nearly complete at saturating concentrations [58–61]. In particular at calyceal or glomerular synapses, spillover-induced desensitization contributes to short-term depression of AMPAR-mediated transmission [62, 63].

The mossy fiber-UBC synapse appears the physiological opposite of the mossy fiber-granule cell synapse. It has very large surface area of synaptic apposition (20-40 μm^2 in rats) with long stretches of continuous PSD and many release sites [22, 64]. Whereas mossy fiber-granule cell synapses tend to get smaller with increasing animal age, mossy fiber-UBC synapses tend to grow larger [23]. Furthermore, while NMDARs remain major mediators of synaptic transmisson in granule cells, they tend to get replaced by AMPARs in UBCs as animals mature [36]. The peculiar structure of the UBC synapse has been hypothesized to trap glutamate in the synaptic cleft for hundreds of milliseconds, saturating postsynaptic receptors and resulting in a (quasi) steady-state receptor activation [36, 37]. A salient feature of excitatory transmission at the UBC synapse is the biphasic EPSC waveform, consisting of a fast 'classical' EPSC followed by a slow tail that decays to baseline in seconds. In many UBCs, the slow EPSC first rises to peak in 200-500 ms before decaying to baseline. This unusual resurgent EPSC waveform is believed to be caused by steady-state activation of AMPARs with a bell-shaped dose-response curve. Such biphasic EPSCs resulting from steady-state AMPAR activation have also been observed at a calyceal synapse in cochlear nucleus, albeit in a less prominent fashion [62].

Several pieces of evidence indicate that slow resurgent EPSCs in UBCs are due to AMPAR activation by slowly diffusing glutamate. First, the EPSC is sensitive to cyclothiazide (an AMPAR desensitization blocker) and CNQX (an AMPAR antagonist), pointing to mediation by AMPARs [36]. Furthermore, its shape is affected by modulating presynaptic release probability and by blocking glutamate transporters, indicating that glutamate is activating AMPARs throughout the entire duration of the slow current [37]. Finally, the slow EPSC is relatively insensitive to temperature, as the slow decay time constant remains $\sim$ 450 ms even at physiological temperature [45]. This is consistent with an underlying molecular diffusion process, which is only weakly temperature dependent (bulk $Q_{10} \approx 1$).

In this chapter the nature of UBC excitatory synaptic transmission is further investigated, by using several different patterns of mossy fiber stimulation in mouse cerebellar slices, while obtaining whole-cell patch-clamp recordings from postsynaptic UBCs. As an initial experiment, the steady-state assertion of the glutamate hypothesis was tested, by using prolonged regular stimulation patterns to obtain steady-state EPSC waveforms as a function of stimulation frequency. Then, short regular stimulation trains were used to investigate temporal integration of AMPAR-mediated EPSCs and the timing of the slow resurgent EPSC. Earlier studies have generally considered the UBC EPSC as a stereotyped waveform [36, 37, 45, 47]. This assertion was re-examined, and the temporal characteristics of slow UBC EPSCs were characterized. Finally, a mechanistic description of EPSC generation was developed on the basis of a kinetic AMPAR model. A direct result of the integrative properties of the synapse was the ability for individual UBCs to controllably extend slow synaptic transmission delays. Such functionality is of particular relevance in the context of cerebellar timing and adaptation, which is further discussed at the end of this chapter.

2.2 Results

2.2.1 EPSC characteristics

Whole-cell patch-clamp recordings were obtained from UBCs in lobule X and the ventral part of lobule IX in cerebellar slices of 5 to 7 weeks old mice. UBCs were identified visually by the size of the soma, and in several cases a fluorescent dye was added to the pipette medium, unveiling the characteristic UBC morphology (Figure 2.1A). Further confirmation was obtained from the typical large membrane capacitance ($>$ 10 pF). The signal amplifier was used in voltage-clamp mode, and the membrane potential was held at $V_{hold} = -80$ mV, unless stated otherwise. All experiments were performed in the presence of 100 μM picrotoxin and 1 μM strychnine to block GABAergic and glycinergic inhibition. To evoke EPSCs a glass stimulation pipette was placed in the white matter or granule cell layer to electrically stimulate the presynaptic mossy fiber. For this study only short-latency (1-2 ms), biphasic EPSCs were selected ($n = 22$). Figure 2.1B shows examples of responses from two UBCs. The initial fast EPSC peak typically rose to peak within ~0.5 ms and decayed with a time constant of ~2 ms. The fast EPSC peak was followed by a slow current tail that decayed back to baseline with a time constant of hundreds of milliseconds. Throughout this chapter the current level just prior to stimulation will be referred to as the 'baseline' or 'base' amplitude, whereas the 'peak' amplitude is used to refer to the maximal fast EPSC, relative to the baseline amplitude. Parameters of evoked EPSCs are summarized in Figure 2.1C. Either a potassium-based ($n = 15$) or a cesium-based ($n = 7$) intracellular medium was used, and no significant difference was found between the two conditions for any of the EPSC parameters ($p > 0.3$ for all parameters, Mann-Whitney U test).

In rat UBCs, the initial fast EPSC is often followed by a transient increase of inward current, which rises to peak in hundreds of milliseconds [36, 37, 45]. This finding was reproduced here in mouse UBCs by applying a burst stimulation protocol, as shown in Figure 2.1D for the same cells as in Figure 2.1B. In response to 5 pulses at 200 Hz, a slow EPSC was observed that rose to a maximal amplitude of ~20 pA in ~200 ms in these two cells. Bath co-application of NMDAR antagonist D-APV and AMPAR antagonist CNQX abolished the fast response as well as the subsequent slow wave, confirming their synaptic nature (grey traces). As exemplified by these recordings, the amplitude of the fast EPSC was generally unrelated to the amplitude of the slow EPSC. Figure 2.1E plots the amplitude ('base amp.') versus the delay of the slow current maximum, for 15 UBCs. The plotted values represent the maximal delays we were able to evoke for a given cell.

2.2.2 EPSCs are generated from a steady-state

According to the glutamate-entrapment hypothesis, the origin of the slow EPSC tail current lies in the (quasi) steady-state activation of postsynaptic receptors, due to prolonged presence of glutamate in the synaptic cleft. To test this hypothesis, a stimulation protocol was designed to expose the UBC synapse to stepwise increasing glutamate concentrations in a reproducible way. Regular stimulus trains were applied at stepwise increasing stimulation frequencies in the range 0-20 Hz. Each stimulation frequency was maintained for at least 5 seconds, ensuring that peak and baseline amplitudes settled to their final stationary values. EPSCs during the last 4 seconds of a train were averaged, and corresponding values of EPSC peak

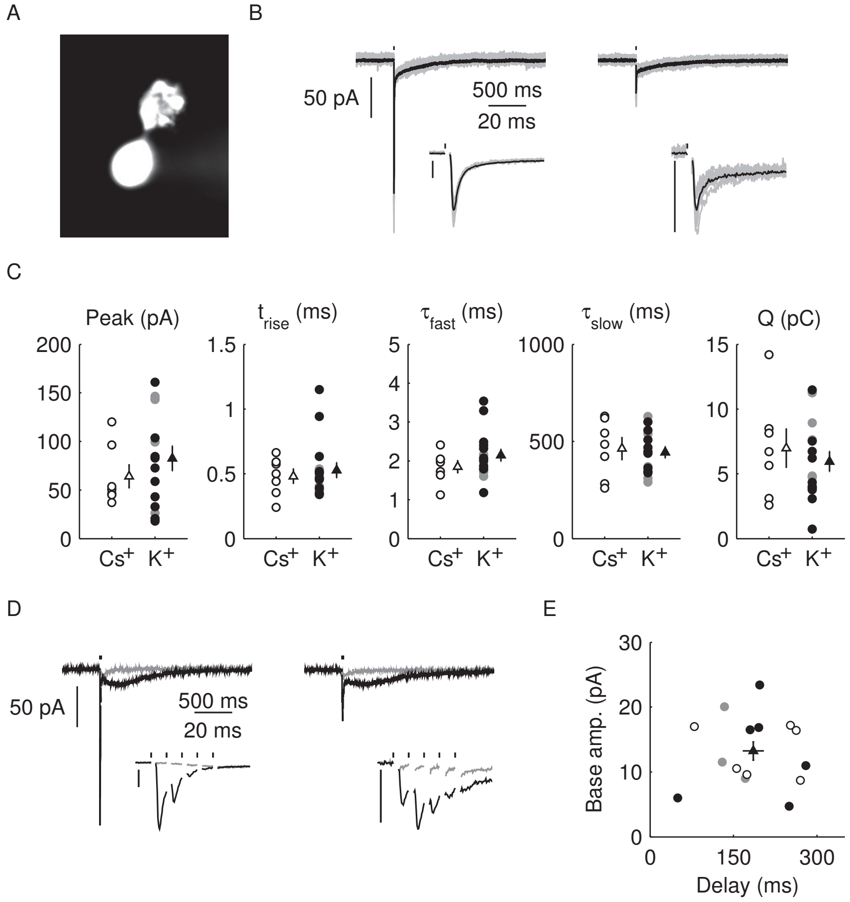

Figure 2.1: Properties of the EPSC. (A) Epifluorescence image of a UBC filled through the patch pipette with a fluorescent dye. (B) Example recordings of responses to a single presynaptic stimulus from two different UBCs. The insets show an enlargement of the fast EPSC, the vertical scalebars indicate 50 pA in all cases. Times of stimulation are indicated by vertical black bars, artefacts were removed for clarity. Black traces are averages of 10 sweeps shown in grey. (C) Summary of EPSC properties from 22 UBCs, left to right: peak amplitude, 20-80 % rise time (t_{rise}), decay time constant of the fast EPSC (τ_{fast}), decay time constant of the slow tail (τ_{slow}), total charge transferred (Q_{trans}). Filled dots, K$^+$-based internal. Open dots, Cs$^+$-based internal. All data were taken at $V_{hold} = -80$ mV, except for the filled grey dots, which were taken at $V_{hold} = -90$ mV (n=2) or $V_{hold} = -100$ mV (n=3). Average and standard error of the mean (SEM) are shown in red. (D) Response to burst stimulation (5 x @200 Hz) of the same cells as in (A), averages of 5 sweeps. (E) Amplitude versus delay of the maximal slow EPSC from 15 UBCs.

amplitude, baseline amplitude, and baseline slope were determined. These values will be referred to as 'steady-state' values from here on.

Examples of steady-state EPSCs are displayed in Figure 2.2A for five frequencies. Perhaps not surprisingly, steady-state EPSC peaks declined monotonically with stimulation frequency. However, it is apparent from these examples that the amplitude and slope of the steady-state EPSC baseline depended in a non-intuitive way on the stimulation frequency. The steady-state baseline amplitude first increased with increasing stimulation frequency until a maximum was reached at 10 Hz.

The baseline amplitude then decreased for higher frequencies, and the slope of the baseline correspondingly reversed sign. The three parameters (peak, base and slope) are plotted as a function of stimulation frequency in Figures 2.2B and 2.2C for 8 UBCs, recapitulating the described steady-state behavior. By stepping the stimulation frequency in this way, the biphasic EPSC waveform was effectively sampled by progressively stepping the baseline current through different phases of the slow tail. This behavior is inconsistent with expectations from ordinary (leaky) integration of slow synaptic currents, strikingly demonstrating the special mode of excitatory transmission at the UBC synapse.

2.2.3 Graded delays of slow EPSCs

Vestibular mossy fibers *in vivo* typically display background discharge rates of 5-10 Hz in anesthetized mice [20, 44]. The development of EPSC amplitudes was therefore investigated during trains of presynaptic stimulation. Figure 2.3A shows an example recording of the response to a regular train of 15 stimuli at 20 Hz. Three things are immediately apparent from the trace: first, the EPSC peaks displayed strong adaptation during the initial stage of the train. Second, the slow EPSC tails fused, forming a persistent baseline current. Finally, after the last stimulus in the train, the baseline current transiently resurged, in a manner that was reminiscent of the slow responses to burst stimulation in Figure 2.1D. Examples of such tail currents for different stimulation frequencies are shown in the inset. The latency of the maximal slow current was graded; it increased when the frequency of the preceding stimulus train was increased.

Figure 2.3B shows the development of EPSC peaks during regular 20 Hz stimulation for 11 UBCs. Peaks depressed in all cells tested, on average by $75 \pm 6\%$ after the first 5 stimuli. Depression then continued at a much slower pace, reaching on average $79 \pm 5\%$ after 10 stimuli. The inset shows EPSC peak ratio (relative to the first EPSC) of the 2^{nd} and 5^{th} peak in a train, as a function of stimulation frequency. The former thus corresponds to a classical paired-pulse experiment. Notably, significant depression of the EPSC peak already occurred at stimulation frequencies as low as 2 Hz.

Under natural conditions, mossy fiber activity is irregular due to the occurrence of bursts and pauses resulting from modulation by sensory inputs, for example. To investigate EPSC integration under such conditions in the *in vitro* preparation, we stimulated mossy fibers with irregular interstimulus intervals (ISIs). Figure 2.3C shows example traces recorded during irregular stimulation at average frequencies

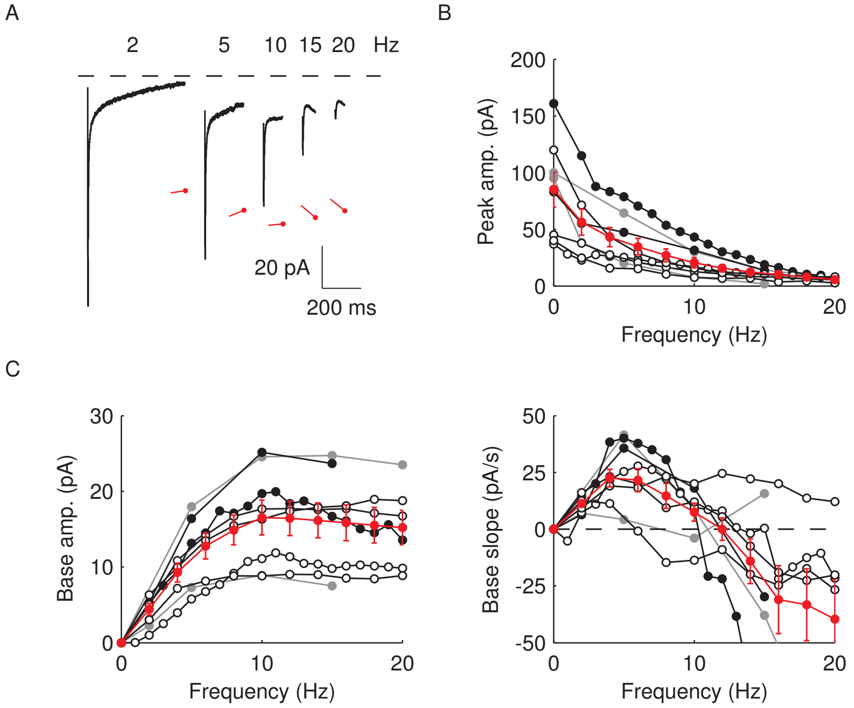

Figure 2.2: Steady-state EPSCs. (A) Examples of steady-state EPSCs, derived from regular stimulation protocols at increasing frequencies. The red markers denote the amplitude and slope a the end of the EPSC, with a vertical offset for clarity of display. (B) and (C) Summary of steady-state EPSC peaks, baseline amplitudes and baseline slopes as a function of stimulation frequency for 8 UBCs. As sample frequencies varied between cells, averages and SEM (red) were obtained by interpolation.

of 5 Hz (left panel, blue) and 10 Hz (right panel, red). Note that for these experiments single (long lasting) trials were used, so the traces are not averages of multiple sweeps. As before, the EPSC peaks were detected, as well as the baseline amplitudes just prior to stimulation. These quantities are plotted against each other below the example traces, for instantaneous frequencies up to 20 Hz. The black overlayed curve was derived from the stimulation protocol described in Figure 2.2 for this particular cell, and thus represents steady-state amplitudes of the baseline and corresponding fast EPSC. The overlap of the black curve with the data points derived from the irregular stimulation protocol indicates that EPSCs were generated from a steady-state, even during irregular stimulation patterns.

As was shown in Figure 2.3A, regular stimulation trains were followed by slow resurgent EPSCs with controllable delays. Such slow EPSCs were also generated during irregular stimulation, as shown in Figure 2.3D. Here, periods with ISI >= 350 ms were selected from the stimulation trials and ordered according to the current amplitude at time 350 ms. These current traces were then stacked and displayed as a heatplot. It is apparent from the plot that slow EPSCs were activated with a wide range of delays, providing further illustration of their graded timing. The properties of slow EPSC timing in response to regular stimulation trains are summarized in Figure 2.3E, which plots the delay of the maximal slow EPSC as a function of the stimulation frequency for 11 UBCs. Delay was positively related to the stimulation frequency and typically extended up to 200 ms. Such graded persistent activation allows UBCs to controllably extend transmission delays in relation to the frequency and duration of presynaptic activity.

2.2.4 Slow EPSC delays result from steady-state AMPAR activation

To elucidate the mechanism underlying slow EPSC generation, EPSCs were simulated using a kinetic AMPAR model from Raman and Trussell [59], consisting of 4 closed states, 2 desensitized states and 3 open states (Figure 2.4A). Qualitatively, the kinetics of the model were characterized by fast desensitization and a bell-shaped dose-response curve. It was used previously to simulate EPSCs at a calyceal somatic synapse in cochlear nucleus [62] and at the mossy fiber to granule cell synapse [63]. Figure 2.4A shows the open probability P_o (sum of three open states) of the model in response to a brief pulse of glutamate (4 mM, decay time $\tau = 0.15$ ms), for increasing levels of the background glutamate concentration G. When G was stepwise increased from 0 to 100 μM, the distribution of occupied model states increasingly shifted towards desensitized states, resulting in a decreasing P_o amplitude (P_{peak}). The relation between P_{peak} and G is plotted in Figure 2.4B, showing that P_{peak} was a monotonically decreasing function of G. The dose-response curve, that is the steady-state open probability as a function of background glutamate concentration G, was bell-shaped (P_{base}, red curve); it first rose to a maximum at around $G = 80$ μM, and then fell in response to increasing steady-state glutamate exposure. Thus, under steady-state conditions both EPSC peak and base currents were instantaneously related to G.

Diffusion modeling has indicated that in a synapse with multiple release sites, glutamate equilibrates rapidly (within 1 ms after release) between sites, resulting in a locally flat spatial concentration profile that decayed exponentially to zero [60] (see Chapter 3). Here the following simplified model was used to describe the time course of background glutamate concentration in the cleft: (1) Peak and base response were generated from two separate sites. (2) The background glutamate concentrations G_{peak} and G_{base} of the two sites were proportional with a factor α. (3) G_{base} rose instantaneously with amount $Q_1 + Q_2$ upon glutamate release, and decayed biexponentially with time constants τ_1 and τ_2.

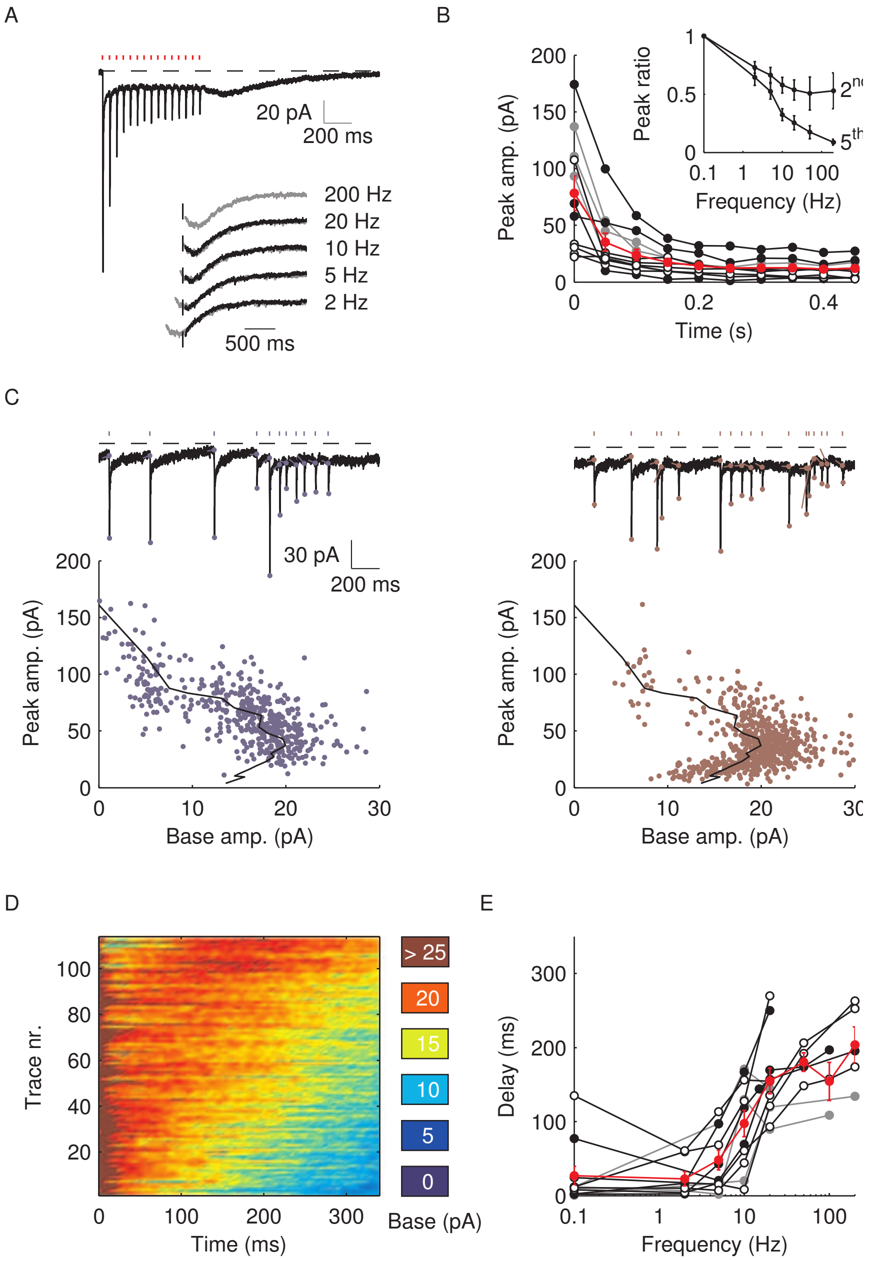

Figure 2.3: Delayed EPSC generation. (A) UBC response to a regular 20 Hz stimulus train, the inset shows example traces of slow waves following regular stimulation at different frequencies. The 200 Hz curve was redrawn in grey beneath each trace for comparison. The vertical dotted line was drawn 20 ms after the final stimulus in the train. (B) Adaptation of EPSC peaks during 20 Hz stimulus trains ($n = 11$), average and SEM are shown in red. The inset shows EPSC peak ratio (relative to the first EPSC) of the 2^{nd} and 5^{th} peak in a train, as a function of train stimulus frequency. (C) Example traces of responses to irregular stimulation (single sweep, 90 s) at average frequencies 5 Hz (top left, blue) and 10 Hz (top right, red). Stimulation times, peaks of the fast EPSCs and baseline currents prior to stimulations are indicated by markers. In the bottom panels, EPSC peaks are plotted versus the corresponding baseline currents for 5 Hz (bottom left, blue dots) and 10 Hz (bottom right, red dots). Steady-state values derived from Figure 2.2 are replotted here for this particular cell (black curve). (D) Heatmap of stacked traces of slow synaptic current during irregular stimulation. Traces with ISIs $>= 350$ ms were selected and ordered according to the value of baseline current at time 350 ms. (E) Latency of the maximal slow EPSC following regular stimulation, as a function of frequency for 11 UBCs. Averages and SEM are plotted in red.

These assumptions are based on the synaptic configurations shown in Figure 2.4C [37]: (1) Glutamate release sites with no opposing PSD (left panel). This site is not directly involved in generating a response, but released glutamate can spread to other sites. (2) PSD not directly opposed to release sites (middle panel). This site generates the steady-state response, driven by background glutamate concentration G_{base}. (3) Release sites directly opposed to PSD (right panel). This site generates the fast peak response, and experiences a background glutamate concentration G_{peak} that was a fraction α of G_{base}.

An estimate of the value of α could be obtained without using explicit assumptions on the time course of G, by directly associating P_{peak} with P_{base}, as shown in Figure 2.4D. By circumventing G in this way, the resulting curve (black) could be directly compared to the steady-state data from Figure 2.2. A least squares fit to the steady-state baseline values resulted in $\alpha = 0.22$.

The glutamate model thus had four parameters: two release quantities ($Q_{1/2}$) and two decay time constants ($\tau_{1/2}$). In order to translate glutamate concentrations into channel open probability during stimulus trains, a steady-state approximation was implemented by using the curves in Figure 2.4B as a lookup table. This instantaneously related the peak and baseline amplitudes to the underlying glutamate concentration. This procedure allowed for estimating the effective background glutamate concentration in the synaptic cleft, by fitting simulated baseline P_{base} to experimental EPSC baseline amplitudes. One additional parameter A_{base} was introduced to translate open probability into current (pA). An example fit result is shown in the top panel of Figure 2.4E, for stimulus trains at 3 frequencies. Note that the black curves all resulted from the same model parameters, and thus do not represent individual fits; the model was fitted simultaneously to base amplitude data at different frequencies, which were treated as a single dataset. An upper limit of 200 μM was imposed on the fit procedure, to prevent runaway parameter values in 4 cases. Fit results from 11 UBCs are summarized in the lower panel of Figure 2.4E, where $Q_{1/2}$ and $\tau_{1/2}$ corresponding to each cell are represented as a set of connected coordinates. One cell was better described by a single-exponential decay (single black dot). The average values obtained from this procedure for glutamate decay time constants were $\tau_1 = 96 \pm 25$ ms and $\tau_2 = 587 \pm 75$ ms (single-exponential value excluded). The slow time constant matched well with the (independently determined) slow time constant from the EPSC tail current in Figure 2.1C. In Figure 2.4F, these time constants were used to obtain an estimate of the glutamate release quantities from fitting to steady-state data from Figure 2.2. The procedure resulted in an excellent fit to the steady-state baseline data.

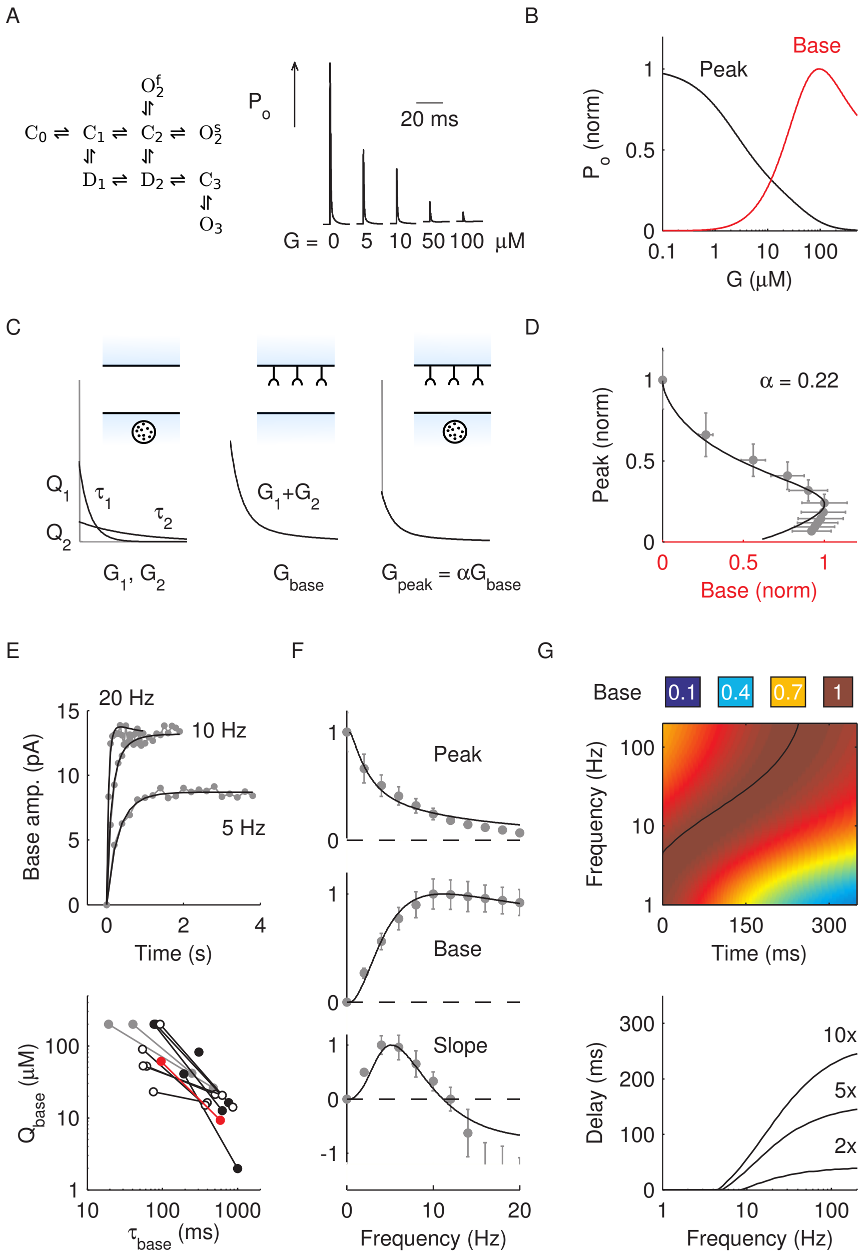

Figure 2.4: AMPAR model simulations. (A) Schematic representation of the AMPAR model from Raman and Trussell [59]. Traces are simulation results of total (summed) receptor open-probability P_o in response to a 4 mM pulse of glutamate for 5 values of the ambient glutamate concentration G. (B) Peak P_o (P_{peak}) in response to a brief 4 mM glutamate pulse (black trace) as a function of G. The steady-state P_o (P_{base}) as a function of G is plotted in red. (C) Glutamate release and decay model. The background glutamate concentration G was modeled as an instantaneously released quantity, which decayed biexponentially to zero (black). The grey curves represent the fast glutamate peak (truncated) underlying the fast EPSC. Further details are described in the main text. (D) P_{peak} as a function of P_{base} (black curve). The steady-state AMPAR model was fitted to experimental steady-state data (grey) with fit parameter α. (E) Results of fitting the biexponential glutamate decay model to EPSC base amplitudes obtained from regular stimulation experiments (top panel). Each fit was characterized by a pair of release amplitudes (Q_{glut}) and decay time constants (τ_{glut}), results are shown in the bottom panel for 11 UBCs. *(continued on following page)*

Figure 2.4: *(continued)* (F) Model fit to steady-state data of Figure 2.2. Slope measurements became increasingly inaccurate at higher stimulation frequencies, and the bottom graph was therefore truncated. Fit results are shown in red in Panel E. (G) Top panel: P_{base} as a function of time following 10 regular stimuli at varying stimulation frequency. The black curve denotes the time of maximal P_{base}. Bottom panel: Delay of the maximal P_{base} as a function of stimulation frequency for 2, 5 and 10 stimuli.

The fit parameters are shown in red in Panel E, and matched well with the fit results from the transient baseline adaptation experiments.

It was thus possible to describe transient adaptation, as well as steady-state EPSC parameters using the steady-state properties of the AMPAR model. As a consequence, the model also naturally reproduced the variable slow EPSC delays. The top panel of Figure 2.4G shows the results from a simulation in which the model was first stimulated by 10 glutamate pulses, and subsequently left to decay (from time $t = 0$ in the plot) according to the steady-state fit parameters. Due to increasing accumulation of glutamate, a delayed AMPAR activation gradually developed with increasing stimulation frequency. The black overlayed curve represents the maximal P_{base}, and corresponds to the '10x' curve in the bottom panel. Delay was a monotonic function of the stimulation frequency and the number of stimuli in the train, and provides a direct mechanistic interpretation of the data in Figure 2.3E.

2.3 Discussion

The role of spatial transformations in the input layer of the cerebellum is a topic of debate, inspired by the anatomy of divergent mossy fiber-granule cell projections [17, 18]. In contrast, less attention has been paid to the origin of temporal transformations in the granule cell layer, and mechanisms have been mostly restricted to the millisecond time scale [65]. Here it is shown that UBCs in the granule cell layer of the mouse produced slow resurgent EPSCs that could be activated with variable delays up to hundreds of milliseconds, in direct relation to the frequency and number of presynaptic stimuli. Furthermore, a mechanistic interpretation of EPSC integration is provided, by combining customized stimulation patterns with a kinetic model of AMPAR activation. These results show that UBCs can provide a basis for temporal coding in the cerebellar cortex.

2.3.1 EPSC integration

Considering the large number of glutamate release sites and the extensive area of PSD, the UBC EPSC peak is surprisingly small, comparable in amplitude to granule cell EPSCs [49, 53]. Moreover, during regular trains of presynaptic stimulation, EPSC peaks displayed significant depression within the first 5 stimuli, that was almost complete at a stimulation frequency of 20 Hz. This result stands in stark contrast to mossy fiber-granule cell EPSCs, for which short-term depression is virtually absent at comparable rates [20, 50]. Furthermore, the relatively large capacitance of the UBC membrane reduces the capacity for fast EPSC components to depolarize UBCs, as currents are effectively low-pass filtered while charging the cell (Figure 1.4B). UBC synaptic physiology thus appears particularly suited to slow signal transmission.

Due to relatively high background activity, combined with slow glutamate removal from the cleft, the physiological state of the UBC synapse *in vivo* is likely characterized by long periods of continuous exposure to glutamate. During long-lasting stimulation patterns in our *in vitro* preparation, UBCs generated slow resurgent EPSCs with variable delays that were well described as resulting from steady-state AMPAR activation. Notably, modulation of the slow EPSC delay took place with little variation in EPSC amplitude, allowing for a fully independent representation of temporal intervals. The extent of the delay also varied widely between cells, which by itself could have important functional implications [42].

Slow depolarizations with graded delays were also recently observed in UBCs in response to mossy fiber bundle stimulation, due to a non-synaptic activation [47]. Such a mechanism could diffusively activate the granule cell layer with delays up to seconds. This type of UBC activation is distinctly different from the type described in our current work in three ways: First, it requires electrical stimulation of the entire mossy fiber bundle at high intensity (typically 10-20 pulses at 100 Hz). Second, UBC depolarization is mediated through a diffusive non-synaptic mechanism, and is therefore most likely not cell-specific. Third, the extent of the delay decreases when the frequency, number or intensity of stimuli are increased. These findings stand in contrast on all accounts to the results presented here, and therefore represent a fundamentally different physiological mechanism in the cerebellar circuit.

2.3.2 Model and simulations

Despite the morphological complexity of the UBC synapse, it was possible to capture both transient and steady-state behavior of the slow EPSC baseline using a scalar model for glutamate release and decay. An explanation is that rapid equilibration of glutamate across the synaptic cleft results in a spatially homogeneous glutamate concentration profile, which supports an equilibrium distribution of open channels in a large ensemble of AMPARs. Slow baseline currents can then be simulated as (quasi) steady-state activation of a kinetic AMPAR model, driven by a single effective glutamate concentration (Chapter 3).

Several features of fast EPSC peak adaptation were also described by the model, such as significant depression at stimulation frequencies as low as 2 Hz, and rapid adaptation to nearly full depression at 20 Hz. These observations point to a common underlying mechanism driving EPSC baseline and peak adaptation, as the two parameters co-varied during transient stimulation (Figure S2.7). Nonetheless, the rate of peak adaptation was not in full accordance with steady-state behavior, as would have been expected from the model (Figure S2.8). Furthermore, an additional very slow peak adaptation component was apparent during long stimulus trains, that was not described by the model (Figures S2.6 and S2.5). These discrepancies could for example be explained by presynaptic adaptation processes, which were not simulated here.

2.3.3 Role in cerebellar learning and timing

The cerebellar cortex is crucial for the timed execution of movements [66]. At the cellular level, this task requires accurate neural activity on multiple time scales, to facilitate adaptive output for motor control [42]. The mechanism described in this work allows individual UBCs to tailor transmission delays to match varying degrees of synaptic input. Considering the abundance of UBCs in the vestibulocerebellum, this functionality could be especially relevant to relatively slow compensatory movements of the eyes and head. For example, activation of vestibular mossy fibers (known to signal head velocity [20]) by a strong head movement could be met with a longer signal delay than activation by a weak head movement. The sensitivity of this mechanism might be tuned by presynaptic plasticity, for example by modulating glutamate release probability.

Transmission delays beyond the typical neuronal membrane time constants are of central importance to many models of cerebellum-dependent behavior. Nonetheless, it remains unclear in most cases how such delays could come about. For example, transmission delays are crucial to the process of signal integration in feedback circuits, which might underlie vestibular oculo-motor integration [67]. In models of eyeblink conditioning and vestibulo-ocular reflex (VOR) adaptation the cerebellar granule cell layer is often specifically postulated as the source of neural transmission delays and tonic signals [68–70], and an eligibility trace with a peak at 200-250 ms has been postulated as a general feature of cerebellum-dependent forms of learning [71]. UBCs are thus well-positioned to provide a robust cellular substrate for representing time intervals in the cerebellar cortex.

2.4 Materials and methods

2.4.1 Slice preparation

Parasagittal slices (250 μm) where prepared from the cerebellar vermis of C57BL/6 mice, 5 to 7 weeks old. The animals where anesthetized by isoflurane inhalation, after which the cerebellum was quickly removed and mounted in a vibratome (Leica VT1000S, Leica Microsystems). Thin sections (250 μm) where cut using a ceramic blade (Campden Instruments) in ice-cold bicarbonate-buffered solution containing (in mM): 90 NaCl, 2.5 KCl, 1.25 NaH_2PO_4, 26 $NaHCO_3$, 0.5 $CaCl_2$, 4 $MgCl_2$, 25 D-glucose, 75 sucrose and 1 kynurenic acid (bubbled with 95% O_2, 5% CO_2). After cutting, slices were allowed to recover for 1 h in an artificial cerebrospinal fluid (ACSF) at 34 °C containing (in mM): 127 NaCl, 2.5 KCl, 1.25 NaH_2PO_4, 26 $NaHCO_3$, 1.5 $CaCl_2$, 1 $MgSO_4$ and 20 D-glucose (bubbled with 95% O_2, 5% CO_2). Slices where then stored in ACSF at room temperature for up to 6 hours.

2.4.2 Electrophysiology

For electrophysiological recordings slices were transferred to a perfusion chamber mounted in an upright microscope (modified Olympus BX51), equipped with infrared differential interference contrast (IR-DIC) optics and whole-field epifluorescence imaging (LaVision Biotec). Slices were continuously perfused with bubbled ACSF (2 ml/min) at room temperature (22-24 °C). In all experiments ACSF was supplemented with 100 μM picrotoxin and 1 μM strychnine, to block GABAergic and glycinergic inhibition. Cells in lobule IX or X were visualized with a 40X water immersed objective (Olympus LUMPLFLN) and a digital camera (AxioCam MRm with AxioScop software, Carl Zeiss). Patch pipettes were pulled from filamented borosilicate glass capillaries (Warner Instruments) with a horizontal puller (Sutter Instruments P-97), resulting in a typical resistance of 7-8 MΩ. Pipettes were filled with a potassium-based intracellular solution containing (in mM): 140 K-gluconate, 0.2 EGTA, 10 HEPES, 4 Na_2ATP, 0.4 Na_3GTP and 2 $MgCl_2$ (290 mOsm, pH 7.3 set with KOH), or a cesium-based intracellular solution containing (in mM): 140 $CsMeSO_3$, 1 EGTA, 10 HEPES, 4 Na_2ATP, 0.4 Na_3GTP, 2 $MgCl_2$, 0.2 $CaCl_2$, 1 QX-314 and 1 TEA-Cl (290 mOsm, pH 7.3 set with CsOH). UBCs were visually identified by their typical soma size (slightly larger than granule cells), and morphology was confirmed in several experiments by supplementing the intracellular solution with a fluorescent dye (20 μM Alexa-Fluor 488, Invitrogen). As a reference electrode an Ag/AgCl wire was connected to the bath through an agarose salt bridge. Whole-cell patch-clamp recordings were performed using an Axon Multiclamp 700B amplifier (Molecular Devices), and data sampled through an Axon Digidata 1440 in combination with pClamp acquisition software (Molecular Devices), or through an onboard PCI card (NI PCI-6259, National Instruments) controlled by custom MATLAB routines (MathWorks). Signals were typically sampled at 20 kHz, and filtered at 10 kHz. The holding potential during voltage-clamp recordings was -80 mV (unless otherwise stated). The identity of UBCs could be confirmed by their whole-cell capacitance ($C_m = 17 \pm 1$ pF, n=22). Access resistance ($R_a = 25 \pm 1$ MΩ, n = 22) was compensated ~60%. Stocks of D-APV and CNQX (Tocris Bioscience) were prepared in water, and stocks of picrotoxin and strychnine (Sigma-Aldrich) were prepared in DMSO. These were stored in aliquots at -20 °C. Kynurenic acid (Sigma-Aldrich) was dissolved in equimolar NaOH and stored at 4 °C. The final concentration of DMSO in the extracellular solution did not exceed 0.1%.

2.4.3 Electrical stimulation

Current pulses were generated by an isolated pulse stimulator (A.M.P.I.) and delivered to the tissue through a double or single barrel borosilicate glass pipette. Pipettes were filled with HEPES-buffered ACSF, and placed to evoke a reliable synaptic response from the white matter or granular layer. Trigger pulses were generated from an onboard PCI card (NI PCI-6259, National Instruments) controlled by custom MATLAB routines. For irregular stimulus sequences, ISIs were drawn from exponential distributions. When possible at the end of a stimulation experiment 20 μM CNQX and 100 μM D-APV were bath applied to confirm the synaptic nature of the response.

2.4.4 Data analysis

Data were analyzed with custom MATLAB scripts (MathWorks). For analysis of fast EPSCs, traces were low-pass filtered at 2 kHz and subsequently resampled at 5 kHz. For analysis of the slower elements of the EPSC, traces were low-pass filtered at 500 Hz and subsequently resampled at 1 kHz. The current baseline and noise standard deviation (SD) were determined from a 1 s window prior to the start of a stimulus protocol. The peak of an EPSC after stimulation was determined in a 5 ms window from the start of the stimulus artefact, by taking the average of data that fell within 2 SDs of the maximal current in the 5 ms window. A single exponential function was then fitted to the data within the first 20 ms after the peak, to estimate the fast EPSC decay time. EPSC risetime was determined within a 20-80 % peak amplitude window. The decay time of the slow tail was determined by fitting an exponential function to the portion below 80% of the maximum slow current. During stimulus trains, a linear function was fitted to data within 20 ms just prior to a stimulation artefact, to estimate the baseline amplitude and slope at the moment of stimulation. This allowed for calculating the fast EPSC amplitude and risetime during stimulus trains. In some cases the current level at the end of a long stimulation trace did not recover completely to the baseline as it was prior to the start of stimulation, but the difference was never larger than 4 pA and usually less than 2 pA for the cells used in this work. In these cases a linear correction to the baseline was applied. The results of the automated analysis routines were always checked by eye afterwards.

2.4.5 Model and simulations

The kinetic AMPAR model was taken from Raman and Trussell [59] and used here to simulate the fraction of open channels in a collection of AMPARs. The model was implemented in NEURON [72], and simulations were performed in Python [73, 74]. The transition rates were (in ms^{-1}): $\mathrm{C_0 \rightleftharpoons C_1}$ (30 mM^{-1}, 0.3), $\mathrm{C_1 \rightleftharpoons C_2}$ (20 mM^{-1}, 600), $\mathrm{D_1 \rightleftharpoons D_2}$ (20 mM^{-1}, 1.038), $\mathrm{D_2 \rightleftharpoons C_3}$ (3.33 mM^{-1}, 0.22), $\mathrm{C_2 \rightleftharpoons O_2^s}$ $(3, 0.35)$, $\mathrm{C_2 \rightleftharpoons O_2^f}$ $(60, 3)$, $\mathrm{C_1 \rightleftharpoons D_1}$ $(1, 0.3)$, $\mathrm{C_2 \rightleftharpoons D_2}$ $(27, 0.014)$, $\mathrm{C_2 \rightleftharpoons O_2^f}$ $(60, 3)$, $\mathrm{C_3 \rightleftharpoons O_3}$ $(0.006, 2)$. Rates are specified as (forward, backward). States $\mathrm{O_2^s}$, $\mathrm{O_s^f}$ and $\mathrm{O_3}$ were summed to determine the total fraction of open channels. Transitions $\mathrm{C_0 \rightleftharpoons C_1}$, $\mathrm{C_1 \rightleftharpoons C_2}$, $\mathrm{D_1 \rightleftharpoons D_2}$ and $\mathrm{D_2 \rightleftharpoons C_3}$ were multiplied by the glutamate concentration. The bell-shaped dose-response curve of this model is due to the $D_2 \rightleftharpoons C_3$ transition, and is thought to underlie biphasic EPSCs. The $C_3 \rightleftharpoons O_3$ transition is responsible for the persistent open state of the channel at high glutamate concentrations.

To simulate the fast EPSC peak, an instantaneous glutamate pulse was used with 4 mM amplitude and 0.15 ms decay time constant. Analysis based on fitting model parameters to data (Figure 2.4D) were very insensitive to the fast glutamate peak; increasing the amplitude to 6 mM gave identical results. The slow glutamate tail was modeled as an instantaneously released quantity which decayed biexponentially. The glutamate concentration G_{slow} was thus given by

$$G_{slow} = Q_1 e^{-t/\tau_1} + Q_2 e^{-t/\tau_2} \; . \tag{2.1}$$

Here Q_1 and Q_2 are glutamate release quantities, and τ_1 and τ_2 are decay time constants. To calculate the glutamate concentrations just prior to a stimulus within a stimulus train, the glutamate summation can be expressed as

$$G_{base}(N) = \sum_{n=2}^{N} Q_1 e^{-(n-1)T/\tau_1} + Q_2 e^{-(n-1)T/\tau_2}, \tag{2.2}$$

for the N^{th} stimulus in the train, where $G_{base}(1) = 0$. T is the interstimulus interval. The steady-state approximation was obtained in the limit to very large N as

$$\lim_{N \to \infty} G_{base} = \frac{Q_1}{e^{T/\tau_1} - 1} + \frac{Q_2}{e^{T/\tau_2} - 1}. \tag{2.3}$$

By making use of the steady-state dose-response relation of the AMPAR model, the steady-state open probability P_o can be expressed as an instantaneous function of the glutamate concentration G_{base}, that is $P_{base} = P_{base}(G_{base})$. The peak open probablity of the fast EPSC can also be related to G_{base} in the same way. Model parameters were thus Q_1, Q_2, τ_1, τ_2 and A_{base}, which was a factor to convert open probability to current (pA). Parameter values were abstracted by fitting P_{base} to experimental data of EPSC baseline adaptation in the least-square sense, using the function lsqcurvefit in MATLAB (MathWorks).

2.5 Supplementary figures

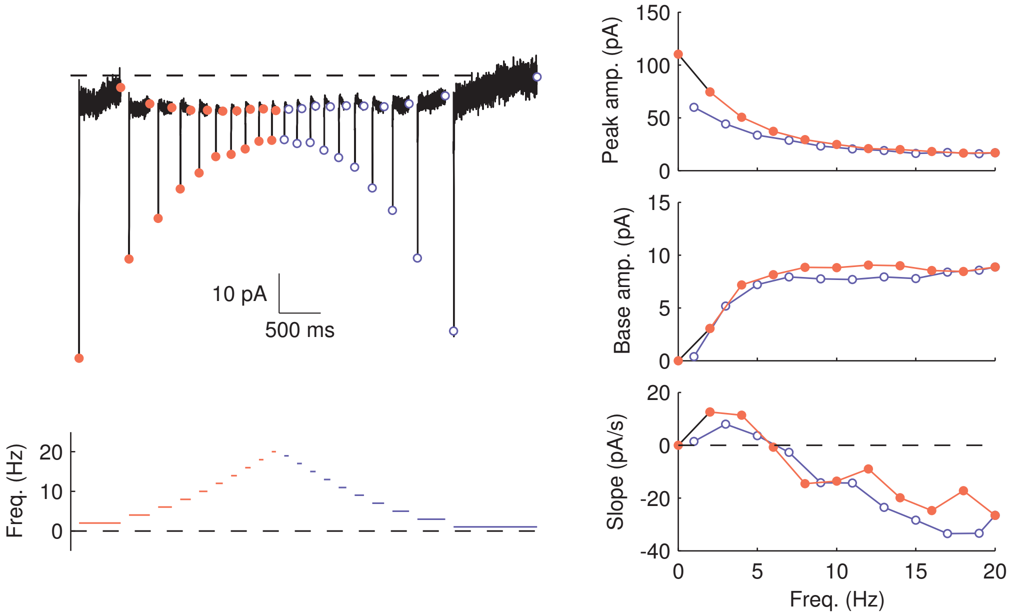

Figure S2.5: Hysteresis of EPSC parameters. Example of the frequency-stepping protocol used to generate steady-state activation curves in Figure S2.7 and Figure 2.2 of the main text. If the EPSC would be fully determined by the (quasi) steady-state activation of AMPARs, we expected that the direction of frequency stepping should not affect the resultant steady-state values, as illustrated in the simulated stepping protocol in Figure S2.6. However, the EPSC peak displayed hysteresis when the stimulation frequency was stepped forwards (red) and backwards (blue) through the frequency range of $0 - 20$ Hz, as shown here in the example trace. This indicated that, apart from the steady-state process described in this work, an additional depression component gradually built up during the stimulation period, with a time constant $\gg 500$ ms (the stimulus train lasted more than 100 seconds). This component did not affect the baseline current, however, as hysteresis was virtually absent in both baseline amplitude and slope.

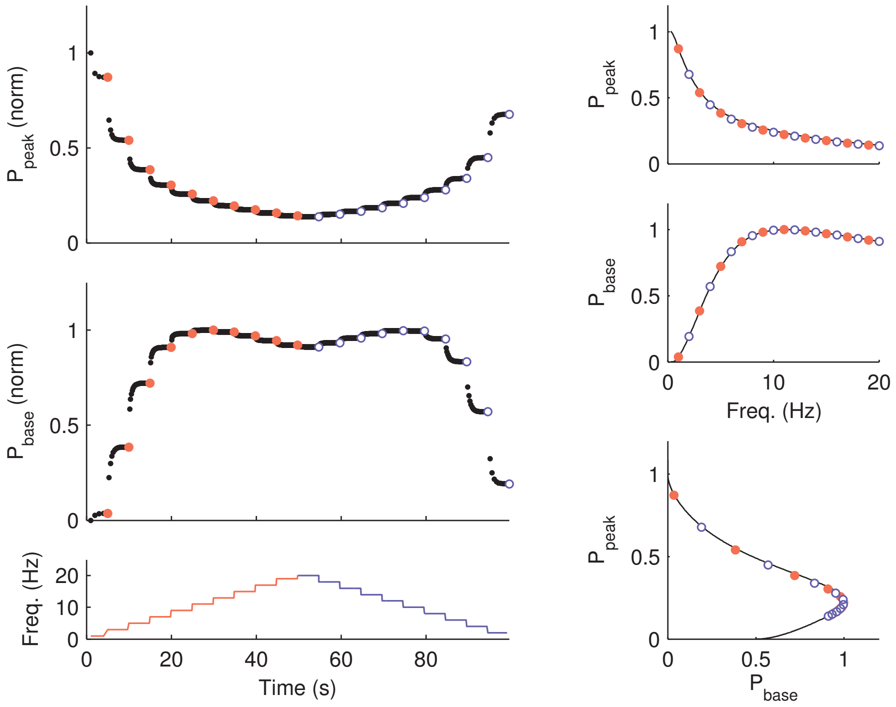

Figure S2.6: Simulated frequency-stepping protocol. Numerical simulation of the frequency-stepping protocol, using the glutamate release and decay model derived in the main text (Figure 2.4). In the main text we made use of the steady-state approximation of AMPAR activation for simplicity, but we show here that the same results could be obtained by numerical integration of the full AMPAR model. As for the experimental protocol, the stimulation frequency was stepped through the range of $1\text{-}20\ \mathrm{Hz}$, in $2\ \mathrm{Hz}$, 5 seconds steps. Peak (P_{peak}) and baseline (P_{base}) open probabilities during the steps were used to generate the plots in the left column. Adaptation of these parameters largely occurred during the first second of a step, although minor adaptation continued for longer periods due to the very slow time constant ($\sim 500\ \mathrm{ms}$) of glutamate removal. The values of P_{peak} and P_{base} at the end of each step were used for the plots in the right column (dots). The grey curves resulted from the steady-state approximation, and matched well with the results from numerical simulation.

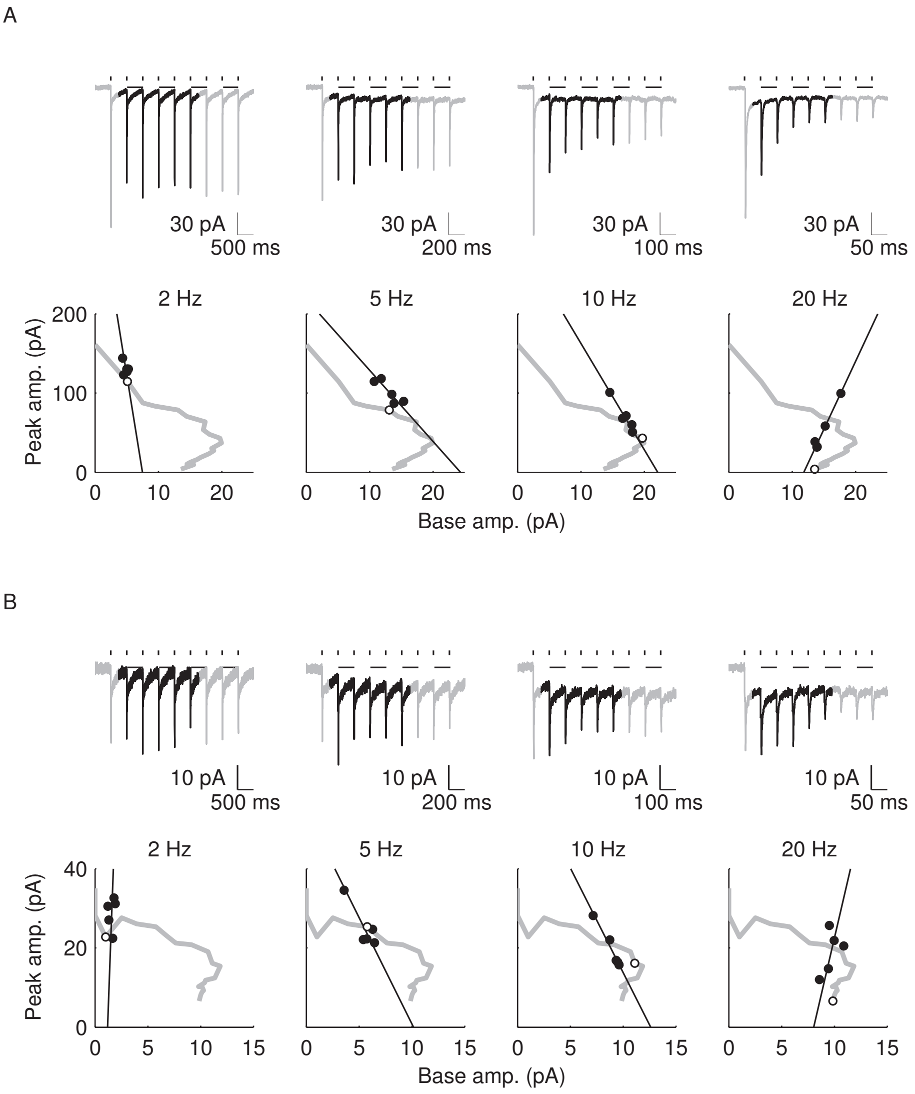

Figure S2.7: Covariation of EPSC parameters. EPSC peaks are plotted as a function of corresponding baseline currents during regular stimulus trains (filled dots) for two different UBCs, with large EPSC peak (A) and small EPSC peak (B). Adaptation occurred within the first six stimuli, the first stimulus in the train was omitted. Covariation of peak and baseline amplitudes was analyzed by comparing the two principal components; vectors corresponding to the largest components are drawn in the panels (black lines). The grey curves represent steady-state values derived from the frequency-stepping protocol described in Figure 2.2 of the main text; the open dots correspond to the relevant frequency in each panel. The level of co-adaptation was quantified as the ratio R_λ of the eigenvalues λ of the covariance matrix, given by $R_\lambda = \lambda_{max}/(\lambda_{min} + \lambda_{max})$. The slopes S_{ad} of the adaptation vectors shifted from negative to positive values with increasing stimulation frequency, the results were $2\ \mathrm{Hz}:\ S_{ad} = -7.8 \pm 14.6$ ($R_\lambda = 0.99 \pm 0.01, n = 7$), $5\ \mathrm{Hz}:\ S_{ad} = -8.6 \pm 2.0$ ($R_\lambda = 0.95 \pm 0.03, n = 10$), $10\ \mathrm{Hz}:\ S_{ad} = -3.0 \pm 5.5$ ($R_\lambda = 0.97 \pm 0.02, n = 11$) and $20\ \mathrm{Hz}:\ S_{ad} = 9.6 \pm 10.5$ ($R_\lambda = 0.98 \pm 0.00, n = 11$).

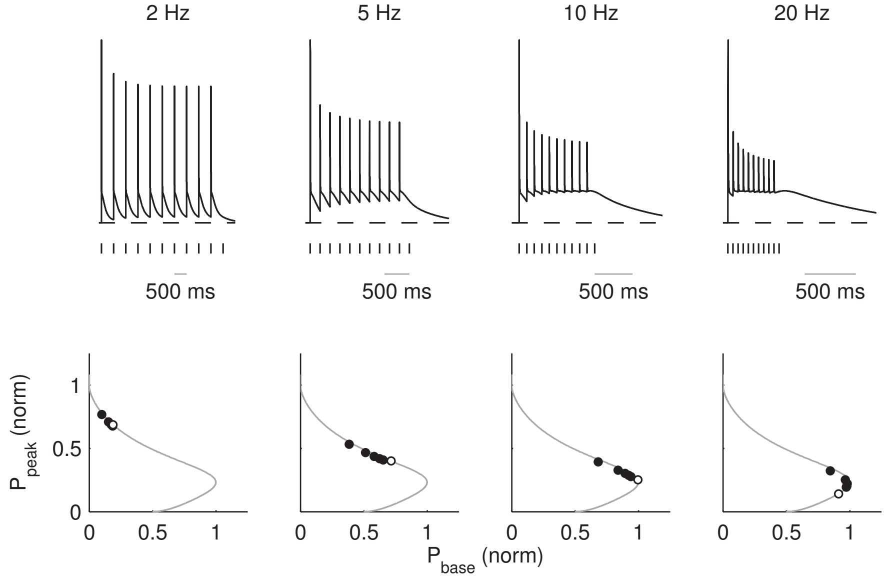

Figure S2.8: Simulated regular stimulation protocol. Numerical simulation of AMPAR activation by regular stimulation trains. The glutamate model derived in the main text allowed for simulating the main qualitative characteristics of short-term adaptation to regular stimuli: Strong depression of P_{peak} already at low stimulation frequencies, and gradual build-up of P_{base} according to the AMPAR dose-response properties. Transient adaptation to frequencies up to $20\ \mathrm{Hz}$ was well described by the steady-state model, as is illustrated in the bottom graphs, which display the simultaneous adaptation of P_{peak} and P_{base} on top of the steady-state curve (grey). The open dots indicate the steady-state values at the relevant frequency.

Chapter 3

Simulation of AMPA receptor-mediated synaptic transmission in unipolar brush cells

Many synapses appear designed to limit the lifetime of neurotransmitter in the cleft to a minimum, allowing temporally restricted point-to-point communication through brief activation of overlying receptors. The mossy fiber to UBC synapse, on the other hand, appears specialized for performing the opposite function: trapping glutamate and activating receptors for long continuous periods of time. In this chapter the characteristic long-lasting AMPAR-mediated EPSCs of UBCs were reproduced using a numerical simulation of glutamate diffusion and AMPAR activation. Artificially slowing down diffusion in part of the model was sufficient to reproduce several features of both fast and slow elements of the EPSC. Incorporating a large number of release sites ensured precision in the timing of the peak of the slow EPSC, by counteracting the unreliability of individual release sites through glutamate pooling.

3.1 Introduction

This chapter addresses the question whether AMPAR-mediated UBC EPSCs, as well as several experimental manipulations thereof, can be reproduced in a computational model incorporating some of the more salient features of the UBC synapse such as the large area of apposition, the presence of many release sites and the steady-state behavior of AMPA receptors. At the level of the synapse, a fundamental choice in model design is whether to implement explicitly the stochastic nature of the microscopic elements. If appropriate probabilistic models and boundary conditions are available for the processes of neurotransmitter release and diffusion, and ion channel receptor conformations, the evolution of the system can be simulated for example by using Monte Carlo techniques [75–77]. However, these techniques are generally computationally costly due to the high level of detail, and it is often beneficial to describe average behavior instead. Kinetic models provide a general tool for describing many processes relevant to neuroscience [78]. They are often employed to simulate the macroscopic behavior of currents flowing through ensembles of ion channels, providing a deterministic average description of the underlying stochastic fluctuations in channel conformation. Receptor-gated ion channels are usually capable of transitioning between numerous different conformations, and the kinetic models capturing their behavior can be accordingly complex. Ion channels involved in synaptic transmission generally display several distinct types of kinetics such as activation, deactivation and desensitization in response to binding of neurotransmitter. Which of these dominates at any given time depends on the properties of neurotransmitter release and diffusion in the synaptic cleft.

The efficiency of kinetic models for describing macroscopic behavior comes at the cost of introducing certain simplifications. For example, they inherently neglect the spatial distribution of channels, and require representing the present number of neurotransmitter molecules as an average concentration in some defined volume. In many cases, the main justification for these simplifications is simply that they can describe experimental data very well. However, it is also recognized at the same time that the stochastic behavior of ion channels is not just a nuisance, but in fact can be an essential determinant of the computational properties of neurons and neural systems.

Most glutamatergic synapses have a small area of PSD with a limited number of postsynaptic receptors (for example $\sim$100 AMPA receptors). The activation of receptors is temporally restricted due to rapid diffusional escape of neurotransmitter to the surrounding space [35]. In such cases, synaptic transmission can usually be simulated accurately by using a single effective glutamate concentration and a single kinetic model for macroscopic description of postsynaptic receptor activation. However, at the UBC synapse a mossy fiber terminal is opposed by large continuous stretches of PSD covering a total area up to 40 μm^2 in rats [31]. Glutamate is released into the cleft volume from many spatially separated release sites, and is believed to remain partially entrapped in portions of the cleft for long periods of time. The resulting prolonged activation of AMPA receptors is believed to be responsible for the typical biphasic UBC EPSC, due to a steady-state current (Chapter 2). It remains unclear however whether AMPA receptors could be capable of generating the relatively large currents that are experimentally observed in the UBC EPSC, as AMPAR steady-state currents are generally very small.

In this chapter a computational model was used to investigate the ability of the glutamate-entrapment principle for generating UBC-like responses. Few experimental details are available concerning the properties of glutamate release, the fine architecture of the synaptic cleft and the kinetic properties of postsynaptic receptors. Nonetheless, UBC-like responses could be readily generated using AMPAR models and glutamate release properties from the literature on the mossy fiber to granule synapse, which has been extensively studied. The main assumption that needed to be made was the introduction of a significant slowing of glutamate diffusion in a major area of the synaptic cleft, as postulated in the glutamate-entrapment hypothesis [36, 37]. The model indicated that the presence of a large number of release sites could ensure the trial-by-trial precision of the shape of the slow EPSC, by counteracting the unreliability of individual release sites through glutamate pooling.

3.2 Results

The large surface area of the UBC synapse presents a challenge for simulating UBC synaptic transmission, due to the computational load of simulating diffusion and thousands of receptor channels. A number of simplifications were implemented to facilitate simulation, while retaining the essential elements of the problem. The synaptic cleft was modeled as a two-dimensional grid consisting of 200x200 nm cells (Figure 3.1A), each defining a volume for an effective glutamate concentration ([glut]). The cell dimensions corresponded to the average area of PSDs from serial electron microscopic reconstructions of mossy fiber rosettes in (non-UBC-containing) glomeruli [63], which was used here as the smallest functional unit in

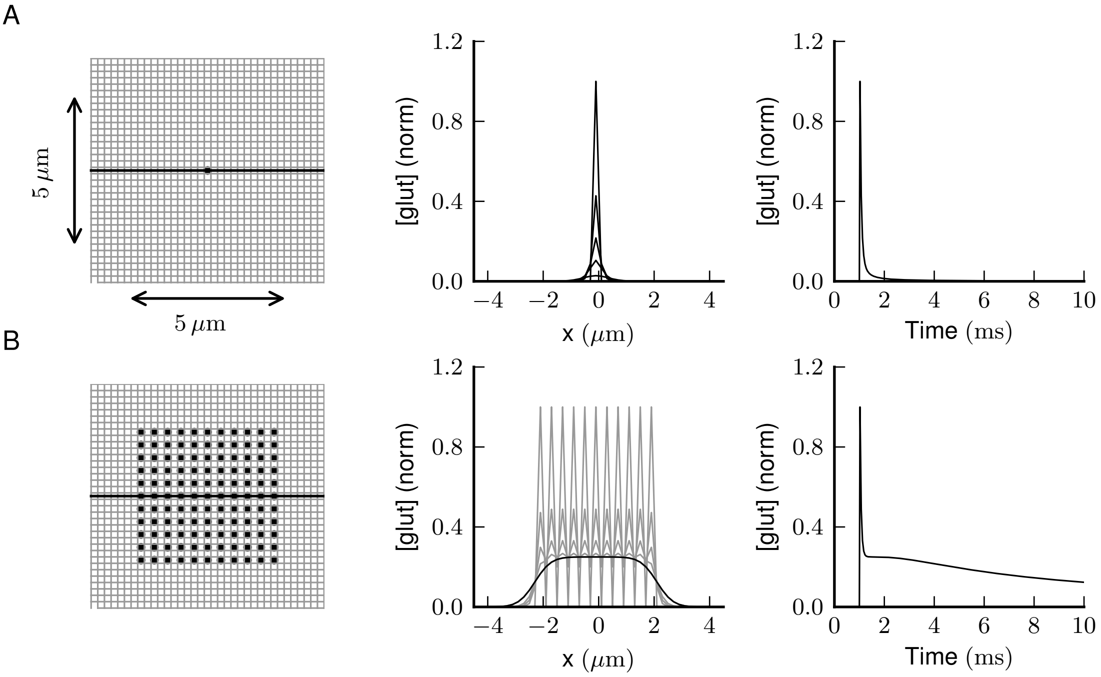

Figure 3.1: Diffusion on a grid. (A) Two-dimensional diffusion from a point-like source (black dot) on a 15×15 µm square grid (only partly displayed). Grid resolution was 0.2×0.2 µm. The middle plot shows glutamate concentration [glut] as a function of horizontal grid position (x, on the black horizontal cross-section) for times 0, 50, 100, 200 and 500 ms. The right plot shows [glut] in the center as a function of time. [glut] dropped by more than 90% within 0.5 ms. (B) Glutamate release from an array of release sites, with inter-site spacing 0.4 µm in both dimensions. Within a fraction of a millisecond, [glut] reached a two-dimensional plateau that decayed to zero with a time constant of ~10 ms.

the model. Glutamate release was simulated as an instantaneous 6 mM increase of [glut] in a cell, which corresponds to approximately 2900 molecules for a 20 nm cleft width [79]. This is a reasonable number for the quantal content of glutamate containing vesicles [80]. Diffusion on the grid was simulated numerically and governed by fluxes calculated per time step on each cell face, with a diffusion coefficient $D = 0.25$ µm^2/ms [77, 81]. This value was derived by correcting $D = 0.76$ µm^2/ms in free solution [82] by a factor 3 to account for the space tortuosity [83]. Although the ambient extracellular [glut] in the cerebellum is unknown, it has been suggested to be high enough to tonically activate NMDA receptors, but too low to significantly activate or desensitize AMPA receptors [84, 85]. A similar conclusion has been obtained in hippocampal slices where the extracellular [glut] was estimated to be tens of nM [86], although it might be higher *in vivo* due to elevated levels of neural activity. The ambient [glut] value was implemented in the simulations by fixing [glut] on the boundaries of the grid at 10 nM. The middle panel of Figure 3.1A shows the spread of glutamate released in the center cell along a cross-section of the grid. The [glut] profile was virtually flat after 500 µs,

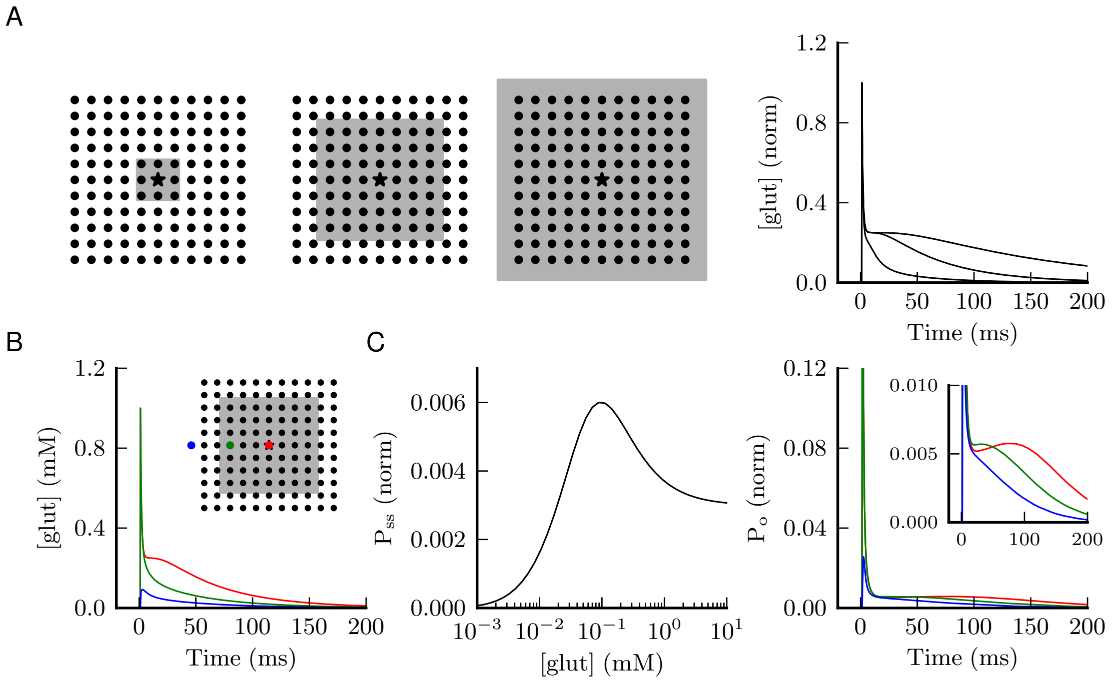

Figure 3.2: Slow AMPAR activation. (A) Simultaneous release from an array of release sites (black dots, as in Figure 3.1). Diffusion was locally slowed down in the grey areas. The right panel shows plots of [glut] in the center of the grid, for the three depicted situations. (B) [glut] in three locations on the grid, for a model with intermediate area of slowed diffusion. (C) The left panel shows the 'bell-shaped' dose-response curve of the AMPAR model used here [59]. The right panel shows responses from AMPAR models on the locations indicated in Panel B.

indicating that most of the glutamate had rapidly escaped from its original release site. This is also clear from the right panel, which shows [glut] in the center as a function of time. This escape time is very similar to that estimated for small synapses, where diffusional escape to the surrounding media is very rapid [35, 77].

In Figure 3.1B the [glut] diffusion profile is shown for a simulation involving simultaneous release from a regular grid of 121 release sites in an area of ~20 µm^2. After release, [glut] equilibrated rapidly between sites, resulting in a virtually flat [glut] plateau after 500 µs (middle panel). The plateau subsequently decayed with a time constant of ~10 ms (right panel). A biphasic [glut] profile thus arose naturally in a model containing many release sites [62], due to a combination of initial rapid local glutamate escape, and subsequent global glutamate pooling.

3.2.1 Slowing down diffusion

Although a biphasic [glut] decay was readily accomplished, the time course of [glut] was much faster than the typical time course of UBC EPSCs, which can be hundreds of milliseconds [36]. It was therefore clear that an additional assumption was necessary in order to achieve such prolonged glutamate entrapment in the model. In Figure 3.2A diffusion was slowed down by lowering the D by a factor 0.04 in increasingly large areas of the model. Due to the discretized nature of the numerical model it was possible to implement spatially nonhomogeneous diffusion by affecting D on cell faces in selected areas of the grid. The [glut] decay in the center was increasingly slowed down when larger parts of the model were affected (right panel). It was evident from the simulations that the value of [glut] differed substantially in different parts of the model, as show in Figure 3.2B. In general [glut] levels were higher in the center than at the edges. This observation is relevant when considering the actual morphology of the UBC synapse, which has large areas of continuous PSD but also many fractured small areas of synaptic apposition. The final synaptic current will thus be a complicated integral of the effects of spatially varying glutamate levels interacting with the kinetic properties of local AMPA receptors.

To simulate EPSCs, a kinetic AMPAR model from Raman and Trussell was used [59], consisting of 4 closed states, 2 desensitized states and 3 open states (see Materials and Methods). It was used previously to simulate EPSCs at a calyceal somatic synapse in cochlear nucleus [62] and at the mossy fiber to granule cell synapse [63]. The dose-response curve, that is the steady-state open probability as a function of background glutamate concentration, was bell-shaped (P_{SS}, red curve); it first rose to a maximum at around [glut] = 80 µM, and then fell in response to increasing steady-state glutamate exposure (Figure 3.2C). This model was also used for the simulations in Chapter 2. The biphasic dose-response curve has been hypothesized to be responsible for generating the typical AMPAR-mediated EPSCs in UBCs [37]. Instances of the AMPAR model were inserted in the model at the three locations indicated in Panel B. As shown in the right panel, both fast and slow components of the AMPAR responses differed between the three locations, as a result of the different local glutamate profiles. The AMPAR model in the center displayed the slow resurgent EPSC reminiscent of UBC EPSCs.

3.2.2 Simulating EPSCs

To simulate EPSCs a basic model was used with the following features. A 6x6 µm grid was used, with fixed-value boundary conditions as before. This was chosen to correspond to the maximal total PSD surface area in rats, which was estimated to 40 μm^2. Release sites were distributed randomly across the model area, at a density of $2.5/\mu m^2$, as was estimated from serial electron microscopic reconstructions

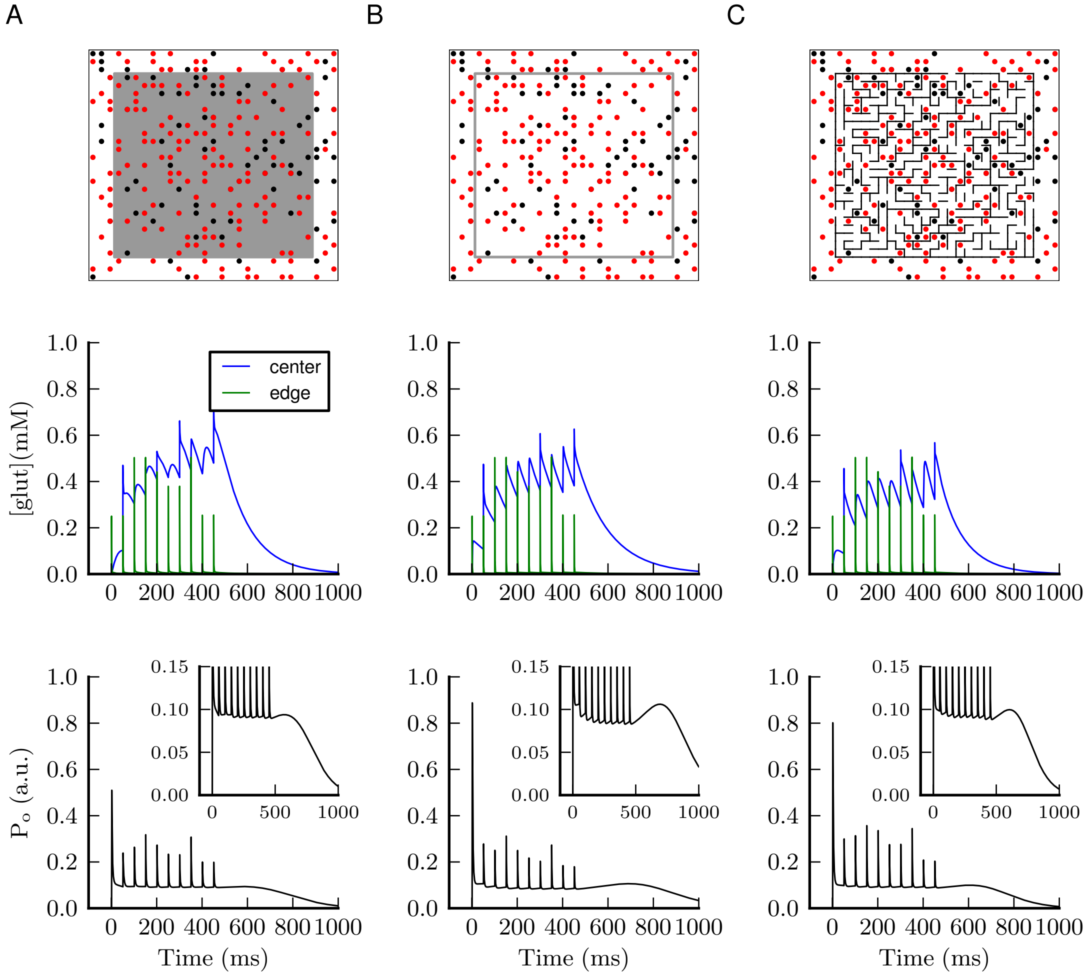

Figure 3.3: Simulating synaptic transmission. Three different implementations for slowing glutamate diffusion in a model with randomly distributed glutamate release sites (black dots) and AMPARs (red dots). An area with slowed diffusion (A), a leaky diffusion barrier (B), and a maze-like structure of diffusion blockades (C). The middle panels show the average glutamate concentration in a square $\sim 3.5\ \mu\mathrm{m}^2$ patch in the center of the model (blue), and in a similar surface area around the edge (green), in response to a train of 10 stimuli at 20 Hz. The bottom panels show simulations of the corresponding AMPAR open probability for each model, summed over the entire surface area (P_O) . The variability in peak P_O was due to the stochastic properties of glutamate release.

of mossy fiber rosettes in (non-UBC-containing) glomeruli [63]. AMPA receptors were also distributed randomly at the same density. The release probability *in vivo* has been shown to be low at several different synapses across the brain [87]. Although this parameter is not known at the UBC synapse, it is also likely low. Increasing the extracellular Ca^{2+} concentration from 1.5 mM to 2.5 mM in slice recordings significantly increased the synaptic response [37], indicating that release probability is low at 1.5 mM Ca^{2+}, close to the estimated 1.2 mM *in vivo* [87]. The release probability at mossy fiber to granule cell connections has been estimated at $P_r \approx 0.6$ in 2 mM Ca^{2+} [50], and it was set in the current simulations at $P_r = 0.3$. Presynaptic effects such as vesicle depletion and replenishment were not simulated here, as these are not likely relevant to the stimulation frequencies below 20 Hz [50].

Simulations were performed using these parameters and implementing a lower diffusion coefficient in part of the model, as in Figure 3.2. As shown in the bottom trace of Figure 3.3A, typical features of UBC EPSCs arose naturally in the model in response to 20 Hz stimulus trains (see Chapter 2). Responses displayed strong short-term depression of fast EPSCs, summation of slow EPSCs to a plateau, and a slow resurgent EPSC tail. The main determinant of these qualitative features was the relative fraction of the model occupied by the grey area, that is, the relative number of AMPARs that experienced fast glutamate removal as opposed to slow glutamate removal. The fluctuations in fast EPSC amplitude in the trace were due to the stochastic nature of the release process. In Panel B a simpler model for diffusion slowing was used, that incorporated a single barrier that slowed diffusion by a factor 150. This model displayed similar characteristics to the model in Panel A. In Panel C diffusion was slowed by implementing a maze-like pattern of hard diffusion barriers, loosely mimicking for example obstacles in the space of the synaptic cleft obstructing glutamate diffusion. It was possible with all three types of models to generate UBC-like responses.

The model in Figure 3.3B was used for further simulations, as it is the simplest of the three. This model was able to reproduce a range of experimental observations, as shown in Figure 3.4. In response to a single stimulus, the model produced a fast initial peak followed by a slowly decaying tail (Figure 3.4A). Due to the stochastic release, the amplitude of the fast peak was quite variable (inset). The amplitude of the slow tail however was much less variable, as it was more determined by an averaged glutamate concentration and the intrinsic properties of the AMPAR model. The model was then used to reproduce three key experimental results that have been taken as support for the glutamate-entrapment hypothesis [37]: (1) The slow EPSC tail occurring in response to a single stimulus transforms into a resurgent 'bump' in response to a burst of stimuli. (2) The same effect occurs when P_r is increased by increasing the extracellular [Ca^{2+}]. (3) When cyclothiazide, an AMPAR desensitization blocker, is applied to the bath the resurgent 'bump' disappears and is replaced by a slowly decaying tail with high amplitude. In Figure 3.4B, the overall glutamate concentration in the cleft was increased by stimulating the model with a high frequency burst (3x @ 100 Hz). This resulted in the development of a slow resurgent response which peaked at around 250 ms. A similar result could be obtained in response to a single stimulus by increasing P_r by a factor 2, as shown by the dashed trace in Figure 3.4C. The

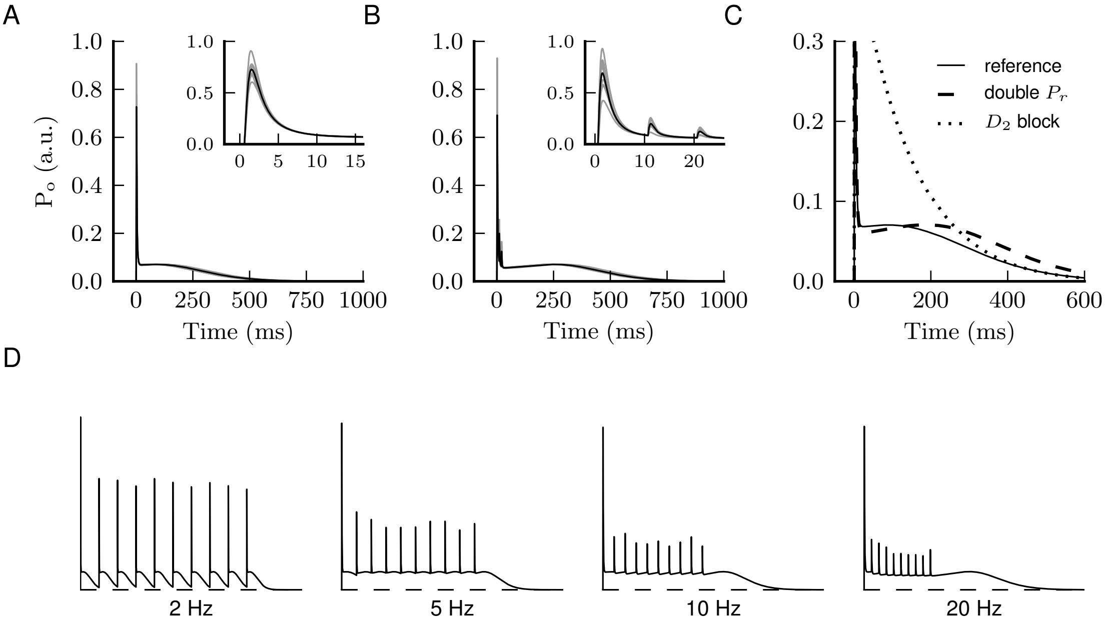

Figure 3.4: Simulating experimental paradigms. (A) P_O in response to a single stimulus. 10 individual trials are shown in grey, and the average is shown in black. Peak P_O displayed considerable variability due to stochastic glutamate release. (B) In response to a burst of stimuli (3x @ 100 Hz) AMPARs displayed a slow resurgent phase of channel activation. (C) Simulated reproduction of two experiments supporting the glutamate-entrapment hypothesis [37]. (1) Increasing P_r converts a slowly decaying tail (solid) into a slow resurgent activation (dashed), in response to a single stimulus. (2) Subsequently blocking AMPAR desensitization eliminates the biphasic response (dotted). (D) Activation of the model by trains of stimuli at four frequencies showed good qualitative agreement with experimental results in Chapter 2. Traces are averages of 10 simulation trials.

dotted trace resulted from blocking all transitions into the D_2 desensitized state of the AMPAR model, mimicking the effect of AMPAR densensitization blocker cyclothiazide. These results thus provided quite good qualitative agreement with the experimental EPSCs. In Figure 3.4D the model was stimulated with regular trains at increasing frequency, to mimic experimental protocols of Chapter 2. As in those experiments, a slow resurgent response gradually developed with increasing stimulation frequency. Finally, the model displayed very similar short-term depression of the fast peaks, even for stimulation frequencies as low as 2 Hz.

3.3 Discussion

The model discussed in this chapter was able to reproduce key features of AMPAR-mediated synaptic transmission in UBCs. Most elements of the model were taken directly from the literature, such as total area of synaptic apposition, the diffusion coefficient in the cleft, the density of release sites, the quantal content and probability of glutamate release, and the kinetics of AMPA receptor gating. Several other elements of the model will be discussed here.

The main assumption that needed to be made was a drastic slowing of diffusion in a large part of the model, in order to reproduce the slow time constants observed in UBC EPSCs. Slowing diffusion naturally allowed the model to reproduce both the short-term depression of fast EPSCs as well as the slow resurgent EPSC tail. The relative area of the model that was affected by the diffusion slowing determined the relative amplitudes of fast and slow elements of the response, as well as the strength of short-term depression. AMPA receptors at the edges of the model contributed mostly to the fast EPSC, while AMPA receptors in the center carried the slow response. In general in the models tested here, the 'edge/center ratio' was an important factor determining the qualitative features of the response. This might bear a direct relation to the morphology of the UBC synapse, which has large stretches of continuous PSD where glutamate might be trapped, but also areas of fractured PSD (causing the brush-like appearance) from where glutamate might escape rapidly from the cleft.

For such a large synapse, the amplitude of the fast EPSC in UBCs is surprisingly small; comparable to the EPSC in granule cells. In the model, the small amplitude of fast EPSCs resulted from the particular distributions of release sites and AMPA receptors. As these were randomly distributed, many AMPARs were not directly opposed to a release site, and therefore experienced much lower glutamate pulses. This effect could conceivably be even more enhanced by specificly designing AMPARs to be located away from release sites. However, as no information is available about the distribution of AMPARs in the cleft of UBCs this was not further investigated here. The simulated responses were not sensitive to the density of AMPARs in the model, except for an increasing variability in the relative amplitude of the fast EPSCs for decreasing AMPAR density. The reason for having many AMPARs in the glutamate-entrapment hypothesis is that the steady-state current of AMPARs is very small, so many AMPARs would be needed in order to produce the relatively large slow EPSCs that are observed in UBCs. This would not show up in the model, since it only examines AMPAR open probabilities.

Although simply assuming diffusion slowing in the model allows reproducing UBC EPSCs, a weakness to this hypothesis is that there is no explanation for how diffusion is slowed to such an extent. Explanations might be the presence of physical obstructions in the extracellular matrix within the cleft space, or the partial sealing of the cleft by glia in the glomerular structure. Alternative explanations to consider are for example that high glutamate levels are somehow maintained by delayed glutamate release. However, miniature events are not observed during the slow EPSC phase. AMPA receptors, perhaps on other local neurons, could trigger the activation of a slowly activating process causing a tonic inward current in UBCs, which might explain the slow tail. However, increasing the frequency of stimulation should lead in such a case to increasing EPSC amplitudes.

Due to the many release sites in the model, the global [glut] displayed very little variation between stimuli, as the stochastic behavior of individual sites was averaged out. This resulted in high reliability of the timing of the peak of slow resurgent EPSC tail (Figure 3.4B). This might provide UBCs with a robust mechanism for introducing slow, well-timed and reliable activation of granule cells involved in the control of slow eye and head movements.

3.4 Materials and methods

3.4.1 Model

Small synapses are often modeled as one-dimensional elements, in which transmission is described by a single time-dependent scalar. In order to understand how EPSCs arise at the UBC synapse however, it is necessary to consider spatial integration across the large area of PSD. This concerns for example taking into account the spatial distributions of release sites and postsynaptic receptors. The total area of UBC PSD can be up to 40 μm^2 in rats [31], while a typical value for the width of the synaptic cleft is 20 nm [79]. Given this relatively flat dimensionality the synaptic cleft was modeled as a two-dimensional space for simplicity. The space was discretized into 200x200 nm cells, which each could contain a release site and/or an AMPAR model, and thus represented the smallest 'functional' unit in the model.

3.4.1.1 Glutamate diffusion

The glutamate diffusion model was defined on the two-dimensional mesh for numerical simulation. Development of the glutamate concentration ([glut]) in each cell was calculated from the diffusional flux across cell faces in each time step. Dirichlet (fixed-value) conditions were imposed on the model boundaries, where

[glut] was equal to the ambient [glut] of 10^{-5} mM. Although glutamate transporters have been shown to shape AMPAR-mediated UBC EPSCs [37], their action was not explicitly incorporated in the model, but only implicitly in that the ambient glutamate concentration depends on glutamate reuptake. Local glutamate release was simulated by instantaneously increasing [glut] in selected cells by 6 mM, which corresponds to release of ~2900 molecules in the volume of a single cell. The diffusion coefficient was set to $D_{glut} = 0.25$ μm^2/ms as in [54, 81], although even lower values (by a factor 10) have also been suggested [80]. The spread of glutamate was manipulated in several simulations by altering the value of the diffusion coefficient on selected boundaries. In this way, D_{glut} could be lowered locally in selected areas of the model to introduce spatially nonhomogeneous features such as diffusion coefficient gradients. In other simulations hard barriers were inserted by setting $D_{glut} = 0$, to implement maze-like quasi one-dimensional diffusion paths for slowing down glutamate. The maze patterns were generated from a recursive algorithm that precluded the occurence of fully enclosed areas.

3.4.1.2 AMPA receptor kinetics

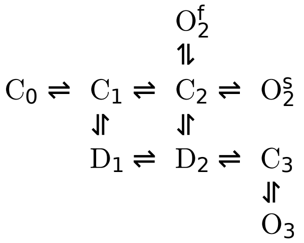

The kinetic AMPAR model was taken from Raman and Trussell [59] and used here to simulate the fraction of open channels in a collection of AMPARs. The transition rates were (in ms^{-1}): $C_0 \rightleftharpoons C_1$ $(30\ \text{mM}^{-1}, 0.3)$, $C_1 \rightleftharpoons C_2$ $(20\ \text{mM}^{-1}, 600)$, $D_1 \rightleftharpoons D_2$ $(20\ \text{mM}^{-1}, 1.038)$, $D_2 \rightleftharpoons C_3$ $(3.33\ \text{mM}^{-1}, 0.22)$, $C_2 \rightleftharpoons O_2^s$ $(3, 0.35)$, $C_2 \rightleftharpoons O_2^f$ $(60, 3)$, $C_1 \rightleftharpoons D_1$ $(1, 0.3)$, $C_2 \rightleftharpoons D_2$ $(27, 0.014)$, $C_2 \rightleftharpoons O_2^f$ $(60, 3)$, $C_3 \rightleftharpoons O_3$ $(0.006, 2)$. Rates are specified as (forward, backward). States O_2^s, O_s^f and O_3 were summed to determine the total fraction of open channels P_o. Transitions $C_0 \rightleftharpoons C_1$, $C_1 \rightleftharpoons C_2$, $D_1 \rightleftharpoons D_2$ and $D_2 \rightleftharpoons C_3$ were multiplied by the glutamate concentration. The bell-shaped dose-response curve of this model is due to the $D_2 \rightleftharpoons C_3$ transition, and is thought to underlie biphasic EPSCs. The $C_3 \rightleftharpoons O_3$ transition is responsible for the persistent open state of the channel at high glutamate concentrations. To simulate the effect of AMPAR desensitization block by cyclothiazide (Figure 3.4C) all transition rates to the D_2 state were set to zero. Simulations typically involved hundreds of independent (but identical) instances of the AMPAR model, and their open-probabilities were summed to obtain a measure of total AMPAR conductance P_O in the model.

3.4.2 Simulations

The partial differential equations (PDEs) defining the spatio-temporal glutamate concentration ([glut]) profile were implemented in FiPy, a finite-volume PDE solver [88]. The AMPAR model was implemented in NEURON [72], and simulation performed separately from (but simultaneously with) the diffusion model. Python [74] was used as an interface to drive AMPAR models using the local [glut] values on the grid [73]. Although coupling the two systems through Python comes at a computational cost (compared to solving a single large DE system), it brings considerable flexibility and ease of use to model design. Simulations were performed with a time step dt = 0.025 ms. For long traces an adaptive time step was sometimes used, where the next time step was calculated on the basis of the maximal absolute value of the (temporal) slope of the preceding glutamate profile. Simulations were performed on a laptop running Ubuntu 12.04, Python 2.7, FiPy 2.1.2 and NEURON 7.3. For systematic parameter variations simulations were distributed on a DELL HPC with 16 CPUs running Fedora 15, allowing 16 parameter sets to be evaluated simultaneously as independent threads.

3.5 Supplementary material

The accuracy of the numerical method using a dt = 0.025 ms time step was confirmed by comparison to analytical results in three simplified cases (Figure 3.5). For unbounded one-dimensional diffusion, the solution is the well-known pulse

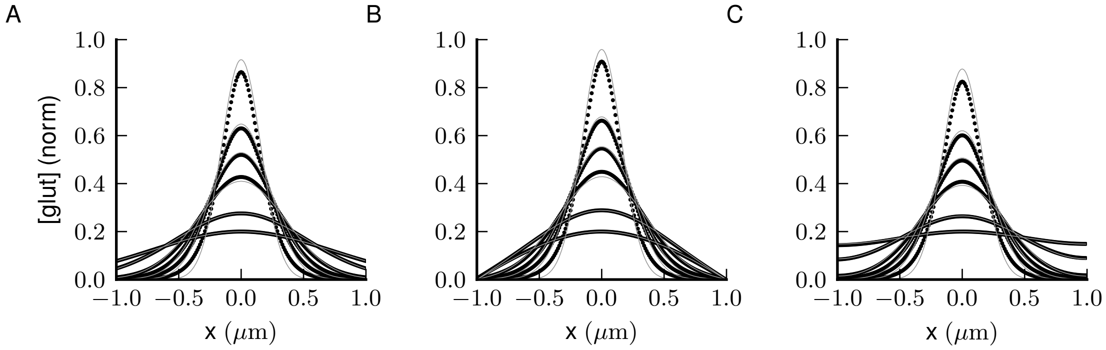

Figure 3.5: Validation of numerical diffusion simulation. Comparison of numerical (black dots) and analytical (grey traces) results on a 2 μm one-dimensional geometry. [glut] values are shown for times 0.05, 0.1, 0.15, 0.25, 0.55 and 1.05 ms relative to release in the center, for unbounded diffusion (A), Dirichlet boundary conditions (B) and Neumann boundary conditions (C). The spatial resolution for numerical simulation was 0.01 μm. Concentrations were normalized to the maximum of the last trace (at 1.05 ms).

response [89] given by

$$c(x,t) = \frac{N}{\sqrt{4\pi Dt}} e^{-x^2/(4Dt)}, \tag{3.1}$$

where c is the concentration, N is the number of molecules released in a point at $x = 0$, and D is the diffusion coefficient. Numerical and analytical results for unbounded diffusion are shown in Figure 3.5A. A solution to the diffusion equation in bounded conditions can be found for example through the method of separation of variables [90].

For Dirichlet conditions with $c = 0$ at both boundaries the general solution is given by

$$c(x,t) = \sum_{n=1}^{\infty} c_n \exp\left(-\frac{Dn^2\pi^2}{L^2}\right) \sin\left(\frac{n\pi}{L}x\right), \tag{3.2}$$

where L is the length. The coefficients c_n are given by

$$c_n = \frac{2N}{L} \sin\left(\frac{n\pi}{L}x_s\right), \tag{3.3}$$

where $0 < x_s < L$ is the location of the point source. Results for this case are shown in Figure 3.5B, for $L = 2$ µm and $x_s = 0$. For Neumann conditions with $\frac{dc}{dt} = 0$ at both boundaries the general solution is given by

$$c(x,t) = \frac{c_0}{2} + \sum_{n=1}^{\infty} c_n \exp\left(-\frac{Dn^2\pi^2}{L^2}\right) \cos\left(\frac{n\pi}{L}x\right). \tag{3.4}$$

The coefficients c_n are given by

$$c_n = \frac{2N}{L} \cos\left(\frac{n\pi}{L}x_s\right). \tag{3.5}$$

Results for this case are shown in Figure 3.5C. Solutions were obtained with Python using 50 iterations of Equations 3.2 and 3.4.

Chapter 4

Intrinsic excitability of unipolar brush cells

Vestibular neurons are known to exhibit high background firing rates and broadly linear information processing. These properties support the precise and reliable operation of vestibulo-ocular and optokinetic reflexes. Although at least a subset of UBCs are known to exhibit spontaneous regular background activity *in vivo*, little is known about their processing of time-varying inputs. In this chapter the subthreshold and suprathreshold response properties of UBCs are investigated in mouse cerebellar slices, by applying various types of time-varying current injections. UBCs displayed profoundly nonlinear subthreshold behavior, due to a low-threshold burst activation mechanism. In contrast, suprathreshold signal processing was linear in a broad range of firing frequencies, and response gain was boosted by a factor ~ 2 in a physiologically relevant range of sinusoidal modulation frequencies. These properties could allow for a linear representation of synaptic transformations in regularly firing UBCs, to communicate filtered versions of external mossy fiber activity to the vestibular cerebellum.

4.1 Introduction

4.1.1 Activity of vestibular neurons

Neurons use diverse strategies for representing information, ranging from rate codes where spike timing appears unimportant, to temporal codes that highlight specific elements in the structure of a stimulus [91]. In the vestibular system, afferents at the sensory periphery display a wide range of variability in background activity, and are classically divided into 'regular' and 'irregular' afferents [92, 93]. Irregular afferents have been shown to have higher velocity detection thresholds and reduced sensitivity to spike timing jitter, consistent with a temporal coding stategy [94]. However, many neurons in the vestibular system, both peripherally and centrally, are characterized by relatively high background firing rates of tens of Hz at a regular pace. This is the case for neurons in the vestibular nuclei and nucleus prepositus hypoglossi [95, 96], as well as eye movement-controlling motor neurons [97, 98]. High background firing rates of afferents and central neurons allow neurons in the cerebellar and vestibular nuclei to linearly represent vestibular information [99, 100]. Vestibular responses of these neurons *in vivo* are often described on the basis of linear-systems analysis methods [97, 98, 101, 102].

In the vestibulo-cerebellum, neurons apparently employ a variety of different coding strategies [103]. Granule cells are silent at rest *in vitro* [104] and display short intermittent bursts of spikes at high instantaneous frequencies *in vivo* [21, 44]. Golgi cells display slow (4-10 Hz) rhythmic activity *in vitro* [105], and slow irregular spontaneous activity *in vivo* [21, 44]. Molecular layer inhibitory interneurons fire irregularly at variable rates *in vivo* [21, 44] as well as *in vitro*, in part due to inhibitory inputs [84]. Purkinje cells, the output neurons of the cerebellar cortex, typically fire spikes (simple spikes) at a regular pace (tens of Hz) at rest, both *in vitro* [106] as well as *in vivo* [107, 108]. Regular firing in Purkinje cells is occasionally interrupted by powerful dendritic depolarizations (calcium spikes) due to current injection in slices or climbing fiber activation *in vivo* (complex spikes). How Purkinje cell simple and complex spikes are integrated with ongoing activity in their target brainstem nuclei is a topic of debate [109–111], but Purkinje cell input has been shown to modulate the phase of responses to sinusoidal vestibular stimulation in vestibular nucleus neurons, compared to non-Purkinje cell receiving neurons [102].

The spontaneous activity of UBCs has been characterized as very regular with a typical average rate of ∼20 Hz by extracellular recordings *in vivo* [21, 44]. *In* *vitro*, varying spontaneous activity patterns have been observed in UBCs, from completely silent [45, 47] to highly regular spiking [46]. In whole-cell recordings in slices, UBCs are able to fire rhythmically when depolarized by direct somatic current injection, and whether or not a UBC is intrinsically rhythmically active depends on the level of tonic hyperpolarizing baseline current at rest [33]. A salient feature of UBC physiology is the generation of slow all-or-none calcium spikes, initiated by activation of fast-inactivating, low-threshold T-type calcium currents I_{CaT} [45]. CaT channels are preferentially located in the dendritic brush, and can be activated by somatic current step injections from hyperpolarized membrane potentials in whole-cell recordings. Another prominent subthreshold feature in UBCs is the activation of an h-current ($\mathrm{I_h}$) in response to strongly hyperpolarizing current steps [46, 47]. $\mathrm{I_h}$ has been implicated in burst responses in UBCs [47], and is involved in generating rebound depolarizations upon release from hyperpolarization in other neurons [95, 112]. $\mathrm{I_h}$ is expressed to varying degrees in UBCs in relation to two main genetic classifications, with a lower density in mGluR1a$^+$ UBCs [48].

4.1.2 Neuronal dynamics

Neuronal membrane excitation is a nonlinear phenomenon caused by accelerated activation of voltage-gated ion channels, leading to the generation of action potentials. Similarly, neuronal membrane excitability, or the ability of a neuron to be excited, is regulated by various (subthreshold) ion channels that together dynamically determine neuronal input resistance. The specific details of the functioning of these ion channels and their impact on the membrane potential are determined by their spatial distribution in the cellular membrane and their specific biophysical properties, such as the dynamics of channel opening and closing regulated by voltage and/or ligands and modulators. Together, the ensemble of ion channels endows a neuron with certain computational properties, which are ultimately the determinants of its biological function in a network of interconnected neurons [113]. At this level, it is useful to classify neurons on the basis of their computational properties, instead of the specific distributions and biophysical properties of their ion channels. An important computational distinction of neuronal excitability exists between neurons that exhibit subthreshold oscillations of the membrane potential, and neurons that do not. The former act as 'resonators', exhibiting a preference for a certain band of input frequencies, while the latter act as 'integrators', preferring high input frequencies [114]. The classification 'resonator' is thus

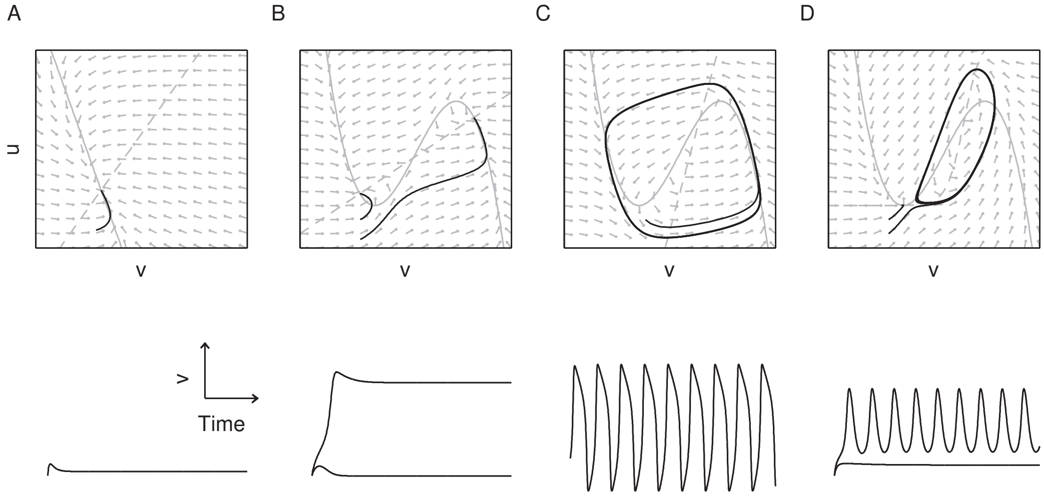

Figure 4.1: Examples of excitability modes. (A) Resting. All trajectories converge onto a single stable resting point determined by intersection of the linear u- and v-nullclines. (B) Bistability. The system can converge onto two separated resting values, depending on the initial starting values. (C) Spiking. The system converges to a periodic trajectory, resulting in sustained oscillation. (D) Resting-spiking bistability. The system can converge onto a stable resting value, or a stable periodic trajectory, depending on the initial starting values.

assigned on the basis of the presence of subthreshold oscillations, irrespective of the particular sets of ion channels that underlie them.

Neurocomputational properties thus essentially result from qualitative features of the (nonlinear) dynamics of the membrane potential, and many aspects of neuronal excitability can be qualitatively understood on the basis of reduced dynamical systems with only two or three variables [114, 115]. These models take the form of differential equations (DE's), for example (second-order leaky) integrator behavior can be described using a set of first-order DE's as

$$\begin{aligned} \dot{u} &= (s_u v - u) f_u \\ \dot{v} &= (s_v v - u) f_v. \end{aligned} \tag{4.1}$$

Here, u and v are dynamic variables, with v representing the membrane potential, and f and s are model parameters. The 'dot' notation was used to indicate time derivatives. The qualitative nature of the dynamical system makes it particularly suited to geometrical representation. Figure 4.1A shows a representation of Equation (4.1), where (normalized) values of $(\dot{u}, \dot{v})$ are plotted as grey vectors for several values of (u, v). This representation is called the 'phase plane' of the DE system. Special cases $\dot{u} = 0$ and $\dot{v} = 0$ are termed 'nullclines' and are shown as dashed and solid grey lines, respectively. The local values of $(\dot{u}, \dot{v})$ fully determine the course of development of u and v in time starting from initial values u_0 and v_0. An example of the time evolution of v is shown in the bottom trace, and corresponds to the black trajectory in the phase plane. In this case, all trajectories will converge onto a single coordinate in the phase plane, determined by the intersection of the nullclines. In general, the intersections of nullclines are important determinants of the qualitative structure (topology) of the system.

Replacing the linear v-nullcline with a third-order polynomial results in the Fitzhugh-Nagumo model (FN-model), a canonical model for neuronal excitability [116]. Depending on the parameters, this model can exhibit several different types of dynamics, two of which are shown in Figures 4.1B and 4.1C. In a bistable system such as displayed in Figure 4.1B, the membrane potential can settle into two stable resting states, depending on initial conditions. As the terminology suggests, these states are intrinsically stable, and switching from one state to the other can only occur due to an external perturbation such as a brief shock that offsets u and/or v. The presence or absence of bistability is another qualitative classification criterium (like the integrator versus resonator distinction) to distinguish neurocomputational properties [114]. A 'spiking' configuration of the FN-model is shown in Figure 4.1C, which has a single, stable oscillatory trajectory. By replacing the linear u-nullcline with a sigmoidal curve, a system can be designed that is again bistable, only in this case exhibiting a stable resting state and a stable spiking state (Figure 4.1D).

In general, the computational properties of a neuron are not fixed but are themselves dependent on the state of the membrane potential. This can change in response to current flow across the membrane for example due to synaptic input or, in a whole-cell patch-clamp configuration, due to (somatic) current injected through the pipette. Under certain conditions, external inputs can cause a fundamental change in the qualitative properties of the membrane potential dynamics, for example by causing a transition from a resting state to a (not previously existing) active (spiking) state. Such a qualitative transition in the dynamical system is called 'bifurcation', and can be understood as relative changes in the locations and shapes of nullclines and their intersections [117].

In this chapter the intrinsic transformations performed by UBCs when generating spike responses to time-varying current inputs are investigated. The focus is on two salient features of UBC excitability: the slow subthreshold CaT-spikes (slow subsystem) and the fast suprathreshold action potentials (fast subsystem). These two systems are coupled through the membrane potential in the intermediate domain. In the first part, the excitability of the slow subsystem is described in terms of a reduced nonlinear model. In the second part, the question is addressed how time-varying input currents are converted into action potentials in the intermediate (threshold-crossing) and suprathreshold regimes.

4.2 Results

4.2.1 Characteristic UBC physiology

Whole-cell patch-clamp recordings were obtained from UBCs in lobule X and the ventral part of lobule IX in cerebellar slices of 4 to 6 weeks old mice. UBCs were identified visually by the size of the soma, and in several cases a fluorescent dye was added to the pipette medium, unveiling the characteristic UBC morphology (Figure 4.2A). Breaking into the whole-cell configuration was always done in voltage-clamp mode, to obtain further confirmation of the UBC identity from the typical large membrane capacitance ($>$ 10pF). The signal amplifier was then switched to current-clamp mode. All experiments were performed in the presence of 100 μM picrotoxin and 1 μM strychnine to block GABAergic and glycinergic inhibition. Kynurenic acid (1 mM) or a mixture of D-APV (0.1 mM) and CNQX (0.02 mM) were present in the bath, except for cells that were also used in mossy fiber stimulation experiments. Blockers for excitatory synaptic transmission were always present during experiments that are particularly sensitive to noise, such as the slow threshold crossing current ramp injections. To evoke EPSPs a glass stimulation pipette was placed in the white matter or granule cell layer to electrically stimulate the presynaptic mossy fiber.

An example of a UBC response to mossy fiber stimulation is shown in Figure 4.2B. The conditions for this experiment were tuned to illustrate the all-or-none nature of the subthreshold burst mechanism, by injecting a hyperpolarizing current into the soma while stimulating the presynaptic mossy fiber. The EPSP was just below the activation threshold for nine out of ten trials (average trace in grey), and by a chance fluctuation in one trial activated the slow burst system (black trace). As was discussed in previous chapters, the EPSP had a slow tail that decayed to baseline in hundreds of milliseconds. The burst subsystem activated with considerable delay, as the stimulus was just on the threshold edge. Some characteristic responses of UBCs to subthreshold current injections are shown in Figures 4.2C and 4.2D. Increasing steps of depolarizing current elicited a burst of spikes in an all-or-none fashion. For sufficiently strong depolarizations the burst was followed by sustained spiking. Increasingly hyperpolarizing current steps

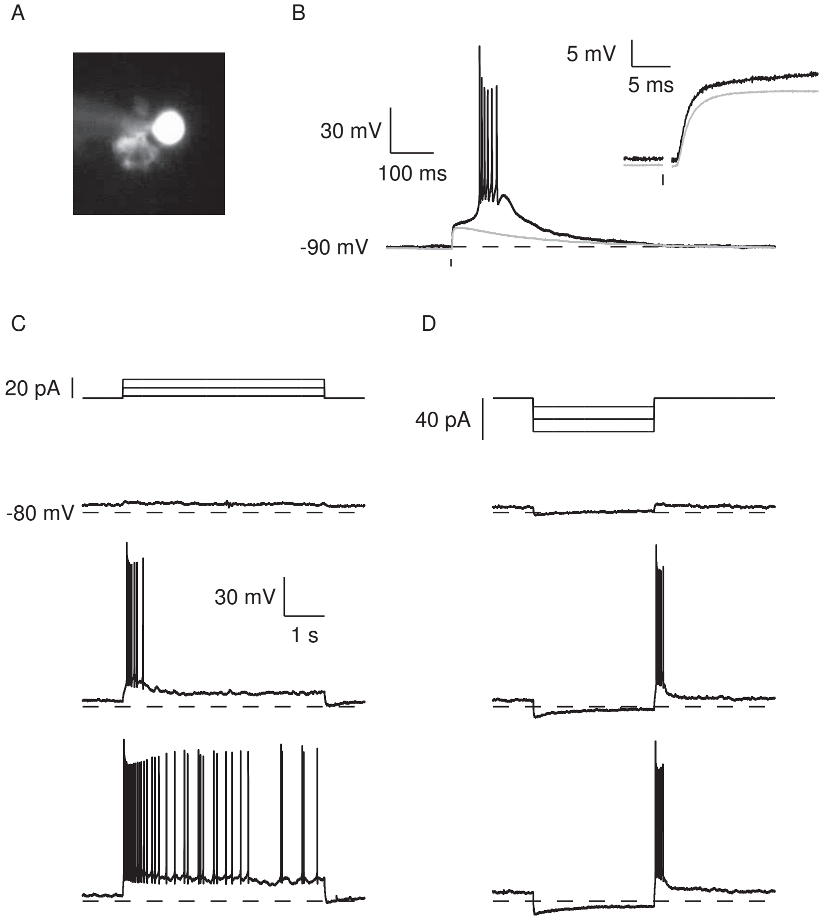

Figure 4.2: Subthreshold current steps. (A) Image of a UBC filled through the patch pipette with a fluorescent dye. The characteristic dendritic brush is visible to the left of the soma. (B) UBC response to a single stimulus to the presynaptic mossy fiber. Nine out of ten traces were just subthreshold (average in grey), one trace by chance just activated the burst system (black). (C) Characteristic UBC response to depolarizing current steps. A low-amplitude step gave a near-Ohmic response (top), while a higher amplitude step activated the burst system (middle). Even higher amplitude steps resulted in sustained spiking (bottom). (D) Hyperpolarizing current steps increasingly activated I_h, as evident from the voltage sag in the response. The burst system could be triggered upon release from hyperpolarization. Same cell as in C.

increasingly activated I_h, as is evident from the development of a voltage sag following the onset of the step. Furthermore, an all-or-none rebound depolarization was generated upon return from hyperpolarization, for sufficiently deep current steps.

4.2.2 Subthreshold mechanisms

To perform isolated investigation of subthreshold dynamics, the fast subsystem was blocked by bath application of 1 μM tetrodotoxin (TTX), which blocks fast Na^+-channels underlying action potential generation. As is clear from Figure

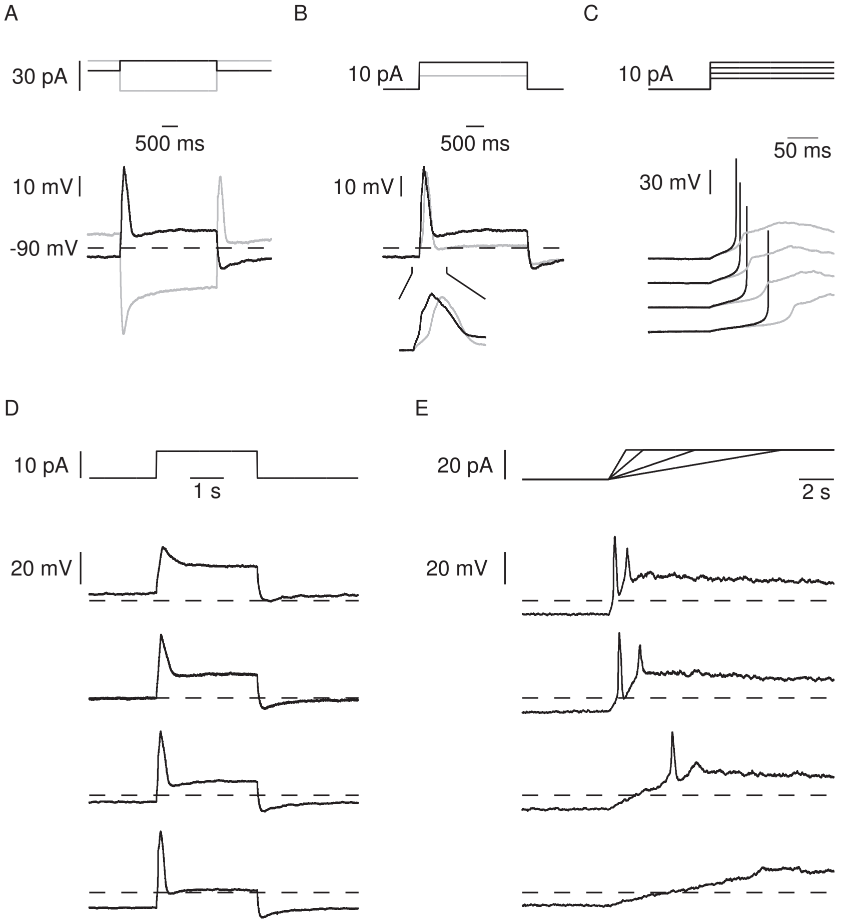

Figure 4.3: Excitability of the slow subsystem. (A) Depolarizing and hyperpolarizing current steps from a hyperpolarized membrane potential in the presence of TTX unveil the slow excitable subsystem underlying the UBC burst response. (B) Activation of the slow spike accelerated with increasing current step amplitude. The amplitude of the slow spike was relatively insensitive to the current step amplitude. (C) Overlay of slow subsystem activation in the same UBC before (black) and after (grey) TTX application. The burst response accelerated with increasing current step amplitude. Current steps were performed from the same membrane potential, but traces were offset for clarity. (D) The slow subsystem only activated from hyperpolarized membrane potentials. (E) Activation of the slow subsystem by current ramps with increasing slopes, for the same cell as in D. Slow depolarization could not trigger slow spikes, while faster depolarization could trigger repetitive slow spikes.

4.3A, the CaT- and I_h-subsystems causing the slow depolarizing spike and voltage sag could operate in the absence of the fast Na^+-subsystem. A 10 pA depolarizing current step from hyperpolarized membrane potential triggered a spike with $\sim$50 mV amplitude and $\sim$300 ms half-width. A prominent voltage sag was present in response to a 30 pA hyperpolarizing current step, indicating I_h activation, and a rebound spike was present upon release from inhibition. The slow spike was triggered in an all-or-none fashion by current step injection, and the amplitude of the spike was insensitive to the amplitude of the current step, as shown in Figure 4.3B. The amplitude of the current step did affect the timing of the peak of the

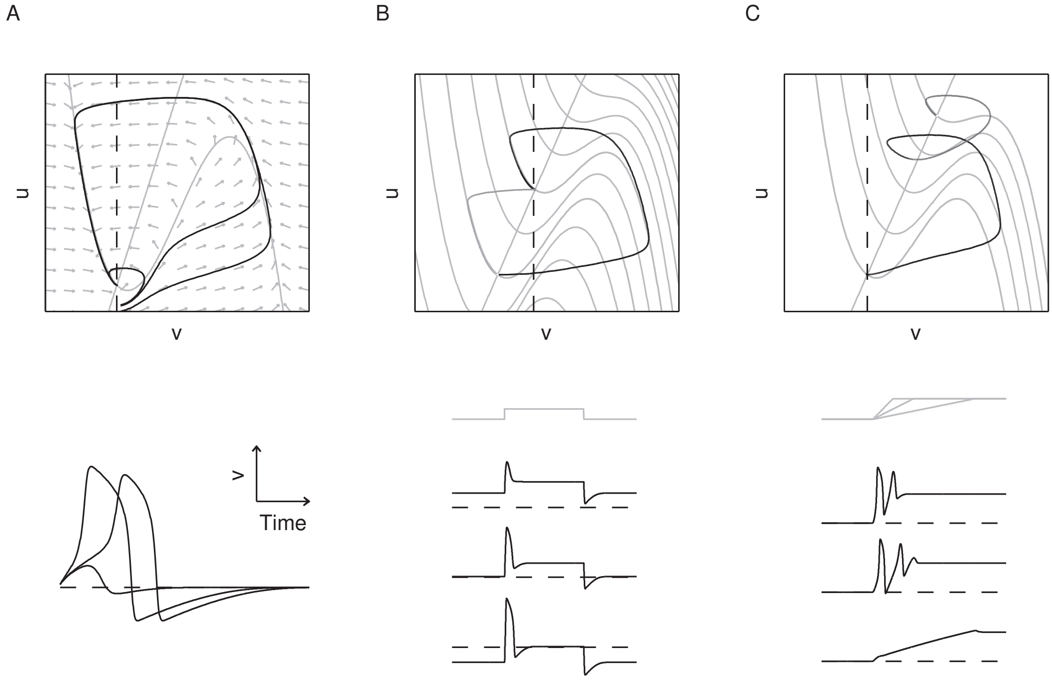

Figure 4.4: Dynamics of subthreshold excitability. (A) Spike generation in the FN-model. Although there is a single stable resting state in the system, some trajectories first traverse a spiking orbit before settling down on the resting state. The velocity and phase of the trajectory depend on the initial condition, and can be different even when starting from the same membrane potential v. (B) Current-step protocol in the FN-model. The injected current I is a model parameter, and affects the shape and location of the v-nullcline, thereby generating a single spike. (C) Current-ramp protocol. Slow linear change of I elicits different effects depending on the slope of the ramp.

slow spike, as its activation was accelerated for larger input current. This effect is layed out in more detail in Figure 4.3C, which shows an overlay of responses to four incremental steps, before (black) and after TTX application (grey). The activation of the slow spike gradually accelerated with increasing current steps, and the first Na^+-spike of the burst followed accordingly. The amplitude of steps of input current thus appeared to be particularly relevant to the timing of the burst response, as the timing of the first spike was dictated by the dynamics of the slow subthreshold mechanism. Slow spikes could only be triggered from hyperpolarized membrane potentials, in a sharply defined window. This can be seen in Figure 4.3D, where a baseline V_m shift of $\sim$10 mV almost abolished the slow spike.

UBCs thus generated a single slow spike in response to depolarizing current steps, before settling down to a stable resting V_m on the current plateau. To investigate whether the response was due to initial dynamical properties of the cell (that is, prior to the onset of the current step), or whether the system underwent a bifurcation during the step, the onset of the current step was replaced by a slow linear depolarizing current ramp. The ramp could result in multiple slow spikes for steep slopes, or no spikes at all for shallow slopes, as shown in Figure 4.3E. Membrane depolarization by itself was thus not sufficient for activating the slow spike, which required a minimal rate of depolarization. V_m developed smoothly during a slow ramp without generating a spike, even when the final plateau amplitude of the injected current was higher than the amplitude which was used for the current steps. This indicated that the used level of current injection in fact did not cause a bifurcation in the system, and that the generation of the slow spikes was caused by a different mechanism.

The behavior of the cell can be qualitatively understood by considering the FN-model in Figure 4.4. The model had a single stable resting state, but when simulations were initiated with different initial condictions (u_0, v_0), some trajectories first traversed a spiking orbit before settling down on the resting state. The velocity and phase of the trajectory depended on the initial conditions, and could be different even when starting from the same v, as shown in Figure 4.4A. This behavior is analogous to the differences in timing of onsets of the slow UBC spike in Figures 4.3B and 4.3C. The parameters of the v-nullcline were I-dependent (see 'Materials and Methods' Section 4.4), as can be seen graphically from the stacked example nullclines in Figure 4.4B. In response to an instantaneous step in I (grey time-dependent trace), the v-nullcline was changed. The plotted trajectory corresponds to the bottom time-dependent trace of v. Even though the v-nullcline changed in response to I, no bifurcation occurred and the topology of the system remained the same. Instead, the generation of the spike was due to an 'accomodation' effect. Qualitatively, the sudden change in structure of the model allowed the system to transiently escape the attraction of the stable resting state, and produce a single spike before converging on the new resting state. The excitability of the system depended on the state of v, due to an I-dependent change in shape of the v-nullcline. By 'dragging' the v-nullcline using a linear current ramp, the system could continue spiking due to this mechanism, until the ramp ended or the system lost excitability due to a change in the shape of the v-nullcline (Figure 4.4C). The trajectory in the phase plane corresponds to the top time-dependent trace of v. If the current ramp slope was too shallow, the system could no longer escape the attraction of the stable resting state, and was thereby unable to generate spikes. The mechanism of accomodation could thus well describe the activation of slow UBC subthreshold spikes.

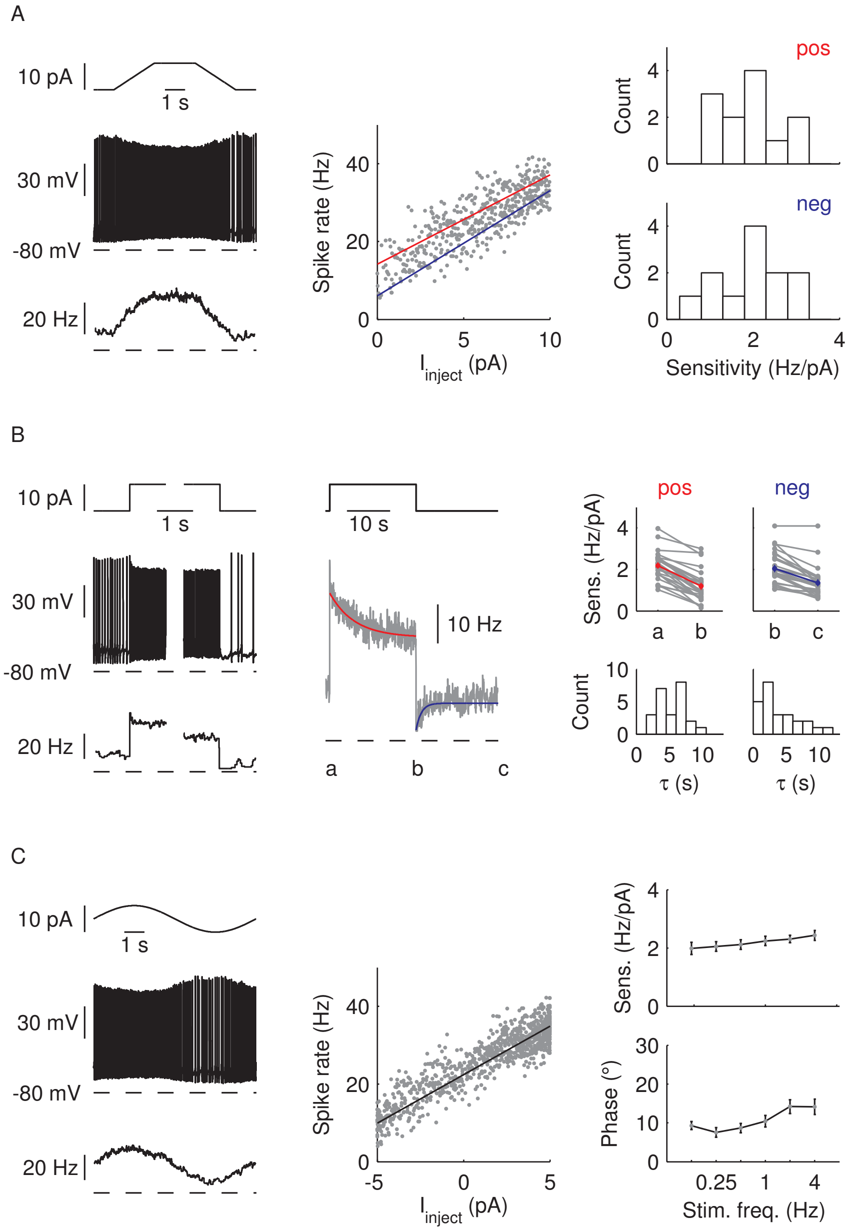

Figure 4.5: Suprathreshold response gain. (A) Suprathreshold gain of ramp step current injection. Left, from top to bottom: ramp step current, example spike response, and average (10 trials) spike rate response. Middle: Response gain analysis. Positive and negative parts usually had slighty different gain and offset, as is also evident from the slight spike rate undershoot after the negative ramp injection (left bottom panel). Right: Summary of current response gains of 12 UBCs. (B) Step current injections. Left: as in Panel A. Middle: Example of average spike in response to a long-lasting current step. A gradual decrease in response gain was evident in most cells, with a time constant of ~ 5 s. Right: Summary of response sensitivity (gain) at the beginning and ending of positive and negative steps (n=24). Response gain decreased almost 50% during positive steps, with time constants (τ) of several seconds. (C) Sinusoidal current injections. Left: as in Panels A and B. Middle: analysis of response gain. Right: Response gain and phase as a function of sine frequency (average of 22 cells). Both gain and phase were essentially flat, with a slight tendency to increase with increasing frequency. The average response gain was similar to that of the ramp step response in Panel A, and to the initial (high) step response gain in Panel B.

4.2.3 Suprathreshold responses

UBCs generate regular fast APs from a depolarized state in the current-clamp configuration. Such a mode of continuous AP generation lends itself to analysis using linear systems methods, where the I input is related directly to the AP rate. To investigate the dynamical properties of this input-output relation, UBCs were depolarized to fire APs at approximately 20 Hz. Three patterns of time-varying current injections were used: ramp steps, instantaneous steps, and sine waves (Figure 4.5). UBCs responded linearly to current ramps in a broad range of AP rates, with usually slightly overdamped and underdamped responses to positive and negative slopes, respectively (Figure 4.5A). The linearity of the response allowed to define a response gain, which was ∼2 Hz/pA in both directions (n=12). To further assess the linearity of the system, instantaneous I steps were used to long-lasting plateaus (Figure 4.5B). Although the initial gain of instantaneous step responses was similar to that of ramp responses, slow firing rate adaptation occurred on the I plateau with time constants ∼5 s and ∼2 s for positive and negative steps, respectively (n=24). The steady-state gain values were ∼1 Hz/pA for positive and negative steps. Sinusoidal modulations had similar high response gain ∼2 Hz/pA, and exhibited a ∼10° phase lead (Figure 4.5C). Gain and phase were virtually independent of the modulation frequency in the range 0. 125-4 Hz, although a weak positive trend was visible in both gain and phase data (n=22).

UBCs thus exhibited linear suprathreshold response gain, which could only be sustained for relatively rapidly varying I injections. To further probe UBC excitability across the entire physiological range of membrane potentials, a slow current ramp was used to gradually depolarize UBCs from a hyperpolarized state, until the onset of fast AP excitation block. An example of such an experiment is shown in Figure 4.6A. Threshold crossing was occasionally accompanied by a burst of spikes, as a result of activating the slow subthreshold subsystem, as shown in the inset. UBC response gain during slow depolarizing ramps generally exhibited three phases, as shown in Figure 4.6B. First, the transition from the subthreshold domain to the suprathreshold domain was marked by a brief, highly nonlinear bursting phase. This was followed by a period of linear gain, which covered responses ranging tens of Hz. The response gain during this period was ∼1 Hz/pA, which was similar to the steady-state step-response gain of Figure 4.5B. Finally, a discrete transition usually occurred to a period of very low response gain, although this was not always clearly so in all cells. Spike rates in this period were near the maximum attainable spike rate of the cell. Further current injection would gradually drive the cell into depolarization block, with spike amplitudes gradually decreasing until fully diminished (not shown in the figure). Subsequent slow hyperpolarization with a negative ramp usually occurred approximately linearly, with a gain that was comparable to, or slightly lower than the initial linear gain during the upwards slope. The transition from suprathreshold to subthreshold was usually accompanied by a brief, nonlinear decrease in firing rate. The gains of the linear phases during the slow ramps are summarized in Figure 4.6C, according to the indices in Figure 4.6B. The overall nonlinearity in the firing rate responses resulted in strong hysteresis during the cycle of positive and negative slow current ramps. Hysteresis was quantified by calculating the normalized surface area enclosed by the input-output curves, as shown in Figure 4.6D. Firing rate hysteresis occurred in all cells tested (n=18).

4.3 Discussion

The goal of this chapter was to describe the intrinsic transformations performed by UBCs when generating spike responses to time-varying current inputs. UBCs exhibited highly nonlinear response gain to current injections from hyperpolarized membrane potentials, due to generation of slow depolarizing spikes that triggered strong bursts of fast action potentials. In contrast, suprathreshold $R - I$ curves were linear in a broad range of firing rates. This bimodal behavior was examined using various time-varying current injection protocols, and the dynamical response properties were investigated using minimal models of neuronal excitability.

4.3.1 Modeling the slow subsystem

The mechanism of generation of the slow spike was investigated using a canonical nonlinear model. The motivation for using such a simplified model comes from the recognition that certain aspects of the dynamics of neuronal excitability have qualitative properties that are largely independent of specific biological details. This is apparent, for example, from the observation that different neurons can share certain qualitative computational properties, such as subthreshold membrane potential oscillations, while using different underlying biophysical mechanisms to produce them. The biophysical details of these mechanisms can often be reduced to canonical forms without loss of generality. For example, a canonical action potential might have a slightly different shape than an actual measured action potential, but any desired level of additional detail can be added to the model

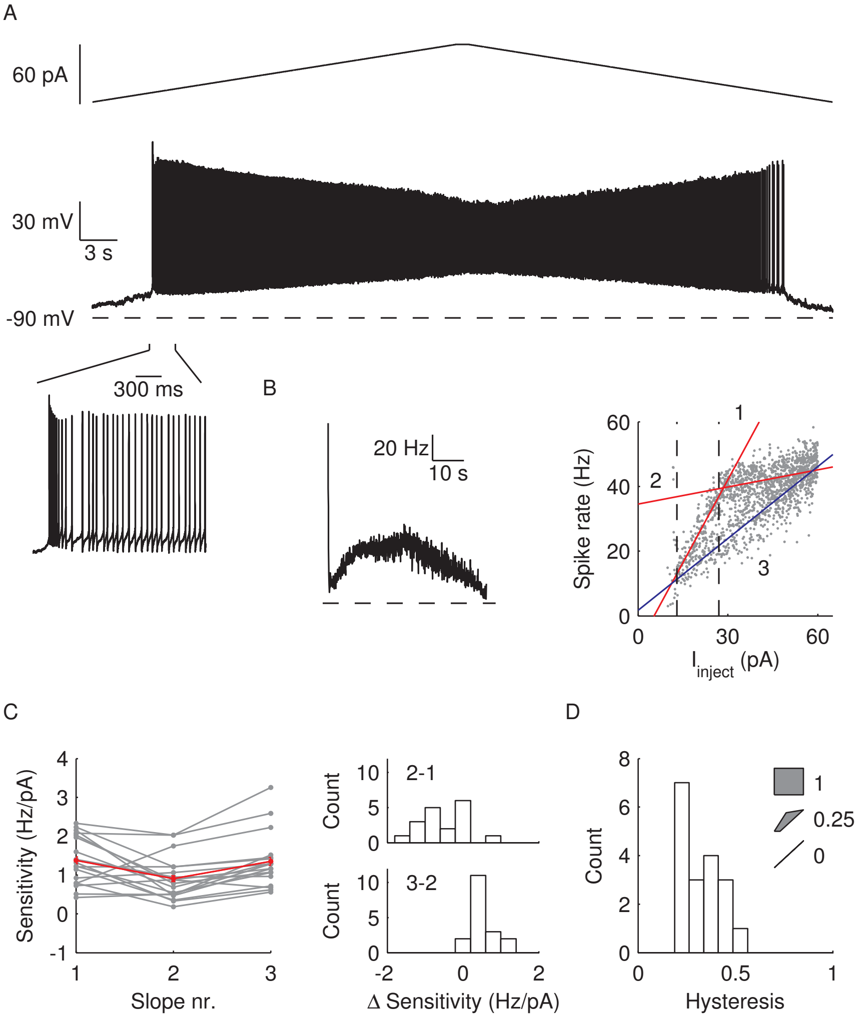

Figure 4.6: Gradual threshold crossing with a current ramp. (A) UBC response to slow current ramp injection. Crossing from subthreshold to suprathreshold V_m was initiated by a burst response. Spike rate then gradually increased, and spike amplitude decreased, with increasing current amplitude. (B) Left: Instantaneous spike rate as a function of time during the slow current ramp. The threshold crossing introduced a strong nonlinearity in the spike rate response. Right: Instantaneous spike rate as a function of injected current. The nonlinearity due to threshold crossing is evident from the positive (increasing current) part of the ramp, which displayed a discrete change in gain from slope 1 to slope 2. (C) Left: Sensitivity (gain) of the response to current injection of 18 UBCs according to the slopes indicated in Panel B. Right: The transition from slope 1 to slope 2 was negative in all cells except one, while the transition from slope 2 to slope 3 was always positive. (D) Quantification of gain hysteresis, by determining the normalized surface area enclosed by lines 1, 2 and 3, within the bounds of the axes. The grey areas drawn in the upper right corner of the axes indicate examples of areas corresponding to hysteresis values of 0, 0.25 and 1. Threshold crossing caused substantial gain hysteresis in all cells tested.

to attain the biological shape, at the cost of additional complexity. Such reduced models thus offer phenomenological explanations of excitability, not mechanistic ones. Still, they provide information on the types of computations a neuron can perform, in a way that is eligible to intuitive geometric understanding of the underlying principles [114].

A minimal definition of a burst is the occurrence of two or more APs followed by a period of relative quiescence. In general, bursts occur due to interplay of fast currents underlying spiking activity and slow currents that modulate that activity. If the fast and slow currents have very different time scales they can be considered as independent subsystems, and analyzed by considering the slow subsystem as driving the fast subsystem through bifurcations of stable and spiking states. In UBCs, the time scales of slow and fast spiking were separated by two orders of magnitude. Also, slow spike repolarization did not require fast APs, as it functioned in the presence of AP blocker TTX. The two processes were therefore treated as independent subsystems. Low-threshold burst activation in UBCs was explained by an 'accomodation' effect in a two-variable nonlinear system, which allowed generation of a single slow spike in response to a sufficiently fast depolarizing current input. Although slow spike activation did not seem to involve a system bifurcation, signs of a nearby bifurcation point were sometimes observed in response to current steps, evidenced by a few damped oscillation cycles following the slow spike. UBC bursts thus acted as threshold elements for the rate of membrane depolarization, that is, they would be activated only in response to 'sudden' events. Bursts have been assigned many different functions in different types of neurons, including improving transmission reliability by increased signal-to-noise ratio, implementing selective communication to subsets of postsynaptic neurons, and encoding specific features of a sensory input [118].

4.3.2 Comparison to vestibular nucleus neurons

In UBCs, bursts could only be triggered from hyperpolarized membrane potentials, and it seems therefore that under physiological conditions a strong inhibitory synaptic input would be required to generate bursts by release from inhibition. Such a 'rebound' burst mechanism has also been identified in neurons of the cerebellar and vestibular nuclei [95, 112], and its physiological function has been a topic of debate [109, 111]. Vestibular nucleus neurons are spontaneously active with regular firing rates both *in vitro* and *in vivo*, which is also the case for at least a subset of UBCs [21, 43, 44, 46]. Intrinsic excitability of UBCs thus bares some resemblances to that of vestibular nucleus neurons. This is also the case at the level of neural connectivity, as a subset of UBCs in the nodulus receives mossy fiber input directly from first-order vestibular afferents [119]. These UBCs thus seem a kind of displaced precerebellar neurons. Medial vestibular nucleus neurons display linear behavior in response to time-varying somatic current injections [99], as well as excitatory synaptic inputs [100]. These properties are shared among diverse precerebellar neurons [96], although the extent of firing rate adaptation varies among different cell types within the vestibular nuclei [112]. Although it is shown in this chapter that UBCs also exhibited linear suprathreshold behavior, the synaptic transformations in UBCs were distinctly different from those in vestibular nucleus neurons (see Chapter 2).

A suprathreshold role for low-threshold CaT-currents has been shown in vestibular nucleus neurons, where voltage-gated Ca^{2+}-channels and Ca^{2+}-dependent K^{+}-channels regulate the gain of spike rate responses to somatic current injections [120]. Furthermore, propensity for post-inhibitory rebound firing was associated in the these neurons with firing rate adaptation in response to current steps [112]. All UBCs tested in the current study exhibited subthreshold burst responses, as well as slow but significant suprathreshold firing rate adaptation. Although the relation between burst strength and firing rate adaptation was not investigated here, it is known that a subtype of UBCs is less prone to burst firing [48]. And it would thus be interesting to investigate the relation between the two phenomena in line with results from vestibular nucleus neurons.

4.3.3 Relation to UBCs *in vivo*

In general, UBCs occur mostly in the vermal areas of the cerebellum, and in the (para-) floccular lobes. The abundance of UBCs in the vestibulo-cerebellum points to a specific role in the control of eye movements [42]. As vestibular mossy fibers typically display high tonic background activity, UBCs *in vivo* likely experience long periods of continuous depolarizing inputs. In slices, trains of stimuli to mossy fibers have been shown to result in depolarized current plateaus from which UBCs generate continuous trains of APs [45, 47, 121]. Accordingly *in vivo*, UBCs were found to display overall very regular spontaneous firing, and responded to vestibular stimulation by smoothly decreasing or increasing their ongoing spiking activity [21, 43, 44]. UBCs responded linearly to sinusoidal head movements in anesthetized mice, with a broad phase dispersion relative to the stimulus. As shown in this chapter, UBCs *in vitro* responded linearly to sinusoidal current injections with a 10° phase lead. The broad phase dispersion *in vivo* was thus likely due to variations in the phases of mossy fiber discharges, which are known to signal mixtures of head velocity- and head position-related patterns [20, 44, 122–125]. An interesting observation was made in another *in vivo* study in awake, behaving rabbits, where UBCs responded with a mixture of eye position- and eye velocity-related signals to sigmoidal head displacement [43]. Here, responses started only after considerable delays up to 200 ms. Such delayed responses are not observed in other neurons such as the surrounding granule cells, and are therefore most likely due to UBC intrinsic signal processing. As it was shown in this chapter that suprathreshold $R - I$ relations in UBCs *in vitro* were linear, these delays might have resulted from synaptic transformations as described in Chapter 2.

Suprathreshold signal processing in UBCs had several features in common with the processing performed by the neural circuitry that produces the VOR. The transformation from head movements to oculomotor commands is essentially linear over a wide range of head movement amplitudes [126]. The VOR system is precise and reliable, and operates in a frequency range that matches the range in which *in vitro* UBC responses were linear with virtually flat phase and gain (0. 125-4 Hz). UBCs displayed a slow ($\tau \approx 5$ s) firing rate adaptation process in response to current injection steps, which effectively provided a preferential boost in response gain by a factor ∼2 for relatively fast input modulation frequencies. The linearity of the spike generation mechanism would provide a linear representation of UBC synaptic transformations, which remain the most striking aspect of UBC physiological and morphological specialization. Delays and slow summation of mossy fiber inputs could be especially relevant to the process of neural integration which underlies the transformation from head velocity to head position signals in the VOR [127].

4.4 Materials and methods

4.4.1 Slice preparation

Parasagittal slices (250 µm) where prepared from the cerebellar vermis of 4 to 6 weeks old C57BL/6 mice. The animals where anesthetized by isoflurane inhalation, after which the cerebellum was quickly removed and mounted in a vibratome (Leica VT1000S, Leica Microsystems). Thin sections (250 µm) where cut using a ceramic blade (Campden Instruments) in ice-cold bicarbonate-buffered solution containing (in mM): 90 NaCl, 2.5 KCl, 1.25 NaH_2PO_4, 26 $NaHCO_3$, 0.5 $CaCl_2$, 4 $MgCl_2$, 25 D-glucose, 75 sucrose and 1 kynurenic acid (bubbled with 95% O_2, 5% CO_2). After cutting, slices were allowed to recover for 1 h in an artificial cerebrospinal fluid (ACSF) at 34 °C containing (in mM): 127 NaCl, 2.5 KCl, 1.25 NaH_2PO_4, 26 $NaHCO_3$, 1.5 $CaCl_2$, 1 $MgSO_4$ and 20 D-glucose (bubbled with 95% O_2, 5% CO_2). Slices where then stored in ACSF at room temperature for up to 6 hours.

4.4.2 Electrophysiology

For electrophysiological recordings slices were transferred to a perfusion chamber mounted in an upright microscope (modified Olympus BX51), equipped with infrared differential interference contrast (IR-DIC) optics and whole-field epifluorescence imaging (LaVision Biotec). Slices were continuously perfused with bubbled ACSF (2 ml/min) at room temperature (22-24 °C). In all experiments ACSF was supplemented with 100 μM picrotoxin and 1 μM strychnine, to block GABA-ergic and glycinergic inhibition. Cells in lobule IX or X were visualized with a 40X water immersed objective (Olympus LUMPLFLN) and a digital camera (AxioCam MRm with AxioScop software, Carl Zeiss). Patch pipettes were pulled from filamented borosilicate glass capillaries (Warner Instruments) with a horizontal puller (Sutter Instruments P-97), resulting in a typical resistance of 7-8 MΩ. Pipettes were filled with a potassium-based intracellular solution containing (in mM): 140 K-gluconate, 0.2 EGTA, 10 HEPES, 4 Na_2ATP, 0.4 Na_3GTP and 2 $MgCl_2$ (290 mOsm, pH 7.3 set with KOH). UBCs were visually identified by their typical soma size (slightly larger than granule cells), and morphology was confirmed in several experiments by supplementing the intracellular solution with a fluorescent dye (20 μM Alexa-Fluor 488, Invitrogen). As a reference electrode an Ag/AgCl wire was connected to the bath through an agarose salt bridge. Whole-cell patch-clamp recordings were performed using an Axon Multiclamp 700B amplifier (Molecular Devices), and data sampled through an Axon Digidata 1440 in combination with pClamp acquisition software (Molecular Devices), or through an onboard PCI card (NI PCI-6259, National Instruments) controlled by custom MATLAB routines (MathWorks). Signals were typically sampled at 50 kHz, and filtered at 10 kHz. The identity of UBCs could be confirmed by their whole-cell capacitance ($C_m = 15 \pm 1$ pF, n=32). Stocks of D-APV and CNQX (Tocris Bioscience) were prepared in water, and stocks of picrotoxin and strychnine (Sigma-Aldrich) were prepared in DMSO. These were stored in aliquots at -20 °C. Kynurenic acid (Sigma-Aldrich) was dissolved in equimolar NaOH and stored at 4 °C. The final concentration of DMSO in the extracellular solution did not exceed 0.1%.

4.4.3 Electrical stimulation

Current pulses were generated by an isolated pulse stimulator (A.M.P.I.) and delivered to the tissue through a double or single barrel borosilicate glass pipette. Pipettes were filled with HEPES-buffered ACSF, and placed to evoke a reliable synaptic response from the white matter or granular layer. Trigger pulses were generated from an onboard PCI card (NI PCI-6259, National Instruments) controlled by custom MATLAB routines.

4.4.4 Data analysis

Data analysis was performed in MATLAB (MathWorks). Instantaneous firing rates were calculated as the reciprocal of the interval between successive spikes, and were assigned to the time in the center between two spikes. Suprathreshold firing rate modulation was determined in response to input current ramps, steps and sine waves, and output curves were calculated by averaging 5-10 repetitions. For ramp and sine wave modulations the firing rate R versus input current I were fitted to a linear function $R = Ax+B$, by minimizing the mean squared difference. The slope A provided the gain value. Varying ramp slopes from 3. 33-5 pA/s gave identical results and gain values were therefore averaged. To determine firing rate gain and adaptation during long-lasting instantaneous steps, responses during the period of the step were fitted with a single exponential function $R = Ae^{-t/\tau} + B$, by minimizing the mean squared difference. Initial step response gain was calculated by determining an average baseline firing rate in a 1 s window prior to the onset of the step, and subtracting it from the value of A. Steady-state gain was obtained by subtracting the baseline from B, and the adaptation time constant was given by τ. A sinusoidal function $R = A\sin(2\pi ft + \phi)+B$ was fitted to the responses to sinusoidally oscillating current injections, by minimizing the mean squared difference. The frequency f was set to the modulation frequency, and gain A and baseline B were previously determined from a linear fit to the R versus I data. The phase ϕ of the response with respect to the input signal then followed from the sinusoidal fit; positive values indicate a phase lead. This method provided good fits, but can only be used when phase differences between input and output signals are small, as the $R - I$ curve would otherwise display hysteresis and would not be linear.

During slow UBC threshold crossing with a ramp, the firing rate response curve consisted of several phases, which were separated by eye. Threshold crossing was a nonlinear bursting phase, then followed by a linear part which often showed a distinct transition at a certain level of current injection I to a next linear phase with low gain that was near the maximal firing frequency of the cell. The subsequent negative I ramp was treated as a single linear phase, followed by a brief nonlinear phase when the cell transited to the subthreshold domain. There were thus altogether three linear suprathreshold response phases, and each was marked by two I levels in the R-I plot. If a clear transition from phase 1 to phase 2 was not present, the separation between the two was set to the value of I at the end of phase 3. To determine R-I gain during the different phases, the data were fitted with a linear function by minimizing the mean squared difference. Altogether, the slow ramp protocol defined a closed trajectory in the R-I plot. As a measure for the nonlinearity during the full trace, a measure for the hysteresis of the R-I curve was determined using the linear fits to the three suprathreshold response phases. This was done by calculating the surface area enclosed by the linear fits and, where necessary, the $R = 0$ or $I = 0$ axis. The enclosed surface area was then normalized to the product of the maximal applied current and maximal measured firing rate ($R_{max} \times I_{max}$), resulting in a hysteresis index between 0 (no hysteresis) and 1 (full hysteresis).

4.4.5 Simulations

To investigate the qualitative dynamics of UBC excitability, models were constructed with a minimal number of variables to explain nonlinear subthreshold behavior, as well as suprathreshold input-output responses. Slow subthreshold spike generation was simulated with a Fitzhugh-Nagumo model (FN-model), a two-variable dynamical system defined as

$$\begin{aligned} \dot{u} &= (A_1\left(v - u_c\right) - u)f_u \\ \dot{v} &= C_3\left(B_3 v - v_c\right)^3 + C_2\left(B_2 v - v_c\right)^2 + C_1\left(B_1 v - v_c\right) + C_0 - u)f_v. \end{aligned} \tag{4.2}$$

Here, u and v are dynamic variables, with v representing the membrane potential. The 'dot' notation was used to indicate time derivatives. This model has a linear u-nullcline and a cubic v-nullcline, and several parameters depended on the injected current I. Parameters f_u and f_v could be used to independently scale $\dot{u}$ and $\dot{v}$, and the nullclines were centered using $u_c = -108.2$, $v_c = -103$. u-nullcline parameters were $A_1 = 0.0286$ and $f_u = 0.0023$. v-nullcline parameters were $B_1 = 1 + 0.45I$, $B_2 = 1 + 0.45I$, $B_3 = 1 + 0.55I$, $C_0 = 0.05 + 1.8I$, $C_1 = 0.0005 - I/20$, $C_2 = 0.0015 - I/1800$, $C_3 = -0.0000375 + I/40000$ and $f_v = 2$. Solution trajectories were obtained by numerical simulation of the model in MATLAB, using a forward Euler scheme.

Chapter 5

Conclusion

Unipolar brush cells (UBCs) are a relatively newly defined cell class in the cerebellar cortex, and relatively little is known about their physiology and function in the cerebellar network. The peculiar specialization of the synapse, combined with the strategic position in the granular layer are likely to allow UBCs to importantly influence cerebellar cortical information processing. This thesis concerns experimental and theoretical investigations of synaptic excitation and intrinsic excitability of UBCs. The main results of the thesis are summarized in this chapter, and the relevance to the current state of understanding their functions is discussed.

5.1 Summary

The vestibulo-cerebellum is an area of the cerebellum that is involved in regulating eye movement reflexes. One such reflex is the vestibulo-ocular reflex (VOR), which aids to stabilize images on the retina by countermoving the eyes in response to head movement. It is initiated by activation of the vestibular organs, which signal information about angular and linear velocity of the head. The vestibulo-cerebellar cortex is characterized by the abundance of a relatively unexplored class of excitatory interneurons, called unipolar brush cells (UBCs). **Chapter 1** describes some of the more salient features of UBC synaptic transmission, intrinsic excitability and connectivity in the cerebellar network. UBCs are feedforward neurons that synapse onto cerebellar granule cells and sometimes also onto other UBCs. This feedforward connectivity was demonstrated in **Chapter 1** by electrically stimulating presynaptic mossy fibers in cerebellar slices, while recording synaptic activity in granule cells or UBCs. In some cases synaptic responses were delayed by tens of milliseconds; an observation that is best explained by assuming the presence of an intermediate UBC. Furthermore, the responses consisted of trains of several impulses, which is consistent with responses of UBCs to synaptic stimulation. Further evidence of forwarding by UBCs was obtained by making use of the fact that UBCs are occasionally spontaneously active in slices. Spontaneous synaptic inputs could occasionally be measured in granule cells and UBCs, that matched the spontaneous activity patterns of UBCs in slices.

The morphologically and functionally most distinctive feature of UBCs is the single dendrite, which has a paint brush-like tuft with many small protrusions termed dendrioles at the tip. It forms a giant synaptic contact with a single mossy fiber, which carries (extra-cerebellar) vestibular information into the vestibulo-cerebellar cortex. In **Chapter 2**, the consequences of this peculiar specialization for synaptic transmission are investigated. Excitatory postsynaptic currents (EPSCs) in UBCs had a biphasic shape, consisting of a fast 'classical' EPSC followed by a slow, transiently resurging tail current that lasted hundreds of milliseconds to seconds. Application of a long-lasting regular presynaptic stimulation protocol, combined with a computational model of AMPA receptor activation, provided results that were in agreement with the hypothesis that biphasic UBC EPSCs are due to prolonged entrapment of glutamate in the synaptic cleft. It is shown in **Chapter 2** that the timing of the slow EPSC in UBCs was variable and dependent on the frequency of presynaptic stimuli. This functionality could play a role in cerebellar timing of slow eye movements.

In **Chapter 3** a two-dimensional biophysical model is used to investigate spatial and temporal aspects of glutamate release and diffusion, and AMPA receptor activation. In order to simulate prolonged entrapment of glutamate it was necessary to considerably slow down glutamate diffusion. By distributing glutamate release sites and AMPA receptor models across the cleft area, it was possible to simulate AMPA receptor conductances that resembled UBC EPSCs.

Synaptic inputs interact with cell intrinsic excitability to produce spiking activity. **Chapter 4** presents an investigation of excitable mechanisms in UBCs, using various paradigms of direct somatic current injection. In response to depolarizing current steps, UBCs were able to generate strong bursts of action potentials from a hyperpolarized state. The dynamics of the slow excitable system underlying these bursts was investigated using a minimal theoretical model for excitable systems. In a depolarized suprathreshold state UBCs fired regular action potentials, and suprathreshold linearity and response gain were investigated using ramps, steps, and sinusoidal current injection protocols. UBC responses were found to be linear in a broad range of output firing rate frequencies, and exhibited flat response gain and phase for sinusoidal modulation frequencies ranging from 0.125-4 Hz. This frequency range covers the physiologically relevant frequency content of head and eye movement in VOR and OKR.

5.2 Discussion

5.2.1 Signal transmission by UBCs

Granule cells are the main elements of the cerebellar granular layer, and have been proposed to be specifically suited to the spatial integration of distinct synaptic inputs [15–17, 128]. In contrast, such integration does not seem to be a function of UBCs, given their dedicated connection to a single mossy fiber. UBCs appear a local network specialization for performing temporal rather than spatial integration. The giant contact area of the synapse does, however, allow for spatial interactions between individual release sites, as discussed in Chapter 3. Temporal integration in the UBC synapse occurs through an unusual mechanism of steady-state activation of receptors due to long-lasting glutamate entrapment [36, 37]. Steady-state activation of AMPARs results in delayed slow synaptic currents of fixed amplitude and variable timing (Chapter 2). The biophysical origin of the EPSC, and in general the physiological impact of the glomerular structure of the synapse, still hold many unanswered questions. For example, it is unclear exactly how glutamate entrapment for periods up to seconds is achieved, and how brush morphology and distributions of the various receptor channels influence transmission (Chapter 3).

Several other elements of slow integration are also present at the UBC synapse. NMDARs mediate a substantial part of the synaptic current in over half of the UBCs in young rats [36, 129]. Due to the different kinetics of NMDARs, steady-state activation does not generate a double-peaked EPSC, but instead results in a monotonic current tail with slow exponential decay. NMDARs might perform leaky integration in response to repetitive synaptic inputs, as they do in granule cells [34, 130]. Furthermore, UBCs express one or more types of metabotropic glutamate receptors which are present at the perisynaptic membrane surrounding the PSD and extrasynaptically at filopodia [32]. Although this has not yet explicitly been shown, they might affect transmission under conditions of high frequency presynaptic activity as in other cerebellar synapses [131, 132]. Activation of mGluRs might have a complicated effect on synaptic transmission, as mGluR1a activation has been shown to depolarize UBCs [34], while mGluR2 activation hyperpolarizes UBCs [33]. Indeed, slow inhibitory responses to mossy fiber stimulation have been observed [133], and it has been mentioned that they occur in mGluR2-expressing UBCs [38]. Mossy fiber activation alone could thus have bimodal effects in some UBCs, where ionotropic depolarization is followed by metabotropic hyperpolarization.

UBCs are a heterogeneous population, divided on the basis of expressing either mGlur1a or calretinin [29]. There is some indication that UBC genetic heterogeneity is correlated with the origin of different types of mossy fibers synapsing on UBCs [29]. It is unknown, however, whether the heterogeneity in UBC genetic make-up also has a correlate in elements of ionotropic transmission, for example through the relative expression and distribution of AMPAR and NMDAR channels. Although in this thesis no distinction was made between the two UBC subtypes, the slow biphasic EPSC as described in Chapter 2 could be expected to be a feature of both, as the entrapment of glutamate is likely due to the morphology of the synapse, and all UBCs share the giant dendritic brush as a common characteristic. Axons from Golgi cells also enter UBC glomeruli [64], and indeed Golgi cell activation induces IPSCs in UBCs, which are predominantly mediated by glycinergic receptors [39]. Furthermore, the synaptic balance between excitatory and inhibitory inputs appears tuned to specific UBC types, as the presence of a GABAergic component is strictly anticorrelated with expression of mGluR2 (but not mGluR1) [38]. Synaptic transmission in UBCs thus appears a strictly regulated mixture of tonic and phasic signals.

The physiological significance of synaptic mechanisms can only be truly appreciated in relation to the full set of cell intrinsic mechanisms that ultimately determine the output of the cell, that is the generation of action potentials. In UBCs synaptic inputs are coupled to several intrinsic systems. I_h can be active around the resting membrane potential in response to strong mossy fiber bundle activity, causing sustained depolarization [47]. From hyperpolarized membrane potentials, the low-threshold I_{CaT} can be activated to produce bursts of action potentials. In UBCs that are intrinsically active, I_{CaT}-mediated bursts might be activated following strong inhibitory input. In UBCs that are not intrinsically active, I_{CaT} might be activated following pauses in excitatory input. In both cases, it might regulate input-output gain during periods of continuous activity, as in other neurons [120].

5.2.2 UBCs and behavior

UBCs appear most prominently in cerebellum and cerebellum-like areas that are targeted by fibers originating from peripheral sensors specialized for detecting motion, gravity and sound in mammals, and electroreception in some fish. These brain regions perform the complex and interrelated processing involved in sound source localization and spatial orientation of the body [134]. Possibly, the presence of UBCs in such areas is an indication that these different computations share fundamental underlying principles, and slow or tonic signals from UBCs support those principles. Alternatively, UBCs could be uniquely involved with processing vestibular information, and their presence in sound-processing areas could be to support an efference copy of head movement and/or static tilt information. This issue could be resolved by determining the origins of fibers projecting to UBCs in these areas, which are still largely unknown [23].

The cerebellum ensures the smooth execution of movements, by tightly controlling the relative timing of motor commands to smoothly perform sequences of muscle contractions. Controlling muscles requires complex transformations from abstract neural commands in the brain to accurate movements in the real world. This is especially challenging because the spatial and temporal framework of movements changes continuously, and muscles themselves have nonlinear response properties and various time constants of activation and relaxation. In the control of eye movements, the cerebellum is widely believed to adaptively construct optimal neural commands [2, 69, 135] operating within a framework of topographically organized anatomical connections. The granular layer is the entry stage of the cerebellum, and is believed to perform a recoding and expansion of mossy fiber signals [15, 16]. Several hypotheses exist with respect to temporal processing in the granular layer, often involving phasic feedback inhibition from Golgi cells [135–137]. In order to deal with long time constants involved in the commands for eye muscles, the granule cell layer has been proposed to generate delayed representations of mossy fiber inputs [68, 69]. In view of the general diversity in UBC characteristics, it is possible that different UBC subtypes perform different functions in the cerebellar circuit. However, slow activation processes are a characteristic feature of the physiology of all UBCs, and some suggestions as to their potential roles and function have been for example 'feed-forward amplification' [36], 'integrators and/or temporal filters' [38], 'supporting oculomotor integration' [47].

The high tonic background activity of vestibular afferents and nuclei neurons has inspired linear systems-type analyses of neural activity in the VOR and OKR [97, 98, 101, 102]. Furthermore, adaptive filter models provide a robust framework for the functioning of cerebellar cortex in modulating the neural pathways subserving vestibular reflexes [135, 138]. Such models often introduce long granular layer delays as a top-down assumption. UBCs might provide delayed granular layer signaling through the slow synaptic processes described in Chapter 2, providing a flexible substrate for cerebellar adaptation in a range of temporal windows. Variable slow UBC excitation might allow Purkinje cells in the vestibulo-cerebellum to construct appropriate output signals by selecting subsets of parallel fibers through synaptic plasticity at parallel fiber to Purkinje cell synapses [139]. A computational model of cerebellar VOR adaptation based on this principle was used by the author of this thesis in a study aimed at elucidating the role of molecular layer interneurons (MLIs) in cerebellar function and learning ([140], not covered in this thesis). The excitatory parallel fiber pathway is complemented by an inhibitory pathway through MLIs, which provide feedforward inhibition to Purkinje cells [141], and have been shown able to shift the phase of floccular Purkinje cell simple spike responses by up to 180° in response to sinusoidal vestibular stimulation [142]. Sinusoidal stimulation is most often used both in experimental conditions as well as in computational models due to its analytical tractability [143]. In Wulff et al. a broad phase dispersion of parallel fiber signals was assumed to be generated in the granular layer and in part supported by MLIs, allowing Purkinje cells to appropriately adapt their output [140]. The model was based on vectorial summation of the polar coordinates of the sinusoidal modulation, and incorporated adaptation at the level of Purkinje cells as well as their target vestibular nucleus neurons. It provided an explanation for the diminished consolidation and depth of VOR phase adaptation in PC-$\Delta\gamma2$ mice, which lack forward inhibition through MLIs.

5.3 Future prospects

To fully understand UBC signal transmission, the synaptic and intrinsic elements need to be studied both in isolation, to determine their individual biophysical properties and the currents they generate, as well as in conjunction, to explore the full parameter space defined by their interactions and the resulting effect on the membrane potential. Achieving such understanding will likely require a combination of various experimental and computational approaches. The relative electrotonic compactness of UBCs might make them suited to dynamic current clamp studies, which could considerably alleviate the difficulties in assessing the effects of interacting excitatory and inhibitory synaptic inputs on the membrane potential [144].

A classical technique to assess the function of a neural circuit element is by lesioning the element, and investigating the effect on neural activity and animal behavior. In addition to mechanical or chemical lesioning, sophisticated genetic techniques can be used in certain cases to cell-specifically inactivate or otherwise affect a single neuronal type. Although such techniques are not yet available for UBCs, their development would create an attractive model for several reasons. First, UBCs are elements that are superimposed on the basic cerebellar circuitry, and disabling their functioning would not abrogate direct mossy fiber-granule cell transmission, allowing their specific contribution to signal processing to be examined. Second, the predominance of UBC expression in vestibular areas would naturally restrict a genetic lesion to the (para-)flocculus and medial vermis, without much affecting the rest of the cerebellum. The VOR-OKR behavioral system, arguably the most widely studied form of cerebellum-controlled behavior, is in this case a natural choice for assessing a behavioral phenotype. Third, the specific specialization of UBC transmission could allow for generating specific predictions as to the effects on behavior, were they to be disabled. VOR and OKR have long been a popular target for computational models, which have often relied on the top-down implementation of slow signals or delays in the granular layer. If UBCs are indeed uniquely responsible for generating such signaling, a combination of computational and behavioral experiments might uncover their physiological roles. On the other hand, a practical difficulty to any genetic lesioning study is the flexible ability of the brain to compensate for partial loss of function. The severity of the effect on behavior of a loss of UBC function, as well as the ability of the brain to compensate for the highly specialized UBC physiology, are thus uncertain. In this respect it is noticable that a recent report showed that ablation of Cr^+ UBCs was correlated with the onset of ataxia in moonwalker (mwk) mice [145].

Bibliography

[1] E. R. Kandel, J. H. Schwartz, and T. M. Jessell. *Principles of neural science.* McGraw-Hill, Health Professions Division, fourth edition, 2000.

[2] M. Ito. Cerebellar control of the vestibulo-ocular reflex–around the flocculus hypothesis. *Annu Rev Neurosci*, 5:275–296, 1982.

[3] S. du Lac and S. G. Lisberger. Cellular processing of temporal information in medial vestibular nucleus neurons. *J Neurosci*, 15:8000–8010, 1995.

[4] C. I. De Zeeuw, D. R. Wylie, J. S. Stahl, and J. I. Simpson. Phase relations of purkinje cells in the rabbit flocculus during compensatory eye movements. *J Neurophysiol*, 74, 1995.

[5] M. Ito, N. Nisimaru, and M. Yamamoto. Postsynaptic inhibition of oculomotor neurons involved in vestibulo-ocular reflexes arising from semicircular canals of rabbits. *Exp Brain Res*, 24:273–283, 1976.

[6] D. E. Angelaki and K. E. Cullen. Vestibular system: the many facets of a multimodal sense. *Annu Rev Neurosci*, 31:125–150, Jan 2008.

[7] Jan Voogd and Mitchell Glickstein. The anatomy of the cerebellum. *Trends Neurosci*, 21: 370–375, 1998.

[8] C. I. De Zeeuw, D. R. Wylie, P. L. Digiorgi, and J. I. Simpson. Projections of individual purkinje cells of identified zones in the flocculus to the vestibular and cerebellar nuclei in the rabbit. *J Comp Neurol*, 349:428–447, 1994.

[9] M. Schonewille, C. Luo, T. J. Ruigrok, J. Voogd, M. T. Schmolesky, M. Rutteman, F. E. Hoebeek, M. T. G. de Jeu, and C. I. De Zeeuw. Zonal organization of the mouse flocculus: physiology, input, and output. *J Comp Neurol*, 497:670–682, Aug 2006.

[10] N. H. Barmack, R. W. Baughman, P Errico, and H Shojaku. Vestibular primary afferent projection to the cerebellum of the rabbit. *J Comp Neurol*, 327:521–534, 1993.

[11] C. I. De Zeeuw, J. I. Simpson, C. C. Hoogenraad, N. Galjart, S. K. E. Koekkoek, and T. J. H. Ruigrok. Microcircuitry and function of the inferior olive. *Trends Neurosci*, 21: 391–400, 1998.

[12] J. C. Eccles. The cerebellum as a computer: patterns in space and time. *J Physiol*, 229: 1, 1973.

[13] J. C. Eccles, R. Llinas, and K. Sasaki. The mossy fibre-granule cell relay of the cerebellum and its inhibitory control by golgi cells. *Exp Brain Res*, 1:82, 1966.

[14] E. Galliano, P. Mazzarello, and E. d'Angelo. Discovery and rediscoveries of golgi cells. *J Physiol*, 588:3639–3655, Oct 2010.

[15] D. Marr. A theory of cerebellar cortex. *J Physiol*, 202:437–470, 1969.

[16] J. S. Albus. A theory of cerebellar function. *Math Biosci*, 10:25–61, 1971.

[17] C.-C. Huang, K. Sugino, Y. Shima, C. Guo, S. Bai, D. B. Mensh, S. B. Nelson, and A. W. Hantman. Convergence of pontine and proprioceptive streams onto multimodal cerebellar granule cells. *eLIFE*, 2:1, 2013.

[18] F. Bengtsson and H. Jorntell. Sensory transmission in cerebellar granule cells relies on similarly coded mossy fiber inputs. *Proc Natl Acad Sci U S A*, 106:2389–2394, 2009.

[19] S. G. Lisberger, A. Pavelko, H. M. Bronte-Stewart, and L. S. Stone. Neural basis for motor learning in the vestibuloocular reflex of primates. ii. changes in the responses of horizontal gaze velocity purkinje cel is in the cerebellar flocculus and ventral paraflocculus. *J Neurophysiol*, 72:954–973, 1994.

[20] A. Arenz, R. A. Silver, A. T. Schaefer, and T. W. Margrie. The contribution of single synapses to sensory representation in vivo. *Science*, 321:977–980, Aug 2008.

[21] T. J. Ruigrok, R. A. Hensbroek, and J. I. Simpson. Spontaneous activity signatures of morphologically identified interneurons in the vestibulocerebellum. *J Neurosci*, 31:712–724, Jan 2011.

[22] E. Mugnaini, A. Floris, and M. Wright-Goss. Extraordinary synapses of the unipolar brush cell- and electron microscopic study in the rat cerebellum. *Synapse*, 16:284–311, 1994.

[23] E. Mugnaini, G. Sekerkova, and M. Martina. The unipolar brush cell: a remarkable neuron finally receiving deserved attention. *Brain Res Rev*, 66:220–245, Jan 2011.

[24] O. P. Hamill, A. Marty, E. Neher, B. Sakmann, and F. J. Sigworth. Improved patch-clamp techniques for high-resolution current recording from cells and cell-free membrane patches. *Pflugers Arch*, 391:85, 1981.

[25] Multiclamp 700b, theory and operation, 2005.

[26] pclamp 9, user's guide, 2003.

[27] J. Altman and S. A. Bayer. Time of origin and distribution of a new cell type in the rat cerebellar cortex. *Exp Brain Res*, 29:265–274, 1997.

[28] Chris Englund, Tom Kowalczyk, Ray A. M. Daza, Avner Dagan, Charmaine Lau, Matthew F. Rose, and Robert F. Hevner. Unipolar brush cells of the cerebellum are produced in the rhombic lip and migrate through developing white matter. *J Neurosci*, 26:9184–9195, Sep 2006.

[29] G. Sekerkova, M. Watanabe, M. Martina, and E. Mugnaini. Differential distribution of phospholipase c beta isoforms and diaglycerol kinase-beta in rodents cerebella corroborates the division of unipolar brush cells into two major subtypes. *Brain Struct Funct*, Mar 2013.

[30] D. Jaarsma, M. R. Dino, C. Cozzari, and E. Mugnaini. Cerebellar choline acetyltransferase positive mossy fibres and their granule and unipolar brush cell targets: a model for central cholinergic nicotinic neurotransmission. *J Neurocytol*, 25:829–842, 1996.

[31] E. Mugnaini, M. R. Dino, and D. Jaarsma. The unipolar brush cells of the mammalian cerebellum and cochlear nucleus: cytology and microcircuitry. *Prog Brain Res*, 114:131–150, 1997.

[32] D. Jaarsma, M. R. Dino, H. Ohishi, R. Shigemoto, and E. Mugnaini. Metabotropic glutamate receptors are associated with non-synaptic appendages of unipolar brush cells in rat cerebellar cortex and cochlear nuclear complex. *J Neurocytol*, 27:303–327, 1998.

[33] M. J. Russo, H. J. Yau, M. G. Nunzi, E. Mugnaini, and M. Martina. Dynamic metabotropic control of intrinsic firing in cerebellar unipolar brush cells. *J Neurophysiol*, 100:3351–3360, Dec 2008.

[34] E. J. Schwartz, J. S. Rothman, G. P. Dugue, M. Diana, C. Rousseau, R. A. Silver, and S. Dieudonne. Nmda receptors with incomplete mg block enable low-frequency transmission through the cerebellar cortex. *J Neurosci*, 32:6878–6893, May 2012.

[35] J. C. Eccles and J. C. Jaeger. The relationship between the mode of operation and the dimensions of the junctional regions at synapses and motor end-organs. *Proc R Soc Lond B*, 148:38–56, 1958.

[36] D. J. Rossi, S. Alford, E. Mugnaini, and Slater N. Traverse. Properties of transmission at a giant glutamatergic synapse in cerebellum: The mossy fiber-unipolar brush cell synapse. *J Neurophysiol*, 74:24–42, 1995.

[37] G. A. Kinney, L. S. Overstreet, and N. T. Slater. Prolonged physiological entrapment of glutamate in the synaptic cleft of cerebellar unipolar brush cells. *J Neurophysiol*, 78: 1320–1333, 1997.

[38] C. V. Rousseau, G. P. Dugue, A. Dumoulin, E. Mugnaini, S. Dieudonne, and M. A. Diana. Mixed inhibitory synaptic balance correlates with glutamatergic synaptic phenotype in cerebellar unipolar brush cells. *J Neurosci*, 32:4632–4644, Mar 2012.

[39] G. P. Dugue, A. Dumoulin, A. Triller, and S. Dieudonne. Target-dependent use of co-released inhibitory transmitters at central synapses. *J Neurosci*, 25:6490–6498, Jul 2005.

[40] M. G. Nunzi and E. Mugnaini. Unipolar brush cell axons form a large system of intrinsic mossy fibers in the postnatal vestibulocerebellum. *J Comp Neurol*, 422:55–65, 2000.

[41] M. R. Dino, R. J. Schuerger, Y. B. Liu, N. T. Slater, and E. Mugnaini. Unipolar brush cell: a potential feedforward excitatory interneuron of the cerebellum. *Neuroscience*, 98: 625–636, 2000.

[42] Z. Gao, B. Todorov, C. F. Barrett, S. van Dorp, M. D. Ferrari, A. M. J. M. van den Maagdenberg, C. I. De Zeeuw, and F. E. Hoebeek. Cerebellar ataxia by enhanced cav2.1 currents is alleviated by ca2+-dependent k+-channel activators in cacna1as218l mutant mice. *J Neurosci*, 32:15533–15546, Jan 2012.

[43] J. I. Simpson, H. C. Hulscher, E. Sabel-Goedknegt, and T. J. H. Ruigrok. Between in and out: linking morphology and physiology of cerebellar cortical interneurons. *Prog Brain Res*, 148:329–340, 2005.

[44] N. H. Barmack and V. Yakhnitsa. Functions of interneurons in mouse cerebellum. *J Neurosci*, 28:1140–1152, Jan 2008.

[45] M. A. Diana, Y. Otsu, G. Maton, T. Collin, M. Chat, and S. Dieudonne. T-type and l-type ca2+ conductances define and encode the bimodal firing pattern of vestibulocerebellar unipolar brush cells. *J Neurosci*, 27:3823–3838, Apr 2007.

[46] M. J. Russo, E. Mugnaini, and M. Martina. Intrinsic properties and mechanisms of spontaneous firing in mouse cerebellar unipolar brush cells. *J Physiol*, 581:709–724, Jun 2007.

[47] F. Locatelli, L. Botta, F. Prestori, S. Masetto, and E. d'Angelo. Late-onset bursts evoked by mossy fiber bundle stimulation in unipolar brush cells: evidence for the involvement of h- and trp-currents. *J Physiol*, Dec 2012.

[48] J. A. Kim, G. Sekerkova, E. Mugnaini, and M. Martina. Electrophysiological, morphological, and topological properties of two histochemically distinct subpopulations of cerebellar unipolar brush cells. *Cerebellum*, Apr 2012.

[49] P. B. Sargent, C. Saviane, T. A. Nielsen, D. A. DiGregorio, and R. A. Silver. Rapid vesicular release, quantal variability, and spillover contribute to the precision and reliability of transmission at a glomerular synapse. *J Neurosci*, 25:8173–8187, Sep 2005.

[50] C. Saviane and R. A. Silver. Fast vesicle reloading and a large pool sustain high bandwidth transmission at a central synapse. *Nature*, 439:983–987, Feb 2006.

[51] E. A. Rancz, T. Ishikawa, I. Duguid, P. Chadderton, S. Mahon, and M. Hausser. High-fidelity transmission of sensory information by single cerebellar mossy fibre boutons. *Nature*, 450:1245–1248, Dec 2007.

[52] D. A. DiGregorio, J. S. Rothman, T. A. Nielsen, and R. A. Silver. Desensitization properties of ampa receptors at the cerebellar mossy fiber granule cell synapse. *J Neurosci*, 27: 8344–8357, Aug 2007.

[53] D. A. DiGregorio, Z. Nusser, and Silver R. Angus. Spillover of glutamate onto synaptic ampa receptors enhances fast transmission at a cerebellar synapse. *Neuron*, 35:521–533, Aug 2002.

[54] T. A. Nielsen, D. A. DiGregorio, and Silver R. Angus. Modulation of glutamate mobility reveals the mechanism underlying slow-rising ampar epscs and the diffusion coefficient in the synaptic cleft. *Neuron*, 42:757–771, 2004.

[55] L. O. Trussell and G. D. Fischbach. Glutamate receptor desensitization and its role in synaptic transmission. *Neuron*, 3:209–218, 1989.

[56] M. V. Jones and G. L. Westbrook. The impact of receptor desensitization on fast synaptic transmission. *Trends Neurosci*, 19:96, 1996.

[57] R. S. Zucker and W. G. Regehr. Short-term synaptic plasticity. *Annu Rev Physiol*, 64: 355–405, Jan 2002.

[58] L. O. Trussell, S. Zhang, and I. M. Raman. Desensitization of ampa receptors upon multiquantal neurotransmitter release. *Neuron*, 10:1185–1196, 1993.

[59] I. M. Raman and L. O. Trussell. The mechanism of alpha-amino-3-hydroxy-5-methyl-4-isoxazolepropionate receptor desensitization after removal of glutamate. *Biophys J*, 68: 137–146, 1995.

[60] T. S. Otis, Y.-C. Wu, and L. O. Trussell. Delayed clearance of transmitter and the role of glutamate transporters at synapses with multiple release sites. *J Neurosci*, 16:1634–1644, 1996.

[61] M. Hausser and B. A. Clark. Tonic synaptic inhibition modulates neuronal output pattern and spatiotemporal synaptic integration. *Neuron*, 19:665–678, 1997.

[62] T. Otis, S. Zhang, and L. O. Trussell. Direct measurement of ampa receptor desensitization induced by glutamatergic synaptic transmission. *J Neurosci*, 16:7496–7504, 1996.

[63] M. A. Xu-Friedman and W. G. Regehr. Ultrastructural contributions to desensitization at cerebellar mossy fiber to granule cell synapses. *J Neurosci*, 23:2182–2192, 2003.

[64] E. Mugnaini and A. Floris. The unipolar brush cell: A neglected neuron of the mammalian cerebellar cortex. *J Comp Neurol*, 339:174–180, 1994.

[65] E. d'Angelo, S. K. Koekkoek, P. Lombardo, S. Solinas, E. Ros, J. Garrido, M. Schonewille, and C. I. De Zeeuw. Timing in the cerebellum: oscillations and resonance in the granular layer. *Neuroscience*, 162:805–815, Sep 2009.

[66] C. I. De Zeeuw and C. H. Yeo. Time and tide in cerebellar memory formation. *Curr Opin Neurobiol*, 15:667–674, Dec 2005.

[67] D. B. Arnold and D. A. Robinson. The oculomotor integrator: testing of a neural network model. *Exp Brain Res*, 113:57–74, 1997.

[68] J. L. Raymond and S. G. Lisberger. Neural learning rules for the vestibulo-ocular reflex. *J Neurosci*, 18:9112–9129, 1998.

[69] P. Dean, J. Porrill, and J. V. Stone. Decorrelation control by the cerebellum achieves oculomotor plant compensation in simulated vestibulo-ocular reflex. *Proc Biol Sci*, 269: 1895–1904, Sep 2002.

[70] B. E. Kalmbach, H. Voicu, T. Ohyama, and M. D. Mauk. A subtraction mechanism of temporal coding in cerebellar cortex. *J Neurosci*, 31:2025–2034, Feb 2011.

[71] J. F. Medina, M. R. Carey, and S. G. Lisberger. The representation of time for motor learning. *Neuron*, 45:157–167, Jan 2005.

[72] M. L. Hines and N. T. Carnevale. The neuron simulation environment. *Neural Comput*, 9, 1997.

[73] M. L. Hines, A. P. Davison, and E. Muller. Neuron and python. *Front Neuroinform*, 3:1, Jan 2009.

[74] Python programming language. `http://www.python.org`, 7 2013.

[75] T. M. Bartol, B. R. Land, E. E. Salpeter, and M. M. Salpeter. Monte carlo simulation of miniature endplate current generation in the vertebrate neuromuscular junction. *Biophys J*, 59:1290–1307, 1991.

[76] P. J. Kruk, H. Korn, and D. S. Faber. The effects of geometrical parameters on synaptic transmission: A monte carlo simulation study. *Biophys J*, 73:2874–2890, 1997.

[77] K. M. Franks, T. M. Bartol, and T. J. Sejnowski. A monte carlo model reveals independent signaling at central glutamatergic synapses. *Biophys J*, 83:2333–2348, 2002.

[78] A. Destexhe, Z. F. Mainen, and T. J. Sejnowski. Kinetic models of synaptic transmission. *Meth Neuronal Mod*, page 1, 1998.

[79] A. Peters and S. L. Palay. The morphology of synapses. *J Neurocytol*, 25:687–700, 1996.

[80] J. Kleinle, K. Vogt, H.-R. Luscher, L. Muller, W. Senn, K. Wyler, and J. Streit. Transmitter concentration profiles in the synaptic cleft: an analytical model of release and diffusion. *Biophys J*, 71:2413–2426, 1996.

[81] W. R. Holmes. Modeling the effect of glutamate diffusion and uptake on nmda and non-nmda receptor saturation. *Biophys J*, 69:1734–1747, 1995.

[82] L. G. Longsworth. Diffusion measurements, at 25 degrees, of aqueous solutions of amino acids, peptides and sugars. *JACS*, 75:5705–5709, 1953.

[83] C. Nicholson and J. M. Phillips. Ion diffusion modified by tortuosity and volume fraction in the extracellular microenvironment of the rat cerebellum. *J Physiol*, 321:225–257, 1981.

[84] M. Hausser and A. Roth. Dendritic and somatic glutamate receptor channels in rat cerebellar purkinje cells. *J Physiol*, 501:77–95, 1997.

[85] L. S. Overstreet, G. A. Kinney, Y.-B. Liu, D. Billups, and Slater N. Traverse. Glutamate transporters contribute to the time course of synaptic transmission in cerebellar granule cells. *J Neurosci*, 19:9663–9673, 1999.

[86] Karim Le Meur, Micaela Galante, Maria Cecilia Angulo, and Etienne Audinat. Tonic activation of nmda receptors by ambient glutamate of non-synaptic origin in the rat hippocampus. *J Physiol*, 580:373–383, Apr 2007.

[87] J. G. Borst. The low synaptic release probability in vivo. *Trends Neurosci*, 33:259–266, Jun 2010.

[88] Fipy: A finite volume pde solver using python. `http://www.ctcms.nist.gov/fipy/`, 10 2013.

[89] Nelson P. C. *Biological Physics: Energy, Information, Life*. W. H. Freeman and Company, 2003.

[90] Sweers G. *Complexe functies, gewone en partiele differentiaalvergelijkingen*. VSSD, 1998.

[91] P. Dayan and L. F. Abbott. *Theoretical neuroscience: computational and mathematical modeling of neural systems*. The MIT Press, 2001.

[92] J. M. Goldberg and C. Fernandez. Physiology of peripheral neurons innervating semicircular canals of the squirrel monkey. i. resting discharge and response to constant angular accelerations. *J Neurophysiol*, pages 635–660, 1971.

[93] J. M. Goldberg and C. Fernandez. Vestibular mechanisms. *Annu Rev Neurosci*, pages 129–162, 1975.

[94] S. G. Sadeghi, M. J. Chacron, M. C. Taylor, and K. E. Cullen. Neural variability, detection thresholds, and information transmission in the vestibular system. *J Neurosci*, 27:771–781, Jan 2007.

[95] C. D. Aizenman and D. J. Linden. Regulation of the rebound depolarization and spontaneous firing patterns of deep nuclear neurons in slices of rat cerebellum. *J Neurophysiol*, 82:1697–1709, 1999.

[96] K. E. Kolkman, L. E. McElvain, and S. du Lac. Diverse precerebellar neurons share similar intrinsic excitability. *J Neurosci*, 31:16665–16674, Nov 2011.

[97] A. A. Skavenski and D. A. Robinson. Role of abducens neurons in vestibuloocular reflex. *J Neurophysiol*, 1973.

[98] J. S. Stahl and J. I. Simpson. Dynamics of rabbit vestibular nucleus neurons and the influence of the flocculus. *J Neurophysiol*, 73:1396–1413, 1995.

[99] S. du Lac, J. L. Raymond, T. J. Sejnowski, and S. G. Lisberger. Learning and memory in the vestibulo-ocular reflex. *Annu Rev Neurosci*, 18:409–441, 1995.

[100] M. W. Bagnall, L. E. McElvain, M. Faulstich, and S. du Lac. Frequency-independent synaptic transmission supports a linear vestibular behavior. *Neuron*, 60:343–352, Oct 2008.

[101] C. Fernandez and J. M. Goldberg. Physiology of peripheral neurons innervating semicircular canals of the squirrel monkey. ii. response to sinusoidal stimulation and dynamics of peripheral vestibular system. *J Neurophysiol*, pages 661–675, 1971.

[102] J. S. Stahl and J. I. Simpson. Dynamics of abducens nucleus neurons in the awake rabbit. *J Neurophysiol*, 73:1383–1395, 1995.

[103] C. I. De Zeeuw, F. E. Hoebeek, L. W. Bosman, M. Schonewille, L. Witter, and S. K. Koekkoek. Spatiotemporal firing patterns in the cerebellum. *Nat Rev Neurosci*, 12:327–344, Jun 2011.

[104] E. d'Angelo, G. de Filippi, P. Rossi, and V. Taglietti. Ionic mechanism of electroresponsiveness in cerebellar granule cells implicates the action of a persistent sodium current. *J Neurophysiol*, 80:493–503, 1998.

[105] L. Forti, E. Cesana, J. Mapelli, and E. d'Angelo. Ionic mechanisms of autorhythmic firing in rat cerebellar golgi cells. *J Physiol*, 574:711–729, Aug 2006.

[106] R. LLinas and M. Sugimori. Electrophysiological properties of in vitro purkinje cell dendrites in mammalian cerebellar slices. *J Physiol*, 305:197–213, 1980.

[107] R. Llinas, W. Precht, and M. Clarke. Cerebellar purkinje cell responses to physiological stimulation of the vestibular system in the frog. *Exp Brain Res*, 13:408–431, 1971.

[108] W. Precht, J. I. Simpson, and R. Llinas. Responses of purkinje cells in rabbit nodulus and uvula to natural vestibular and visual stimuli. *Pflugers Arch*, 367:1–6, 1976.

[109] F. E. Hoebeek, L. Witter, T. J. Ruigrok, and C. I. De Zeeuw. Differential olivo-cerebellar cortical control of rebound activity in the cerebellar nuclei. *Proc Natl Acad Sci U S A*, 107:8410–8415, May 2010.

[110] A. L. Person and I. M. Raman. Purkinje neuron synchrony elicits time-locked spiking in the cerebellar nuclei. *Nature*, Dec 2011.

[111] V. Steuber, N. W. Schultheiss, R. A. Silver, E. de Schutter, and D. Jaeger. Determinants of synaptic integration and heterogeneity in rebound firing explored with data-driven models of deep cerebellar nucleus cells. *J Comput Neurosci*, 30:633–658, Jun 2011.

[112] C. Sekirnjak and S. du Lac. Intrinsic firing dynamics of vestibular nucleus neurons. *J Neurosci*, 22:2083–2095, 2002.

[113] R. R. Llinas. The intrinsic electrophysiological properties of mammalian neurons: Insights into central nervous system function. *Science*, 242:1654–1664, 1988.

[114] Izhikevich E. M. *Dynamical systems in neuroscience*. The MIT Press, 2007.

[115] J. Rinzel and B. Ermentrout. Analysis of neural excitability and oscillations. *Methods in neuronal modeling*, pages 251–291, 1998.

[116] R. Fitzhugh. Impulses and physiological states in theoretical models of nerve membrane. *Biophys J*, 1:445–466, 1961.

[117] S. H. Strogatz. *Nonlinear dynamics and chaos*. Perseus Books Publishing, LLC, 2000.

[118] E. M. Izhikevich. Simple model of spiking neurons. *IEEE Trans Neural Netw*, 14:1569–1572, Jan 2003.

[119] M. R. Dino, A. A. Perachio, and E. Mugnaini. Cerebellar unipolar brush cells are targets of primary vestibular afferents: an experimental study in the gerbil. *Exp Brain Res*, 140: 162–170, 2001.

[120] M. R. Smith, A. B. Nelson, and S. du Lac. Regulation of firing response gain by calcium-dependent mechanisms in vestibular nucleus neurons. *J Neurophysiol*, 87:2031–2042, Apr 2002.

[121] N. T. Slater, D. J. Rossi, and G. A. Kinney. Physiology of transmission at a giant glutamatergic synapse in cerebellum. *Prog Brain Res*, 114:151–163, 1997.

[122] S. G. Lisberger and A. F. Fuchs. Role of primate flocculus during rapid behavioral modification of vestibuloocular reflex. i. purkinje cell activity during visually guided horizontal smooth-pursuit eye movements and passive head rotation. *J Neurophysiol*, 41:733–763, 1978.

[123] Y. Zhang, A. M. Partsalis, and S. M. Highstein. Properties of superior vestibular nucleus neurons projecting to the cerebellar flocculus in the squirrel monkey. *J Neurophysiol*, 69: 642–645, 1993.

[124] G. Cheron, M. Escudero, and E. Godaux. Discharge properties of brain stem neurons projecting to the flocculus in the alert cat. i. medial vestibular nucleus. *J Neurophysiol*, 76:1759–1774, Sep 1996.

[125] M. Escudero, G. Cheron, and E. Godaux. Discharge properties of brain stem neurons projecting to the flocculus in the alert cat. ii. prepositus hypoglossal nucleus. *J Neurophysiol*, 76:1775–1785, 1996.

[126] E. A. Baarsma and H. Collewijn. Vestibulo-ocular and optokinetic reactions to rotation and their interaction in the rabbit. *J Physiol*, 238:603–625, 1974.

[127] D. A. Robinson. Integrating with neurons. *Annu Rev Neurosci*, 12:33–45, 1989.

[128] F. Gabbiani, J. Midtgaard, and T. Knopfel. Synaptic integration in a model of cerebellar granule cells. *J Neurophysiol*, 72:999, 1994.

[129] D. Billups, Y. B. Liu, S. Birnstiel, and N. T. Slater. Nmda receptor-mediated currents in rat cerebellar granule and unipolar brush cells. *J Neurophysiol*, 87:1948–1959, Apr 2002.

[130] E. d'Angelo, G. de Filippi, P. Rossi, and V. Taglietti. Synaptic excitation of individual rat cerebellar granule cells in situ: evidence for the role of nmda receptors. *J Physiol*, 484: 397–413, 1995.

[131] F. Tempia, M. C. Miniaci, D. Anchisi, and P. Strata. Postsynaptic current mediated by metabotropic glutamate receptors in cerebellar purkinje cells. *J Neurophysiol*, 80:520–528, 1998.

[132] D. Watanabe and S. Nakanishi. mglur2 postsynaptically senses granule cell inputs at golgi cell synapses. *Neuron*, 39:821–829, 2003.

[133] S van Dorp, F. E. Hoebeek, T. M. Hoogland, E. d'Angelo, and C. I. De Zeeuw. Integration of mossy fiber signals at the mossy fiber to unipolar brush cell synapse. *SfN Abstr.*, 580.06/NN12, 2012.

[134] Donata Oertel and Eric D. Young. What's a cerebellar circuit doing in the auditory system? *Trends Neurosci*, 27:104–110, Feb 2004.

[135] M. Fujita. Adaptive filter model of the cerebellum. *Biol Cybern*, 45:195–206, 1982.

[136] R. Maex and E. de Schutter. Synchronization of golgi and granule cell firing in a detailed network model of the cerebellar granule cell layer. *J Neurophysiol*, 80:2521–2537, 1998.

[137] S. Solinas, T. Nieus, and E. d'Angelo. A realistic large-scale model of the cerebellum granular layer predicts circuit spatio-temporal filtering properties. *Front Cell Neurosci*, 4: 12, Jan 2010.

[138] P. Dean, J. Porrill, C. F. Ekerot, and H. Jorntell. The cerebellar microcircuit as an adaptive filter: experimental and computational evidence. *Nat Rev Neurosci*, 11:30–43, Jan 2010.

[139] Z. Gao, B. J. van Beugen, and C. I. De Zeeuw. Distributed synergistic plasticity and cerebellar learning. *Nat Rev Neurosci*, 13:619–635, Sep 2012.

[140] P. Wulff, M. Schonewille, M. Renzi, L. Viltono, M. Sassoe-Pognetto, A. Badura, Z. Gao, F. E. Hoebeek, S. van Dorp, W. Wisden, M. Farrant, and C. I. De Zeeuw. Synaptic inhibition of purkinje cells mediates consolidation of vestibulo-cerebellar motor learning. *Nat Neurosci*, 12:1042–1049, Aug 2009.

[141] J. C. Eccles, R. Llinas, and K. Sasaki. The inhibitory interneurones within the cerebellar cortex. *Exp Brain Res*, 1:1, 1966.

[142] Y. Miyashita and S. Nagao. Contribution of cerebellar intracortical inhibition to purkinje cell responses during vestibulo-ocular reflex of alert rabbits. *J Physiol*, 351:251–262, 1984.

[143] N. Masuda and S. Amari. A computational study of synaptic mechanisms of partial memory transfer in cerebellar vestibulo-ocular-reflex learning. *J Comput Neurosci*, 24: 137–156, Apr 2008.

[144] A. A. Prinz, L. F. Abbott, and E. Marder. The dynamic clamp comes of age. *Trends Neurosci*, 27:218–224, Apr 2004.

[145] J.-A. Kim, G. Sekerkova, E. B. E. Becker, J. Hartmann, L. Birnbaumer, E. Mugnaini, and M. Martina. The trpc3 moonwalker gain-of function mutation is accompanied by selective and complete ablation of type ii unipolar brush cells. *SfN abstract*, 561.23/BBB26, 2013.

Samenvatting

Het vestibulo-cerebellum is een gedeelte van het cerebellum dat betrokken is bij het reguleren van reflexmatige oogbewegingen. Een voorbeeld van zo'n reflexmatige oogbeweging is de vestibulo-oculaire reflex (VOR), die tot doel heeft om beelden op de retina te stabiliseren door de ogen te bewegen in een richting tegengesteld aan die van het hoofd. De VOR wordt geactiveerd door het vestibulaire orgaan (het evenwichtsorgaan), dat rotatie en verplaatsing van het hoofd registreert. In het vestibulo-cerebellum bevindt zich een relatief onbekend type hersencel dat unipolar brush cel (enkelpolige borstel cel; UBC) wordt genoemd. Dit proefschrift behandelt experimenteel en theoretisch onderzoek naar synaptische prikkeling en intrinsieke prikkelbaarheid van UBCs. **Hoofdstuk 1** beschrijft een aantal kenmerkende eigenschappen van synaptische signaaloverdracht, intrinsieke prikkelbaarheid en verbinding met andere cellen in het cerebellaire netwerk. UBCs geven signalen door aan cerebellaire korrelcellen en in sommige gevallen aan andere UBCs. De functionaliteit van deze neurale verbindingen werd aangetoond in **Hoofdstuk 1** door presynaptische mosvezels elektrisch te stimuleren in dunne plakjes cerebellair weefsel, terwijl synaptische activiteit werd gemeten in korrelcellen of UBCs. In sommige gevallen arriveerde de synaptische activiteit met een vertraging van tientallen milliseconden, terwijl synaptische overdracht tussen twee cellen normaal gesproken slechts 1 a 2 milliseconden in beslag neemt. Deze observatie kan worden verklaard door aan te nemen dat er zich een UBC bevond tussen de gestimuleerde mosvezel en de cel waarin activiteit werd gemeten. Daar komt bij dat de gemeten synaptische activiteit bestond uit series van meerdere impulsen, die overeenkwamen met typische responsen van UBCs wanneer deze kort elektrisch worden gestimuleerd. Verder bewijs dat UBCs signalen doorgeven werd geleverd door gebruik te maken van het feit dat sommige UBCs ook spontaan actief zijn. In sommige gevallen werd spontane synaptische activiteit gemeten in korrelcellen en UBCs, die kenmerken vertoonde overeenkomstig met spontane activiteit van UBCs.

Het meest onderscheidende kenmerk van UBCs is de enkele dendriet, die eruit ziet als een kwast met vele kleine uitsteeksels aan de uiteinden (vandaar de benaming 'unipolar brush'). De dendriet maakt een uitgebreid synaptisch contact met een enkele mosvezel, die informatie over hoofd- en oogbewegingen van buiten het cerebellum aanvoert. In **Hoofdstuk 2** wordt de invloed van deze speciale synaptische verbinding op signaaloverdracht onderzocht, door het opwekken en meten van *excitatory postsynaptic currents* (EPSCs) in UBCs. EPSCs zijn prikkelende synaptische stroompjes die binnenkomen via de dendriet en die de activiteit van een neuron verhogen. EPSCs in UBCs bestonden uit twee fases, een initiële snelle piek zoals die ook in andere neuronen voorkomt (bijvoorbeeld in korrelcellen), gevolgd door een tweede lagere en veel tragere piek die honderden milliseconden tot seconden lang kon duren. De gangbare hypothese met betrekking tot deze trage synaptische stroompjes stelt dat deze veroorzaakt worden door het langdurig vasthouden van neurale signaalstoffen in de synaps. Door langdurige reeksen van presynaptische stimulatie te gebruiken en de resultaten te combineren met een computermodel kon ondersteuning voor deze hypothese worden geleverd in **Hoofdstuk 2**. Tevens werd aangetoond dat het tijdstip van de piek van de trage EPSC variabel was en werd bepaald door de sterkte van de presynaptische stimulatie. Deze functionaliteit zou een belangrijke rol kunnen spelen in de coördinatie van bijvoorbeeld oogbewegingen door het cerebellum.

Computermodellen worden vaak gebruikt om te assisteren bij het interpreteren van experimentele resultaten, door waarnemingen te verklaren met behulp van simulaties. In **Hoofdstuk 3** werd een computermodel gebruikt om het tijdsverloop van de concentratie neurale signaalstoffen in de synaps te onderzoeken, alsmede de activatie van signaalreceptoren door deze signaalstoffen. Om het langdurig vasthouden van signaalstoffen in de synaps te simuleren, bleek het nodig om de bewegingssnelheid van deze stoffen drastisch te verlagen. EPSCs zoals die eerder werden beschreven konden worden nagebootst door op verscheidene plaatsen in het model bronnen van signaalstoffen en ook signaalreceptoren te simuleren.

De prikkelbaarheid van neuronen wordt bepaald door het vermogen om actiepotentialen te genereren, ofwel 'actief' te worden, als ze elektrisch worden gestimuleerd. Synaptische signalen bepalen samen met de intrinsieke prikkelbaarheid de signalen die neuronen doorsturen naar andere neuronen. **Hoofdstuk 4** behandelt onderzoek naar de prikkelbaarheid van UBCs, door verscheidene patronen van stroompjes direct in de cellen te injecteren. Vanuit een niet-actieve toestand reageerden UBCs op stroomstapjes door met hoge frequentie een aantal actiepotentialen te genereren. Dit werd veroorzaakt door de activering van een onderliggende trage actiepotentiaal, die vervolgens een aantal snelle actiepotentialen activeerde. In een toestand van hoge activiteit kwamen deze trage actiepotentialen niet voor, maar genereerden UBCs enkel snelle actiepotentialen in een gelijkmatig tempo. De frequentie van deze actiepotentialen werd onderzocht terwijl verscheidene patronen van stroompjes werden geïnjecteerd. De signaaloverdracht bleek uiterst lineair, en UBCs volgden de patronen nauwkeurig door de frequentie van actiepotentialen gelijkmatig te verhogen of verlagen. De gebruikte patronen vertoonden overeenkomsten met de patronen die voorkomen in hoofd- en oogbewegingen.

Curriculum vitae

Stijn van Dorp was born in Oosterhout, the Netherlands, in 1981. He studied applied physics at Delft University of Technology from 1999, and graduated *cum laude* in 2006. His thesis concerned the experimental determination of ionic currents and forces on DNA molecules in synthetic nanoscale pores. He subsequently pursued his interest in neuroscience through research projects at the Netherlands Institute for Neuroscience (NIN) and at New York University Medical Center, analyzing electrophysiological and behavioral data from anesthetized and awake animals. For his doctoral studies he focused on electrophysiology in cerebellar slices, investigating synaptic transmission and membrane excitability of unipolar brush cells in the Cerebellar Coordination & Cognition group at the NIN. Since October 2013 he is a research scholar in the department of Molecular and Cellular Physiology at Stanford University, developing *in vitro* model systems for a calcium signaling pathway.

Education

Netherlands Institute for Neuroscience	**Amsterdam**
Ph.D. candidate, with dr. C.I. de Zeeuw	2009–2013
New York University Medical Center	**New York**
Pre-doctoral fellow, with dr. J.I. Simpson	2008–2009
Netherlands Institute for Neuroscience	**Amsterdam**
Research assistant, with dr. C.I. de Zeeuw	2007–2008
Kavli Institute of Nanoscience	**Delft**
Research assistant, with dr. U.F. Keyser and dr. S.G. Lemay	2005–2007
Delft University of Technology	**Delft**
Student, Applied Physics	2003–2006
Study Association for Applied Physics (VvTP)	**Delft**
Fulltime member of the board	2002–2003
Delft University of Technology	**Delft**
Student, Applied Physics	1999–2002

Publications

Integration of mossy fiber signals at the mossy fiber to unipolar brush cell synapse S. van Dorp, F.E. Hoebeek, T.M. Hoogland, E. D'Angelo and C.I. De Zeeuw *SfN Abstr.* 580.06/NN12 (2012)

Cerebellar ataxia by enhanced Ca_V2.1-currents is alleviated by Ca^{2+}-dependent K^+-channel activators in *Cacna1a*^{S218L} mutant mice Z. Gao, B. Todorov, C.F. Barrett, S. van Dorp, M.D. Ferrari, A.M.J.M. van den Maagdenberg, C.I. De Zeeuw and F.E. Hoebeek *J. Neurosci.* 32, 15533-15546 (2012)

Comparing floccular granule cell activity in anesthetized and awake rabbits S. van Dorp, R.A. Hensbroek, B.J. van Beugen, J. Maruta, T.J.H. Ruigrok and J.I. Simpson *FENS Abstr.* 5, 141.16 (2010)

Tether forces in DNA electrophoresis U.F. Keyser, S. van Dorp and S.G. Lemay *Chem. Soc. Rev.* 39, 939-947 (2010)

Signal processing by cerebellar granule cells S. van Dorp, R.A. Hensbroek, B.J. van Beugen, J. Maruta, T.J.H. Ruigrok and J.I. Simpson *SfN Abstr.* 367.9/DD31 (2009)

Electrophoretic force on a protein-coated DNA molecule in a solid-state nanopore A.R. Hall, S. van Dorp, S.G. Lemay and C. Dekker *Nano Lett.* 9, 4441-4445 (2009)

Synaptic inhibition of Purkinje cells mediates consolidation of vestibulo-cerebellar motor learning P. Wulff*, M. Schonewille*, M. Renzi, L. Viltono, M. Sassoè-Pognetto, A. Badura, Z. Gao, F.E. Hoebeek, S. van Dorp, W. Wisden, M. Farrant and C.I. De Zeeuw *Nat. Neurosci.* 12, 1042-1049 (2009)

Origin of the electrophoretic force on DNA in solid-state nanopores S. van Dorp, U.F. Keyser, N.H. Dekker, C. Dekker and S.G. Lemay *Nat. Phys.* 5, 347-351 (2009)

Role of olivary electrical coupling in cerebellar motor learning R.S. van der Giessen*, S.K. Koekkoek*, S. van Dorp*, J.R. De Gruijl*, A. Cupido*, S. Khosrovani*, B. Dortland, K. Wellershaus, J. Degen, J. Deuchars, E.C. Fuchs, H. Monyer, K. Willecke, M.T.G. De Jeu and C.I. De Zeeuw *Neuron* 58, 599-612 (2008)

Direct force measurements on DNA in a solid-state nanopore U.F. Keyser, B.N. Koeleman, S. van Dorp, D. Krapf, R.M.M. Smeets, S.G. Lemay, N.H. Dekker and C. Dekker *Nat. Phys.* 2, 473-477 (2006)

* Equal contributions

Acknowledgements

First of all I would like to thank Chris De Zeeuw for allowing me to pursue my ideas and make this thesis possible. While under Chris' wing I worked on several different projects, and I would like to thank all the people I met and worked with during that time, both at the Erasmus Neuroscience department and at the Netherlands Institute for Neursocience. Jerry Simpson, NYC is burned into my brain, thank you for an unforgettable year. Thanks to Jun Maruta. Thanks to Robert Thorne for coffee, beers and unlimited enthusiasm.

Many thanks to the members of the Hoebeek lab. In particular I would like to thank Boeke van Beugen, Elisa Galliano, Freek Hoebeek and Zhenyu Gao for all the help and discussions. I would like to thank my friends and colleagues from the NIN: Aleksandra Smilgin, Beerend Winkelman, Cathrin Canto, Danny Riemens, Guilherme Testa-Silva, Janne Plugge, Jochen Spanke, Jornt de Gruijl, Laurens Witter, Leonardo Tolosa Rodríguez, Nicolas Gutierrez-Castellanos, Özgecan Özyildirim, Piotr Sokol, Samuel Picard, Saša Peter, Serhat Alkema and Tycho Hoogland, for many work- and non-work-related discussions, beers at the windmill and Sinterklaas dinners.

To my friends I am grateful for many things. Thank you for laughs and discussions over dinners and beers, hikes, squash and cycling. I particularly thank Freek Kelkensberg and Beerend Winkelman for accompanying me as my paranimfs. Finally, I thank my family for their unconditional help and support, and I especially thank Sascha for being the best partner and friend I could wish for; you are the one I need above all.